HELSINKI UNIVERSITY OF TECHNOLOGY
Department of Electrical and Communications Engineering
Electronic Circuit Design Laboratory

MONOLITHIC ACTIVE RESONATOR FILTERS FOR HIGH FREQUENCIES

Risto Kaunisto

November 2000

Dissertation for the degree of Doctor of Science in Technology to be presented with due permission of the Department of Electrical and Communications Engineering for public examination and debate in Auditorium S4 at Helsinki University of Technology (Espoo, Finland) on the 17th of November, 2000, at 12 o'clock noon.

ISBN 951-22-5194-9
ISSN 1455-8440

ABSTRACT

This doctoral thesis deals with monolithic active resonators and their use in high-frequency filters. The emphasis has been put on noise and distortion properties of active resonators, as these are crucial in potential applications. Two active resonator types are considered: passive LC resonators with active negative resistance compensation, and gyrator-based active inductor resonators.

An introduction to the theory of passive resonators is given, and the basic quality factor and noise characteristics are discussed in detail. Filter structures based on parallel resonators are studied and techniques for frequency tuning briefly introduced.

Based on a three-port equivalent, different negative resistor structures suitable for integration are categorized, and their fundamental small-signal and tuning properties derived. The noise properties of the topologies are analyzed and compared. The Volterra-series method is applied in the distortion estimations for each negative resistor type. Practical examples of integrated negative resistor are given with realistic measured data.

High-Q active inductors based on integrated high-frequency gyrators are analyzed using the total loop phase shift as an essential parameter. Theoretical limitations of high-frequency performance and tuning are found. Noise and distortion properties are assessed in the same manner as with negative resistors to give grounds for direct comparisons. Practical issues of monolithic active inductor resonators are tackled and realized topologies with measured results are presented.

Active resonator filters employing either of the resonator types are discussed. Their noise and distortion performance derived from the respective resonator results is calculated. Automated tuning techniques are briefly discussed. Exemplary designs are presented with measured data. The two realized active resonator filters with negative resistance resonators operate in the 3 – 4 GHz region with 1.1% and 12% relative bandwidths, 400-MHz tuning ranges, and 19-dB and 11-dB noise figures respectively. The DC power consumption is a low 15 mW per resonator. The active inductor filter has a center frequency of 2.4 GHz with almost 1-GHz tuning range. The noise figure is a high 30 dB as estimated by the theory.

System considerations show that active filters cannot directly replace passive filters in traditional radio architectures due to their relatively poor performance, but as a new potential application, an LO signal generation system for direct-conversion transmitters with a monolithic band-pass filter is presented. Both GaAs and Si-BiCMOS realizations show the feasibility of the concept. With the comparable quality factors of 415 and 300 and approximately the same –1-dB output compression points of –20 dBm, the BiCMOS topology consumes only a fraction of DC power but still gives more than 80 dBc mirror rejection thanks to its dual-mixer topology.

Keywords: analog integrated circuits, active resonators, negative resistors, active inductors, monolithic radio-frequency filters

PREFACE

I communed with mine own heart, saying, Lo, I am come to great estate, and have gotten more wisdom than all they that have been before me in Jerusalem: yea, my heart had great experience of wisdom and knowledge. And I gave my heart to know wisdom, and to know madness and folly: I perceived that this also is vexation of spirit. For in much wisdom is much grief: and he that increaseth knowledge increaseth sorrow.

Ecclesiastes 1:16 – 1:18

This doctoral thesis is a result of research work at the Electronic Circuit Design Laboratory, Institute of Radio Communications (IRC), in 1995 – 2000. The research has been part of the Academy of Finland's projects 'New Radio Systems and Their RF Technology' (SARF) 1995 – 1996, and 'Integrated Circuit Solutions for Adaptive and Wideband Radio Communication Circuits' starting from 1999. In addition, some financing was provided by the National Technology Agency TEKES in the project 'Programmable Radio Receivers' (ORAVAT). During 1995 – 1999, I had the privilege to attend the Graduate School on Electronics, Telecommunications and Automation (GETA), which enabled me to concentrate fully on post-graduate studies and to make university visits abroad. In the course of post-graduate studies, I have been fortunate to receive additional funding from several foundations acknowledged here: the Finnish Cultural Foundation, the Nokia Foundation, the Emil Aaltonen's Foundation, the Foundation of Technology and the Electronics Engineers' Foundation.

I want to express my gratitude to my supervisor, Prof. Veikko Porra for his guidance and contribution in the graduating process even when his schedule was tight. I would also like to thank Dr. Petteri Alinikula of Nokia Research Center who acted as my instructor when I started my career in our laboratory in 1993. He originally provided me with a subject that was broad enough for doctoral studies. Lic.Tech. Kari Stadius and me were the first RF students in the laboratory. We have worked together ever after and shared a working room almost all the time. Kari and I have had countless arguments on professional issues as well as others, which, I believe, have been beneficial for both of us. I warmly thank him for having borne with me all these years! Another colleague of mine, Lic.Tech. (diss.) Aarno Pärssinen, whose development from an apprentice to a master I have witnessed during these years, has always been an enthusiastic and supportive discussion partner, for which I am grateful. Besides, these two 'uncles' have been excellent lunch companions! Lic.Tech. Jan Riska has co-operated with me on the applications of the circuits; I thank him for that. Finally, the rest of the staff at our laboratory, both former and present, also deserves thanks for a pleasant and relaxed working environment.

In 1995 and 1996 I spent a total of seven months as a visiting researcher at University College London in England. The visit gave new perspectives and resulted in several papers in conferences and journals. I would like to thank doctors David Haigh and Danny Webster for their contributions and initiatives for a visit I made to Macquarie University in Sydney Australia in 1997.

I want to thank the pre-examiners Prof. Joseph Tauritz of University of Twente and Prof. Ian Robertson of University of Surrey for their contribution to the completion of this thesis.

Finally, I am deeply grateful to my parents Raija and Sakari and to my sister Raisa's family for their love and irreplaceable support in the moments of joy and success, as well as despair and disappointment. It has not always been easy to keep up the motivation but thanks to them I did not give up. To reach the final goal without them would have been very difficult and almost meaningless. The support of my dear relatives and friends will also be remembered.

In Tapiola, Espoo, October 2000

Risto Kaunisto

SYMBOLS AND ABBREVIATIONS

Symbols

A_1 , A_2	excitation voltage amplitudes in Volterra kernels
A_i	current gain
A_v	voltage gain
A_{filter}	filter pass-band loss
$B'(\omega_0)$	derivative of susceptance at center angular frequency
B_{in}	input susceptance
b_0 ,…, b_3	digital logic levels of a binary word
C_0	zero-bias capacitance
C_{01} ,…, $C_{n,n+1}$	coupling capacitances in coupled-resonator filters
C_{be}	base-emitter capacitance
C_c	coupling capacitance in second-order filters
C_g	gyrator capacitance
C_{gd}	gate-drain capacitance
C_{gs}	gate-source capacitance
C_{in}	input capacitance
C_p	parallel capacitance
C_{p1} , C_{p2}	parallel capacitances in two-ports
C_r	resonator capacitance
C_{r1} ,…, C_{rn}	resonator capacitances in coupled-resonator filters
C'_r	capacitance associated with the actual resonance in coupled-resonator filters
C_s	series capacitance
C_v	junction capacitance in varactors
c_0 , c_1 , c_2	coefficients in the power series approximation of non-linear capacitance
c_i	small-signal input capacitance
F	noise figure
F_1 ,…, F_n	block noise figures in a system
F_{filter}	filter noise figure
F_R	receiver noise figure
F_{tot}	total chain noise figure
f_0	center frequency
$f_{0,min}$, $f_{0,max}$	minimum and maximum center frequencies
f_{in}	input frequency
f_{LO}	local oscillator frequency
f_{max}	maximum oscillation frequency
f_{sr}	self-resonance frequency
f_T	transition frequency
G_0	characteristic conductance
G_1 ,…, G_n	block gains in a system
G_g	gyrator conductance
G_{FB}	feedback conductance
G_{in}	input conductance
G_l	load conductance
G_s	source conductance
G_{tun}	tuning conductance

g_0	small-signal output conductance
g_2 , g_3	coefficients in the power series approximation of non-linear transconductance
g_{2c} , g_{3c}	coefficients in the power series approximation of non-linear compound transconductance
g_b	small-signal base conductance
g_{ce}	small-signal collector-emitter conductance
g_{ds}	small-signal drain-source conductance
g_m	small-signal transconductance
g_n	relative noise conductance
g_{tot}	total small-signal conductance
H_1 , H_2 , H_3	Volterra kernels of order 1, 2 and 3
H_{iin}	Volterra kernel for input current
I_{-R}	current through negative resistance
I_{bias}	bias current
I_{Cp}	current through parallel capacitance
I_{Cs}	current through series capacitance
I_c	collector current
I_{dc}	DC operating current
I_{dss}	zero-bias drain current
I_{in}	input current
I_L	current through inductance
I_{Ls}	current through series inductance
I_{Lp}	current through parallel inductance
i_g	current through gyrator capacitance (AC component)
i_{in}	input current (AC component)
$i_{in,actind}$	active inductor input current (AC component)
$i_{in,negres}$	negative resistor input current (AC component)
i_{NL2} , i_{NL3}	second- and third-order non-linear current sources
i_o , i_{out}	output current (AC component)
k	Boltzmann constant $1.3807 \cdot 10^{-23}$ J/K
L_1 ,…, L_n	resonator inductances in coupled-resonator filters
L_{comp}	inductance due to compression
L_{fund}	fundamental-frequency inductance component
L_p	parallel inductance
L_s	series inductance
L_{super}	super-inductance
n	pn-junction grading factor
P_{IM3}	power of third-order intermodulation product
P_{in}	input power
Q	quality factor
Q_0 , Q_{res}	unloaded quality factor at resonance
$Q_{0,actind}$	active inductor unloaded quality factor
$Q_{0,noise}$	effective unloaded noise quality factor
Q_C , Q_{cap}	capacitor quality factor
Q_{C0}	process-defined capacitor quality factor
Q_{diff}	quality factor in differential resonators
Q_e	external quality factor
$Q_{max,C}$,$Q_{max,cap}$	maximum capacitor quality factor
$Q_{max,L}$,$Q_{max,ind}$	maximum inductor quality factor
Q_L , Q_{ind}	inductor quality factor

Q_{L0}	process-defined inductor quality factor
Q_l	loaded quality factor
q	elementary charge $1.6027 \cdot 10^{-19}$ C
R_0	characteristic resistance
R_{cap}	resistance associated with capacitance
R_{comp}	loss resistance due to compression
R_{ind}	resistance associated with inductance
R_l	load resistance
R_{leff}	effective load resistance after transformation
R_p	parallel resistance
R_{peff}	effective parallel resistance after transformation
R_{Qen}	Q-enhancing resistance
R_s	series resistance
R_{sens}	sensing resistance
$R_{small\text{-}signal}$	small-signal resistance
R_{so}	source resistance
r_i	small-signal input resistance
r_n	relative noise resistance
r_o	small-signal output resistance
S_{11} , S_{12} , S_{21} , S_{22}	s-parameters
$S(f)$	noise spectral density
T	standard temperature 290 K
t_{pd}	mean propagation delay time
V_{-R}	voltage across negative resistance
$V_{bias,f}$	frequency control voltage
$V_{bias,Q}$, V_{qb}	quality factor control voltage
V_C	voltage across capacitance
V_c	control voltage
V_{c+} , V_{c-}	positive and negative control voltages
V_{cc} , V_{dd}	positive supply voltage
V_{Cp}	voltage across parallel capacitance
V_{Cs}	voltage across series capacitance
V_{in}	input voltage
V_j	built-in junction potential
V_{Lp}	voltage across parallel inductance
V_{Ls}	voltage across series inductance
V_{out}	output voltage
V_{pp}	peak-to-peak voltage
V_{res}	voltage across a resonator
V_{ss}	negative supply voltage
V_T	thermal voltage 24.990 mV
V_t	threshold voltage
v_g	voltage across gyrator capacitance (AC component)
v_{in}	input voltage (AC component)
$v_{in,comp}$	input voltage at compression (AC component)
$v_{in,comp,actind}$	active inductor input voltage at compression (AC component)
$v_{in,comp,negres}$	negative resistor input voltage at compression (AC component)
$v_{in,comp,reson}$	resonator input voltage at compression (AC component)
Y_{diff}	differential admittance
Y_{in}	input admittance
Y_p	parallel admittance

$y_{11}, y_{12}, y_{21}, y_{22}$	y-parameters
y_{p1}, y_{p2}	parasitic gyrator port admittances
Z_{in}	input impedance
Z_{norm}	normalized impedance
Z_{out}	output impedance
Z_{res}	resonator impedance
Z_s	series impedance
W_{diss}	dissipated energy
W_{stored}	stored peak electromagnetic energy
$W_{stored,ind}$	stored peak magnetic energy
$W_{stored,cap}$	stored peak electric energy
w	relative angular frequency
α_n	n^{th} low-pass prototype filter component
β	current gain coefficient in bipolar transistors
γ	noise gamma coefficient
Δa	amplitude error
$\Delta\varphi$, $\Delta\phi$	phase shift, phase error
$\Delta\omega$	-3-dB angular bandwidth in second-order filters
τ	transit time
φ , ϕ	phase angle
ϕ_i	input phase
ϕ_o	output phase
$\varphi'(\omega_0)$	derivative of phase angle at center angular frequency
ω_0	center angular frequency
ω_1 , ω_2	excitation angular frequencies in Volterra kernels
$\omega_{L=0}$	angular frequency at inductance zero
ω_{LO}	local oscillator angular frequency
ω_{min}	minimum usable angular frequency
ω_{Qmax}	angular frequency for maximum quality factor
$\omega_{Qmax,C}$	angular frequency for maximum capacitor quality factor
$\omega_{Qmax,L}$	angular frequency for maximum inductor quality factor
ω_{self} , ω_{sr}	self-resonance angular frequency
$\hat{i}^2, \hat{i}_n^2$	noise spectral density current
$\hat{i}_c^2$	collector shot noise spectral density current
$\hat{i}_d^2$	channel thermal noise spectral density current
$\hat{i}_{in}^2, \hat{i}_{n,in}^2$	input-referred noise spectral density current
$\hat{i}_{n,A_i}^2$	noise spectral density current associated with current amplifier
$\hat{i}_{n,neg}^2$	negative resistor noise spectral density current
$\hat{i}_{n,res}^2$	resonator noise spectral density current
$\hat{i}_{n,Z}^2$	noise spectral density current associated with impedance
$\overline{v}^2$	total root-mean-square noise voltage
$\hat{v}^2, \hat{v}_n^2$	noise spectral density voltage
$\hat{v}_{gm}^2$	noise spectral density voltage associated with transconductance

$\hat{v}_{in}^2$, $\hat{v}_{n,in}^2$	input-referred noise spectral density voltage
$\hat{v}_{n,A_v}^2$	noise spectral density voltage associated with voltage amplifier
$\hat{v}_{n,Z}^2$	noise spectral density voltage associated with impedance
$\hat{v}_R^2$	noise spectral density voltage associated with resistance

Abbreviations

AC	alternating current
ACTRES	active resonator
Al	aluminium
APLAC	simulation software package by Aplac Solutions
BDR	blocking dynamic range
BFL	buffered FET logic
BiCMOS	bipolar and complementary-metal-oxide-semiconductor
BJT	bipolar junction transistor
BW	bandwidth
BW_{-3dB}	-3-dB bandwidth
bal	balanced
C-V	capacitance-voltage
CAD	computer-aided design
CCII	second-generation current conveyor
CD	common drain
CG	common gate
CLK	clock
COMP	compression
D	depletion-mode
DC	direct current
DCS	digital cellular system
DR	dynamic range
ECL	emitter-coupled logic
FDD	frequency division duplex
FET	field-effect transistor
GaAs	gallium arsenide
Gm-C	transconductance-capacitance
GMMT-F20	process technology provided by GEC-Marconi
GSGSG	ground-signal-ground-signal-ground
GSM	global system mobile
HBT	heterojunction bipolar transistor
HD_3	third-order harmonic distortion
I-V	current-voltage
IC	integrated circuit
ICP	input compression point
IF	intermediate frequency
IIP_3	third-order intermodulation distortion intercept point
IM	intermodulation
IM_3	third-order intermodulation distortion
ISM	industrial-scientific-medical

Im/Re	ratio of imaginary and real components
IQ	in-phase – quadrature-phase
IR	image rejection
LC	inductor-capacitor
LNA	low-noise amplifier
LO	local oscillator
MDS	Microwave Design System; simulation software package by Hewlett-Packard
MESFET	metal-extrinsic-semiconductor field-effect transistor
MIM	metal-insulator-metal
MMIC	monolithic microwave integrated circuit
MOS	metal-oxide-semiconductor
MRR	mirror-rejection ratio
NF	noise figure
NOR	not-or
OCP	output compression point
OTA-C	operational transconductance amplifier – capacitor
PIN	positive-intrinsic-negative
PLL	phase-locked loop
pn	positive-negative
RC	resistor-capacitor
RF	radio frequency
RFIC	radio-frequency integrated circuit
RLC	resistor-inductor-capacitor
rms	root mean square
RX	reception
SFDR	spurious-free dynamic range
Si	silicon
SiGe	silicon-germanium
TDD	time division duplex
TX	transmission
unbal	unbalanced
WCDMA	wide-band code-division multiple access

CONTENTS

1. INTRODUCTION

1.1 Motivation for the Thesis

The breakthrough of wireless personal telecommunication in recent years has created a demand for smaller and cheaper portable handsets. Much effort has been made to fulfil these requirements, often with success. The number of discrete components in a cellular telephone has shrunk into few integrated circuits in the base-band and IF-sections, the same applying to many parts in the RF section. Filters, however, have not been among those components.

RF filters are definitely the most difficult RF parts to be integrated. This is a serious disadvantage, as they appear in several locations in an RF front end. New radio architectures, such as direct conversion receivers, can possibly reduce the number of RF filters in the receiver chain but by no means dispense with them. Moreover, the high-quality passive filters are the most expensive and bulky individual components in the RF section, and they are cumbersome in automated manufacturing processes. Although integrated filters would rectify all these drawbacks, no commercially significant progress has been made in realizing them yet. The reason is clear: the current system specifications are too tight for active filters. Unlike their passive counterparts, active filters have noise and distortion; they consume power and need constant tuning for maintaining accuracy. High frequencies bring more problems, as traditional well-known design methods are not applicable: no high gain elements are available, and the clock frequency for discrete-time filters, such as switched-capacitor or switched-current filters, becomes impracticably high. On the other hand, distributed elements applicable at millimeter-wave integrated circuits, such as microstrip structures, are too large for integration in the frequency range concerned (< 5 GHz).

Active resonator filters seem to offer the best possibilities for monolithic high-frequency realizations. The objective of this study is to investigate the possibilities offered by integrated active resonators in microwave filter design, recognize their limitations and find potential applications in the field of mobile telecommunications. Different integrated circuit technologies have been probed in order to find the optimal performance for each technique.

Active resonators themselves are not by any means a new approach for filter synthesis. They have been reported throughout the short history of electronics. Due to their numerosity, it would be a tedious task to refer to them comprehensively, and they would have little relevance to this study. Some of the historic references will be given in the corresponding chapters, though. In the context of radio-frequency integrated circuits, active resonator topologies presented in the recent decade have more significance to this work, and the most significant scientific contributions to the subject will be discussed in further chapters. However, studies with practicable results and proper measured data are relatively few.

1.2 Research Contribution

Active resonators can be divided into two groups: passive LC resonators with active negative resistance compensation, and active inductor resonators. The theoretical and practical design issues of these approaches will be tackled in this thesis. Practical examples in the form of realized circuits will be given.

In the present study, all the different microwave negative resistor topologies are shown to derive from a single three-port. Thus, they can be categorized, and the common fundamental properties recognized. This has also given the motivation for comparison in terms of performance and feasibility. The emphasis is put on noise and distortion properties, as they are the main concern in applications. Consequently, gyrator-based active inductors are also

analyzed in detail. A method for understanding loss generation and its eventual cancellation with appropriate loop phase shift is presented.

A very typical misconception found in many papers is to regard active resonators as direct alternatives to passive resonators. This is the result of totally neglecting noise and distortion studies. By careful analyses, the author aims to give a realistic, although somewhat pessimistic, view of this issue. The author shows that simplified models for noise and non-linearity of transistors can be used as a basis for in-depth analyses. Although the absolute theoretical results give an optimistic view, their relative accuracy is good and useful for practical dimensioning, if permitted by the chosen process and practical issues. The Volterra-series method for calculating distortion responses is applied to the topologies, giving more understanding on the effect of each non-linear term.

Several active resonators and filters have been designed by the author, with the emphasis on low noise, low power consumption and small size. Different process technologies are experimented, and their suitability for active resonator design is assessed. Cellular phones are commonly regarded as potential applications for monolithic active filters. It is shown, however, that the noise and dynamic range performance of active filters cannot be adequate for direct replacement of passive filters in current cellular architectures. However, a new application for wireless systems, an LO signal generation circuit for direct-conversion transmitters, is presented. Two such circuits with promising measured performance have been designed and the results presented in the thesis.

The thesis concentrates on the analysis and the realization of negative resistors and active inductors in resonators only. It does not deal with other filter techniques, even if they were presently applicable to the frequency range in interest. Although important, the detailed analysis and the design of frequency-tuning devices, e.g. varactors, are also out of the scope of this work. The focus is on the core resonators and filters, and external tuning circuits are only briefly discussed.

Based on several projects at the Electronic Circuit Design Laboratory, the results have been published in numerous scientific journals and conference proceedings. References to these will be given in the appropriate locations in the text. The contribution of the author in these papers has been the theoretical background and all the practical designs of active resonator filters. Mr. Kari Stadius has participated in the practical design issues, and Prof. Veikko Porra and Dr. Petteri Alinikula have acted as project supervisors. In the course of doctoral studies, the author has visited University College London, where he has participated in the research team led by Dr. David Haigh. During the visit, the author has experimented with different resonator designs, which have been published in joint papers with Dr. Haigh's team.

The system considerations in Chapter 5 have been published in a joint paper of Dr. Alinikula and the author, where the former has contributed to the system aspects and the latter to the filter design issues. The GaAs version of the LO signal generation circuit has been developed in a laboratory project, where Mr. Jan Riska has been responsible for practical design of the circuits except for the band-pass filter. The author has been the project leader and in charge of the system design and the implementation of the band-pass filter. Prof. Kari Halonen and Dr. Alinikula have been the supervisors of the project. In the Si-BiCMOS version, Mr. Riska has designed the mixer with its auxiliary circuitry, whereas the authors contribution is in the frequency divider design, the filter and output buffer realizations, and the overall system design.

1.3 Organization of the Thesis

In Chapter 2, an introduction to passive resonator theory is given. It is essential to understand the definitions and the terminology of passive resonators prior to considering their active counterparts. The definition of quality factor is discussed in detail, as inconsistent definitions can be found in the literature. Noise properties and large-signal effects in passive

resonators and filters are discussed, as they form a reference for active designs. Also, a review of frequency tuning techniques for resonators is given.

Chapter 3 deals with the analysis and design of negative resistor resonators. The different topologies are categorized and their fundamental small-signal and tuning properties are derived. The emphasis is put on noise and distortion analyses and comparison of different negative resistor types, as they are the most limiting issues in practical filter design. The Volterra-series method is applied in the distortion estimations. At the end, realized negative resistor resonators are presented and their measured performance presented.

The subject of gyrator-based active inductor resonators is elaborated in Chapter 4. By utilizing the concept of loop phase error, the operation conditions for high-Q active inductors are derived, and the effects of tuning parameters studied. The noise and distortion performance is assessed in the same manner as with negative resistors, so that direct comparisons are possible. Finally, practical issues of gyrator inductor design and realized topologies with measured data are discussed.

In Chapter 5, the topic of active resonator filter design is tackled. Derived from the respective resonator results, the noise and dynamic range performance of the filters themselves are presented. Automated tuning techniques are introduced although their implementation is outside the scope of the thesis. Utilization of active filters in modern cellular systems is shown to be difficult but as a new potential application, an LO signal generation system employing a monolithic band-pass filter is presented for direct-conversion transmitters. The measurement results from two test circuits show that the concept is feasible.

Finally, Chapter 6 contains a summary of the work carried out in this thesis.

2. PASSIVE RESONATOR THEORY

2.1 General Definitions

For each active resonator, one can identify a passive equivalent at a given narrow frequency band. As the passive counterpart is without exception superior in terms of essential performance factors, such as noise and distortion, it forms a self-evident reference. Therefore, it is essential to first understand the behavior and performance limits of resonators generally before looking into active circuits. In view of active resonator design, this chapter gives a review of essential aspects of passive resonators, their quality factors, noise and tuning issues, and passive resonator filter design.

2.1.1 Series and Parallel Resonators

An electrical resonator is formed when devices capable of storing electrical and magnetic energy interact with each other. In electronics, such devices are capacitors and inductors. The two types of LC resonators are series and parallel resonators.

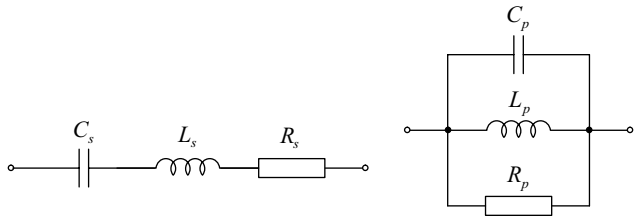

Figure 2.1 Series and parallel LC-resonators

If an LC resonator were ideal, i.e. lossless ($R_s = 0$, $R_p = \infty$), the electric and magnetic energy in its components would transform into each other in an oscillatory manner at the rate of ω_0 called the resonance frequency, when excited by a voltage (series resonators) or current (parallel resonators) impulse. In practice, passive resonators are never ideal, however, and possible initial oscillations are damped by the loss resistors R_s or R_p.

$$Z_s = R_s + \left(1 - \frac{\omega^2}{\omega_0^2}\right)\frac{1}{j\omega C_s}, \quad Y_p = \frac{1}{R_p} + \left(1 - \frac{\omega^2}{\omega_0^2}\right)\frac{1}{j\omega L_p}, \quad \omega_0 = 1\Big/\sqrt{L_{s,p}C_{s,p}} \tag{2.1}$$

When resonators are fed from an external source, they form a frequency-dependent network the impedance of which reaches its minimum (series resonators) or maximum (parallel resonators) at resonance. This feature is useful in designing frequency-selective circuits, such as filters. If used as a part of a passive filter circuit, a resonator is always loaded by surrounding components and source resistances, and even if the resonator is lossless, the circuit remains stable. In this case, an ideal resonator would give zero pass-band attenuation and lowest noise, which are naturally desirable properties for any passive filter. Thus, maximum-Q resonators are needed for good-quality filters.

2.1.2 Series-Mode and Parallel-Mode Transformations

As inductor losses are usually dominating in a monolithic resonator, all possible internal loss resistances are identified as inductor losses here. A lossy inductor can be defined with its loss resistance either in series or in parallel (or both) with the inductance. One can always transform a series-mode circuit into a parallel-mode circuit and vice versa:

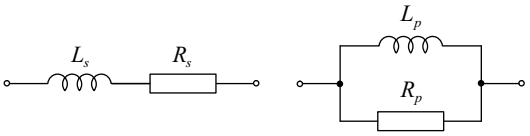

Figure 2.2 Series-mode and parallel-mode inductors

$$\begin{aligned} R_p &= R_s + \frac{\omega^2 L^2}{R_s} = R_s\left(1+Q^2\right) \approx R_s Q^2, \quad Q >> 1 \\ L_p &= L_s + \frac{R_s^2}{\omega^2 L_s} = L_s\left(1+ {}^{1}\!\!\diagup\!\!{}_{Q^2}\right) \approx L_s \end{aligned} \tag{2.2}$$

The quality factor of an inductor is a measure of its ideality; for a series-mode and a parallel-mode inductor it is defined as

$$Q = \frac{\omega L_s}{R_s} = \frac{R_p}{\omega L_p} \tag{2.3}$$

As the usage of (grounded) parallel resonators in monolithic band-pass filters is more feasible, and most active resonators are inherently parallel, I shall concentrate only on parallel-mode circuits from now on. Nevertheless, most calculations would apply directly to series resonators with little modifications.

2.1.3 Large-Signal Behavior

Within a resonator, very high voltage/current levels across the reactive components can be observed. In a series and parallel resonator, the voltage/current magnitudes over the inductor and the capacitor at resonance are

$$\begin{aligned} \left|V_{Ls}\right| = \left|V_{Cs}\right| &= Q_0 V_{in}, \quad I_{Ls} = I_{Cs} = {}^{V_{in}}\!\!\diagup\!\!{}_{R_s} \\ \left|I_{Lp}\right| = \left|I_{Cp}\right| &= Q_0 I_{in}, \quad V_{Lp} = V_{Cp} = R_p I_{in} \end{aligned} \tag{2.4}$$

when the resonator is excited by the voltage V_{in} (series resonators) or the current I_{in} (parallel resonators). This implies that series resonators suffer from internal voltage swings Q_0 times higher than the input voltage, the same applying to current swings in parallel resonators. If the voltage/current handling capability of the reactive components is limited, this leads to linearity problems. This will become an issue in high-Q filters if the resonators are active and thus more or less non-linear. For instance, a quality factor of 100 corresponds to 20-dB voltage/current peaking at the inductor terminals. If the resonator is loaded, the external loss can be included in R_s or R_p, and Equation (2.4) still applies.

2.2 Concept of Quality Factor

2.2.1 General Remarks

The concept of quality factor Q has often several interpretations, depending on the context. This will lead to confusion if the particular method of calculation is not revealed. There is, however, only one definition that is physically correct and applicable in most cases: the quality

factor of a system is the ratio of the stored energy and the dissipated energy per one frequency cycle in the system.

$$Q = 2\pi \frac{W_{stored}}{W_{diss}}\bigg|_{cycle} \tag{2.5}$$

This definition gives the two fundamental conditions where Q exists: the system must be able to store energy, i.e. it must contain reactive or reactance-simulating elements, and it must also be dissipative. For a system that produces energy, quality factor is not defined, as it would become negative ($W_{diss} < 0$). Therefore, in terms of the network theory, Q cannot be defined for an active circuit. The system can contain active components, i.e. transistors, but when looking inside through its terminals, it must act as a passive system.

W_{stored} in Eq. (2.5) describes the system's *capability* for storing energy, i.e. it is the peak value of either magnetic or electric energy, whichever is greater (I_L and V_C are the peak voltage and current applied to the component):

$$W_{stored,ind} = \frac{1}{2} L |I_L|^2, \quad W_{stored,cap} = \frac{1}{2} C |V_C|^2 \tag{2.6}$$

The peak energies become equal at resonance, and that is the point where the definition of W_{stored} changes (the magnetic energy becomes larger than the electric energy, or vice versa). W_{diss} is always the total dissipated energy during one cycle.

For a pure inductor in a parallel connection, Eq. (2.5) gives the familiar expression [2.1]:

$$Q = 2\pi \cdot \frac{V^2}{\underbrace{2\omega^2 L}_{W_{stored}}} \div \frac{2\pi}{\omega} \underbrace{\frac{V^2}{2R}}_{W_{diss}} = \frac{R}{\omega L} \tag{2.7}$$

Yue and Wong [2.1] suggest that for a realistic inductor with parasitic capacitances, a different definition of Q should be used. The parasitic electric energy would be counterproductive and finally cancel out the magnetic energy of the inductance, resulting in a quality factor of zero at self-resonance. Mathematically this corresponds to the widely used formula $Q = \mathrm{Im}\{Z\}/\mathrm{Re}\{Z\}$, where Z is the impedance of the inductor *with* parasitics. It can be contemplated that this ideal violates the fundamental principle in Eq. (2.5), though. There would be no energy stored at the self-resonance frequency, and it would be impossible to use the circuit as a resonator at that point if the inductor Q sank to zero at resonance.

Therefore, in order to preserve consistency with the fundamental quality factor definition, all practical inductors (or capacitors for that matter) should be identified as LC tanks. At low frequencies well under self-resonance, this is somewhat awkward, and Eq. (2.7) is quite an accurate approximation.

It is important to understand the distinction between the losses of an inductor and those of an LC tank. The inductor loss is attributed to the magnetic energy storage only, but the dissipation in a resonator consists of both magnetic and electric energy losses. Hence, if we talk about the *inductor* Q value in conjunction with a real-world inductor, the examination must be limited to low frequencies, and we must not take any eventual losses in parasitic capacitors into account. In other words, any change in the resistive behavior that is caused by parasitic capacitors does not affect the inductor Q but will change the resonator Q.

2.2.2 Resonator Q Factor

Theory

We can easily calculate the stored and dissipated energies with the aid of Eq. (2.6), and after some approximations ($\omega_0 \approx 1/LC^{1/2}$) get the following expression for the resonator Q, irrespective of the resonator type:

$$Q \approx \left(\frac{1}{Q_L} + \left(\frac{\omega}{\omega_0} \right)^2 \frac{1}{Q_C} \right)^{-1}, \quad \omega \le \omega_0$$
$$Q \approx \left(\frac{1}{Q_C} + \left(\frac{\omega_0}{\omega} \right)^2 \frac{1}{Q_L} \right)^{-1}, \quad \omega \ge \omega_0 \tag{2.8}$$

Exactly the same result can be obtained by reducing the circuit to one of the basic resonator types via the series-parallel or parallel-series transformations, and then determining Q in the conventional way (Eq. (2.3)). The results given by Eq. (2.8) are illustrated in Figure 2.3, where the quality factor of a typical parallel resonator with a series-loss inductor and capacitor is plotted.

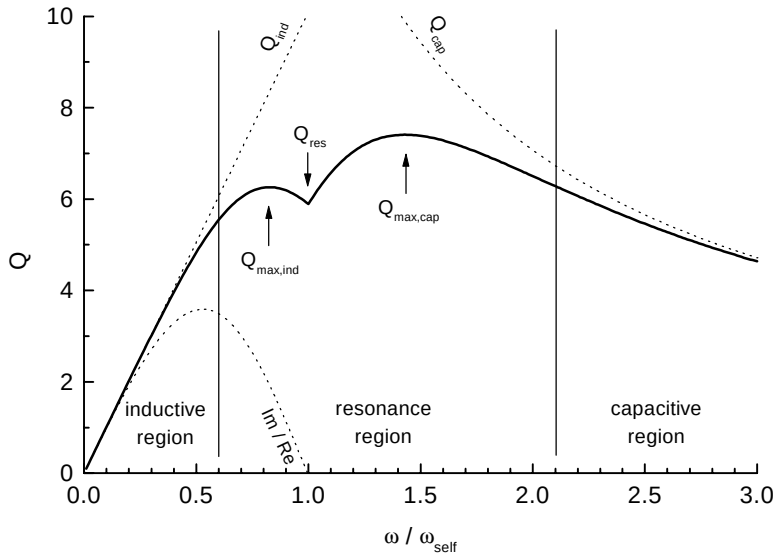

Figure 2.3 Quality factor of a parallel resonator with a series-loss inductor and capacitor. Pure inductor and capacitor Qs and the Im/Re ratio of the resonator are also plotted.

When the circuit is used in the inductive or capacitive region, its Q is directly the inductor Q or the capacitor Q itself, just like explained in the previous section. It is noteworthy to remark that the definition Im{*Z*}/Re{*Z*} gives a false approximation at the upper end of the inductive region.

In the resonance region Eq. (2.8) is the only valid definition of Q. It is interesting to remark that there is a maximum in both inductive and capacitive quality factors, and that this maximum does not necessarily stand at resonance. In the case of series-loss resonating components, the following relations apply:

$$\omega_{Q\max,L} = \omega_0 \sqrt{\sqrt{\frac{R_{ind}}{3R_{cap}}}}, \quad Q_{\max,L} = \frac{3}{4}\frac{\omega_{Q\max,L} L}{R_{ind}}$$
$$\omega_{Q\max,C} = \omega_0 \sqrt{\sqrt{\frac{3R_{ind}}{R_{cap}}}}, \quad Q_{\max,C} = \frac{3}{4}\frac{1}{\omega_{Q\max,L} C R_{cap}} \tag{2.9}$$

By adding a suitably sized high-Q capacitor to the circuit, it is possible to make $\omega_{Qmax,L}$ and ω_0 coincide and thus have the maximum available quality factor at resonance.

Practice

The previous studies are not necessarily easily applicable to a practical case. They assume that the loss resistance is constant over the frequency band in interest. In practice, however, it is dispersive, due to current crowding effects in the conductive materials. Moreover, in monolithic resonators the conductance of the semiconductor is frequency-dependent. The capacitive region can be difficult to characterize, as parasitic inductances may affect the measurements at high frequencies.

At resonance, it is possible to define the resonator Q value via measurements, though. It can be defined as the inverse of the resonator impedance -3-dB bandwidth (Figure 2.4):

$$Q_0 = \frac{R_p}{\omega_0 L_p} \approx \frac{\omega_0}{\Delta\omega} \tag{2.10}$$

If the resonator is loaded by a resistance R_l, the quality factor sinks to

$$Q_l = \frac{R_p R_l}{\omega_0 L_p (R_p + R_l)} = \left(\frac{1}{Q_0} + \frac{1}{Q_e}\right)^{-1}, \quad Q_e = \frac{R_l}{\omega_0 L_p} \tag{2.11}$$

where Q_l and Q_e are the 'loaded' and 'external' quality factors. For instance, if also the resonating capacitor is lossy, the total Q value of the resonator can be calculated from Eq. (2.11) where Q_e is the capacitor Q value.

If y_{11} of a resonator is known, e.g. from measurements, the unloaded quality factor can also be defined as

$$Q_0 = \frac{1}{G}\left(\frac{\omega_0}{2}\frac{\partial B}{\partial\omega}\bigg|_{\omega_0} - B\right), \quad G = \mathrm{Re}\{y_{11}\}, B = \mathrm{Im}\{y_{11}\} \tag{2.12}$$

because the slope of B at resonance equals $2C_p$ (Figure 2.5a). Perhaps a more elegant way of determining the resonator unloaded Q is to examine the derivative of phase at resonance:

$$Q_0 = \frac{\omega_0}{2}\frac{\partial\varphi}{\partial\omega}\bigg|_{\omega_0}, \quad \varphi = \arg(y_{11}) \tag{2.13}$$

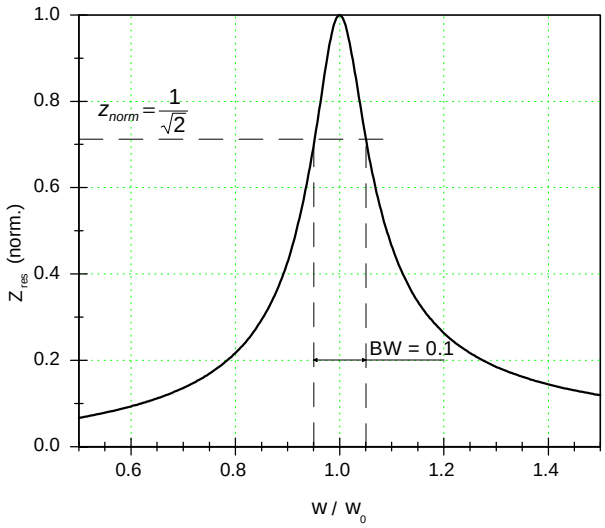

Figure 2.4 Magnitude of parallel resonator impedance; $\omega_0 = 1$, $Q_0 = 10$

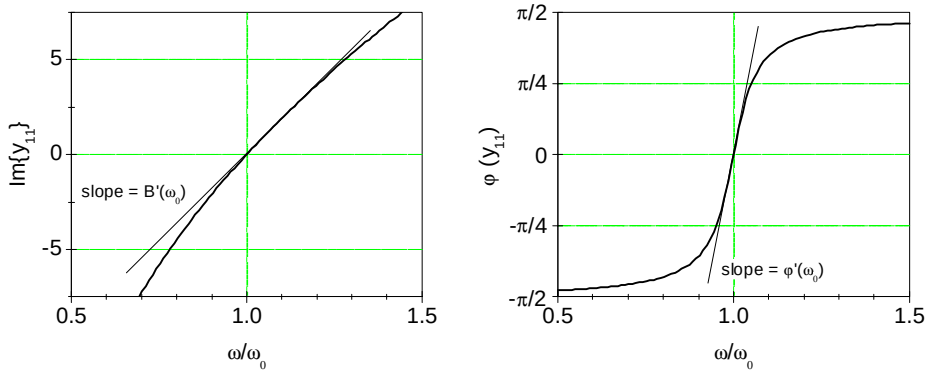

Figure 2.5 a) Resonator susceptance at resonance b) Phase of y_{11} at resonance

2.2.3 Q in Two-Port Circuits and Differential Resonators

Very often active resonators must be realized as differential circuits; many of the active resonator topologies are by nature differential. A differential resonator is fed by signals in 180° phase shift. In realizable circuits, they usually form a two-port; a typical example is shown in Figure 2.6. Actually, practical integrated inductors are similar two-port resonators. Defining Q for such a circuit is problematic, as it may vary depending on from which port it is measured (if the grounded capacitors are of different sizes). If the circuit is grounded from one end, it reduces to a one-port, and Q is easily attained, but the information on the capacitor at the grounded end is lost.

The solution to this problem is to regard the circuit as a differential one-port. The rest of the differential circuit regards the resonator as a normal parallel RLC resonator, as the ground level is floating in terms of the differential signal. For characterization a differential resonator is measured like an ordinary two-port in a single-ended environment, but the results must be manipulated to give the actual circuit parameters:

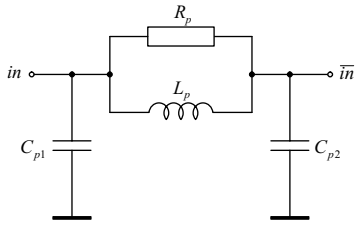

Figure 2.6 Differential resonator

$$Y_{diff} = \frac{y_{11}y_{22} - y_{21}^2}{y_{11} + y_{22} + 2y_{21}}, \quad y_{21} = y_{12} \tag{2.14}$$

Phase imbalance at the input results in changes in the functional quality factor of the differential resonator, although the actual Q, set by the component values, remains the same. If $\Delta\phi$ designates the phase deviation from the ideal 180°, the detectable Q value of the circuit becomes

$$\frac{1}{Q_{diff}} = \frac{1}{Q_0} + \left(1 - \omega_0^2 L_p C_p\right)\tan\frac{\Delta\phi}{2}, \quad Q_0 = \frac{R_p}{\omega_0 L_p} \tag{2.15}$$

In the case of a pure differential inductor (C_p = 0), the changes in Q are serious, as shown in Figure 2.7. Normal resonators where $\omega_0 = 1/(L_pC_p)^{½}$ are not affected by this phenomenon, though. As the phase error conceptually creates an extra reactive component, the resonance frequency is also changed, but at a small $\Delta\phi$ this is negligible.

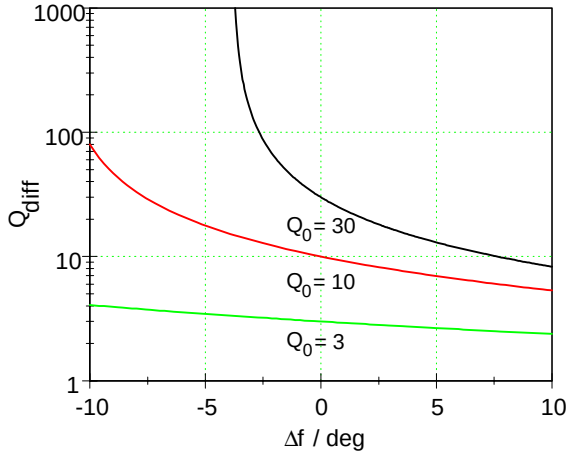

Figure 2.7 Differential Q

2.3 Passive Resonator Noise

The two quantities used in noise calculations are noise spectral density *S(f)* and total rms noise voltage $\bar{v}^2$. The former gives the noise voltage or current density at a certain bandwidth, usually 1 Hz. The latter gives the total noise voltage of the circuit over all frequencies limited by the transfer function. These two are related:

$$\bar{v}^2 = \int_0^\infty S(f)df \tag{2.16}$$

The noise spectral density *S(f)* generally gives more information about the resonator noise performance itself than the rms noise voltage (or current) $\bar{v}^2$. It is used for defining spot noise values near resonance, and consequently the filter noise figure. When defining the filter performance, the pass-band noise is most significant, but the total rms noise value does not give specific information on that. For instance, when the Q_0 of a passive resonator approaches infinity its spot noise at resonance goes to infinity at the same time, resulting in instability, but the total rms noise still gives a fixed value of *kT/C*, as illustrated in Figure 2.8.

Normally, the rms noise voltage is used in the system design, where the noise sources are wide-band but the output noise limited by filter transfer functions. It is assumed that the filters have only a band-shaping effect but not any noise contribution. This is not the case with active filters, where the filtering function itself is noisy. The total rms noise voltage is still needed in the dynamic range definitions, where the absolute maximum and minimum voltage levels across the resonator are studied.

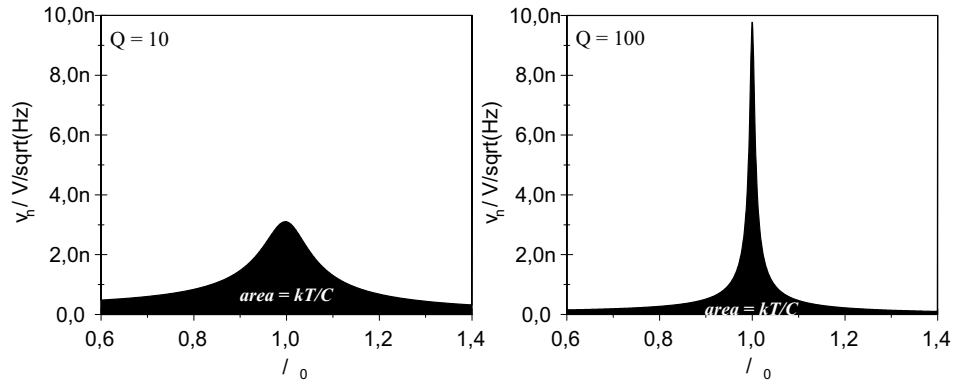

Figure 2.8 Noise spectral densities and total rms noise voltages of an unloaded resonator

I shall denote noise spectral density voltages (currents) as $\hat{v}^2$ ($\hat{i}^2$) hereafter for simplicity. A passive unloaded parallel resonator shown in Figure 2.9 contains only one noise source, namely the series resistance of the non-ideal inductor.

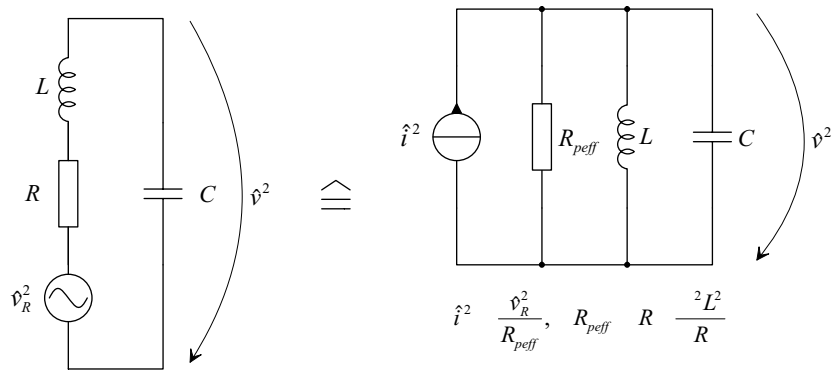

Figure 2.9 Passive unloaded resonator with noise sources

The noise voltage at the output node is the product of the noise source voltage and the noise transfer function:

$$\hat{v}^2 = \hat{v}_R^2\left[\left(1-\omega^2 LC\right)^2 + \omega^2 R^2 C^2\right]^{-1} = \frac{4kTR}{\left(1-\omega^2 LC\right)^2 + \omega^2 R^2 C^2} \tag{2.17}$$

At the resonance frequency ω_0 this yields

$$\hat{v}^2\Big|_{\omega_0} = \frac{4kT}{\omega_0^2 RC^2} = 4kTRQ_0^2 \tag{2.18}$$

Thus, the higher the quality factor of the resonator the higher the spot noise at resonance. Of course, if Q_0 were infinite the resonator would be in fact noiseless, since there would be no noise sources left. However, it would be unstable and bound to oscillate, which in turn can be imagined as infinite noise at a single frequency. The total rms output noise voltage of an unloaded resonator is

$$\begin{aligned}\bar{v}^2 &= \int_0^\infty \hat{v}^2 df = \frac{2kTR}{\pi}\int_0^\infty \frac{d\omega}{\left(1-\omega^2 LC\right)^2 + \omega^2 R^2 C^2} \\ &= \frac{2kTR}{\pi}\frac{\pi}{2}\frac{1}{RC} = \frac{kT}{C}\end{aligned} \tag{2.19}$$

which is the well-known formula for the noise of passive resonators, and in fact single-pole RC-filters as well.

If a resonator is to be used as a building block of a filter, it is always loaded by the source and load impedances and possibly other resonators. If the source and load impedances are capacitively coupled, as usual, the coupling capacitances can be embedded into the resonating capacitance after impedance transformation. The terminating impedances become transformed as well, and their values increase substantially. The transformation is frequency-dependent but fairly constant at a narrow bandwidth around the center frequency. The resulting circuit is shown in Figure 2.10.

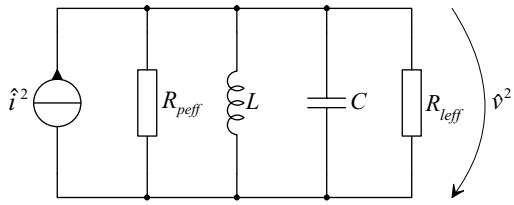

Figure 2.10 Passive resonator with loading

In order to facilitate further noise derivations, I shall use injected output noise current sources instead of output noise voltages, as the former are independent on loading. The injected output noise current of a passive resonator is

$$\hat{i}^2 = \frac{4kT}{R_{peff}} = \frac{4kTR}{R^2 + \omega^2 L^2}, \quad R_{peff} = R + \frac{\omega^2 L^2}{R} \tag{2.20}$$

where the effective parallel resistance R_{peff} is transformed from the actual series resistance of the inductor. Now, the noise spectral density at the output becomes

$$\hat{v}^2 = \hat{i}^2 |Z_n|^2 = \frac{4kTR}{\left(1 + R/R_l - \omega^2 LC\right)^2 + \omega^2 \left(RC + L/R_l\right)^2} \tag{2.21}$$

At resonance this yields

$$\begin{aligned} \hat{v}^2\big|_{\omega_0} &= 4kTR\left[\left(R/R_l\right)^2 + \omega_0^2\left(RC + L/R_l\right)\right]^{-1} = 4kTR\left[1/Q_0^2 Q_e^2 + \left(1/Q_0 + 1/Q_e\right)^2\right]^{-1} \\ &= 4kTR\left[1/Q_0^2 Q_e^2 + 1/Q_l^2\right]^{-1} \approx 4kTRQ_l^2 \end{aligned} \tag{2.22}$$

where Q_e is the external quality factor formed by loading, $Q_e = R_l/\omega L$, and Q_l is the loaded quality factor $1/Q_l = 1/Q_0 + 1/Q_e$. It can be seen that the noise is directly proportional to the load, i.e. a high Q_e imply high noise. As narrow-band filters have high effective source and load impedances, they inherently generate more noise. If the loading is zero ($Q_e = \infty$, $Q_l = Q_0$) the result is the same as in Eq. (2.18). For completeness, the total rms noise voltage is calculated below. Without loading, this yields *kT/C*, as previously.

$$\bar{v}^2 = \frac{2kTR}{\pi}\int_0^\infty \frac{d\omega}{\left(1 + R/R_l - \omega^2 LC\right)^2 + \omega^2\left(RC + L/R_l\right)} = \frac{kT}{C}\frac{1}{\left(1 + R/R_l\right)\left(1 + L/R_l RC\right)} \tag{2.23}$$

2.4 Resonators in Filters

2.4.1 Coupled Resonator Filters

Resonator band-pass filters are most straightforward to construct from capacitively coupled parallel resonators. The simplest possible second-order filter of this kind is shown in Figure 2.11. Higher order filters are formed by cascading multiple second-order blocks with altered capacitor values, corresponding to the desired prototype function.

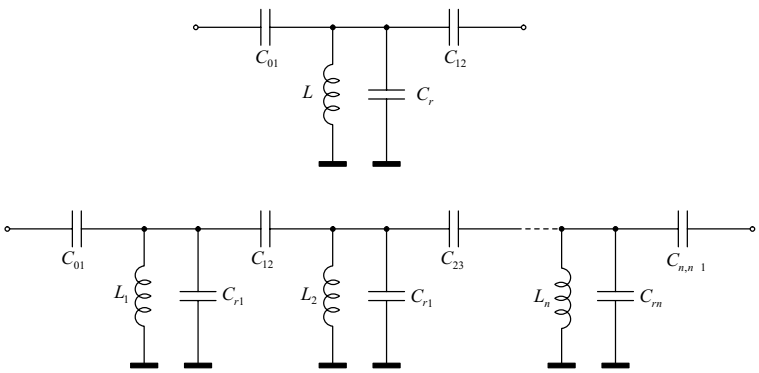

Figure 2.11 Coupled-resonator filters; second-order and n[th]-order

Dimensioning of coupled-resonator filters has been derived by Cohn [2.2]. The low-pass prototype filter parameters and types can be freely chosen and then translated into the band-pass coupled-resonator topology. For different filter functions (Butterworth, Chebyshev, Bessel etc.) and orders, prototype component values are listed in filter reference books, such as [2.3]. If α_n designates the n^{th} low-pass prototype component, the actual filter component values can be calculated from the set of equations (2.24):

$$
\begin{aligned}
&C'_{rk} = \frac{1}{\omega_0^2 L_k} \\
&C_{01} = \frac{1}{\omega_0}\sqrt{\frac{w' C'_{r1}/R_{so}\alpha_1}{1 - w' C'_{r1} R_{so}/\alpha_1}}, \quad C_{n,n+1} = \frac{1}{\omega_0}\sqrt{\frac{w' C'_{rn}/R_l\alpha_n}{1 - w' C'_{rn} R_l/\alpha_n}} \\
&C_{k,k+1} = \frac{w'}{\omega_0}\sqrt{\frac{C'_{rk} C'_{r,k+1}}{\alpha_k \alpha_{k+1}}}, \quad k \in [1, n] \\
&C_{r1} = C'_{r1} - \frac{C_{01}}{1 + \omega_0^2 C_{01}^2 R_{so}^2} - C_{12}, \quad C_{rn} = C'_{rn} - \frac{C_{n,n+1}}{1 + \omega_0^2 C_{n,n+1}^2 R_l^2} - C_{n-1,n} \\
&C_{rk} = C'_{rk} - C_{k-1,k} - C_{k,k+1}, \quad k \in [2, n-1]
\end{aligned}
\tag{2.24}
$$

w' is the angular -3-dB bandwidth of the filter ($\omega_2 - \omega_1$) if the prototype filter ω_0 is one, as usual, and R_{so} is the source resistance. For a narrow-band second-order (single-resonator) filter with equal terminations, the equations can be approximated as

$$
C'_r = \frac{1}{\omega_0^2 L}, \quad C_{01} = C_{12} \approx \sqrt{\frac{C'_r}{2\omega_0 Q_l R_{so}}}, \quad C_r \approx C'_r - 2C_{01} \tag{2.25}
$$

where $\alpha = 2$ (Butterworth response, $n = 1$) and $Q_l = \omega_0 / (\omega_2 - \omega_1)$ in second-order filters. The circuit looks like a loaded resonator with a loaded quality factor of Q_l.

2.4.2 Resonator Q versus Filter Q

The loaded quality factor of a resonator in a second-order band-pass filter is often called the filter Q. The filter Q is actually defined as the inverse of the relative bandwidth, and it is the same as the actual loaded Q of a single parallel resonator. It has no relation with the actual resonator Q in higher-order band-pass filters, though. Therefore, I will refrain from using this term hereafter.

2.4.3 Effective Termination Impedances

When the source or load impedance is raised, the corresponding coupling capacitor C_{01} or C_{12} diminishes, and eventually it can be omitted altogether. Generally, if the desired bandwidth can be achieved via the coupling capacitors without impedance transformation, their values become zero. Then the filter becomes simply a loaded parallel resonator the (loaded) Q of which is determined by the source and the load. This is the case when the resonator is coupled with buffer circuits instead of capacitors (Figure 2.12). The advantage of this topology is that no impracticably small coupling capacitors are needed, even if Q is very high. However, noise and linearity properties are impaired due to limitations in the active buffer circuits.

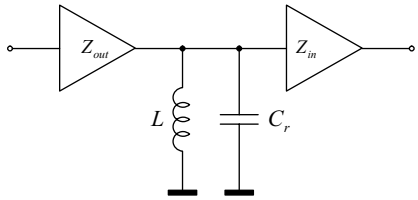

Figure 2.12 Buffered resonator

2.4.4 Noise in Resonator Filters

Since the calculation of noise performance becomes increasingly difficult when the number of resonators rises, I shall confine to single-resonator second-order filters only. The fundamental noise characteristics observed are nevertheless universal.

The most convenient and most widely used quantity for describing noise performance of a microwave filter is noise figure F. By definition, it is the ratio of the signal-to-noise ratios at input and output, or the total input referred noise level compared to the source noise level at the standard temperature T = 290 K. Usually, noise figure is expressed as spot noise figure at a defined bandwidth, usually 1 Hz. Both input noise voltages and currents can be used:

$$F = \frac{4kTR_{so} + \hat{v}_{in}^2}{4kTR_{so}} = 1 + \frac{\hat{v}_{in}^2}{4kTR_{so}} = 1 + \frac{\hat{i}_{in}^2}{4kT} R_{so} \tag{2.26}$$

The input referred noise current $\hat{\imath}_{in}^{\,2}$ is attained by reducing the resonator injected noise current to the input. Using the formulation of C_c given in Eq. (2.24), it becomes at resonance

$$\hat{i}_{in}^2 = \left(1 + \frac{1}{\omega_0^2 R_{so}^2 C_c^2}\right)\hat{i}^2 = \alpha \frac{\hat{i}^2}{\Delta\omega C_r' R_{so}} \tag{2.27}$$

Now, the spot noise figure of a single-resonator filter at the center frequency is

$$F = 1 + \frac{\hat{i}_{in}^2}{4kT} R_{so} = 1 + \alpha \frac{\hat{i}^2}{4kT\Delta\omega C_r'} \tag{2.28}$$

Notably, the contribution of the source impedance disappears. However, if R_{so} alone is changed $\Delta\omega$ will also change and alter the noise level.

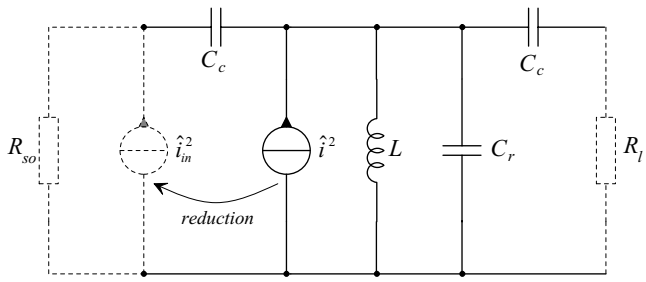

Figure 2.13 Second-order coupled resonator band-pass filter

By Eq. (2.20) the resonator noise current is

$$\hat{i}^2 = \frac{4kTR}{R^2 + \omega_0^2 L^2} \approx 4kT \frac{\omega_0}{Q_0} C_r', \quad Q_0 >> 1 \tag{2.29}$$

Thus, the spot noise figure of a high-Q passive resonator filter becomes

$$F = 1 + \alpha \frac{\omega_0}{\Delta\omega} \frac{1}{Q_0} \quad \text{or} \quad F = 1 + \alpha \frac{Q_l}{Q_0} \tag{2.30}$$

where Q_l corresponds to the termination-loaded quality factor of the resonator. The result clearly proves the importance of high quality inductors in passive resonator filters. Figure 2.14 shows how the filter noise figure behaves, when the inductor Q_0 is varied in the range of typical integrated spiral inductors and the -3-dB bandwidth if kept constant as 10%.

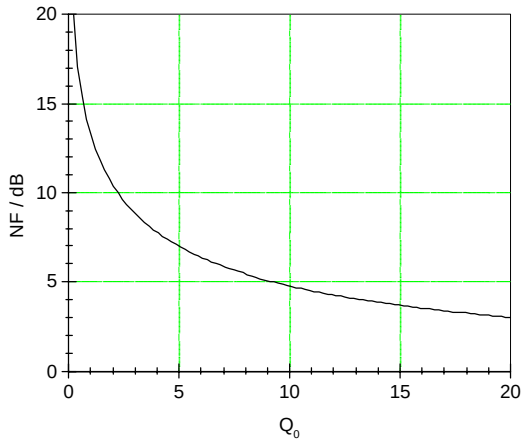

Figure 2.14 Passive resonator Q_0 vs. noise figure

The relative bandwidth of the filter is an equally important factor for noise performance, but usually it is fixed by the specifications and cannot be freely enlarged.

In a realistic resonator, both the inductor and the capacitor are non-ideal, and the expression for noise becomes respectively

$$F = 1 + \alpha Q_l \left(1/Q_L + 1/Q_C \right) \tag{2.31}$$

where Q_L and Q_C are the inductor and capacitor (varactor) quality factors. For instance, with typical integrated good-quality inductor/varactor Q values of 15, the absolute minimum noise figure with noiseless compensation of Q would be as high as 9.6 dB for a second-order filter, when targeted to the Bluetooth system as a potential exemplary application (f_0 = 2.44 GHz, BW_{-3dB} = 80 MHz). Thus, for low-noise operation at narrow bandwidths, it would be imperative to have passive resonating components of virtually unrealistically high quality in the first place.

Since the inductor and capacitor quality factors are proportional to frequency, filters with higher center frequencies have lower noise figures. Therefore, coupled-resonator filters are especially suitable for microwave frequencies, provided that the self-resonance of the individual components will not yet affect their quality factors at the filter center frequency.

In a higher-order filter the individual noise sources each contribute to lower noise levels than in a second-order single-resonator filter, since the resonators load each other. Coupling

between the resonators is, however, so weak that the total noise of the filter is always higher than that of a single-resonator filter with the same bandwidth.

In the previous studies, the resonators are assumed noisy but lossless, which is naturally impossible as far as passive resonators are concerned. Any loss resistance in the resonators will change the transfer characteristics of the filter and increase its pass-band loss, as well as induce noise to the system. However, in active resonator filters the situation is quite like discussed here: the active resonator is designed for zero-loss, but active components will introduce some excess noise.

As far as system noise properties are concerned, also the loss of the filter is significant. Even if the filter were practically noiseless, its loss would still degrade the total system noise figure, especially if it is located first in the chain. According to Friis's formula, the system noise figure is in this case (A_{filter} is the filter loss)

$$F_{tot} = F_{filter} + A_{filter}\left[(F_2 - 1) + \frac{(F_3 - 1)}{G_2} + \frac{(F_4 - 1)}{G_2 G_3} \ldots + \frac{(F_n - 1)}{G_2 G_3 \ldots G_{n-1}}\right] \tag{2.32}$$

A high filter pass-band loss will set greater noise performance demands on the following system blocks. The strength of active filters is that their losses can easily be cancelled, or even better, they can have gain. In a system, an active resonator filter with a 10-dB noise figure but zero loss as good as a passive filter with a 5.9-dB noise figure and loss, if F_2 = 5 dB and the following stages are ignored.

2.4.5 Large-Signal Effects in Resonator Filters

A passive resonator is practically linear. Only the hysteresis phenomenon in the inductor might attribute to non-linearity at very high signal levels. However, in the context of active resonator filters, it is necessary to understand how the filtering function affects the large-signal performance of the system.

In a second-order coupled-resonator filter (Figure 2.11a) the voltage level across the resonator is

$$V_{res} = V_{in}\sqrt{\frac{Q_l}{2\omega_0 C_r' R_{so}}} \tag{2.33}$$

using the same markings as in Eq. (2.25). The expression shows clearly how large an effect the quality factor has on the voltage peaking at the resonator terminals. If the loaded Q is doubled (the bandwidth halved) and the rest of the parameters remain unchanged the resonator voltage level is increased 3 dB. Or correspondingly, the highest allowed input level is decreased 3 dB if the resonator large-signal properties are kept constant. It is also worth noticing that large source (and load) resistances give better large-signal performance.

Compression in active resonators shows itself in diminishing unloaded quality factors compared to the small-signal values. This has effect on both the filter bandwidth and pass-band loss. The latter directly attributes to the compression point of the whole filter. The Q degradation can be understood as an increase of loss (a decrease of current at the fundamental frequency) when part of the response current is transferred to higher harmonic frequencies. If the total (parallel) loss resistance due to compression is marked as R_{comp}, the output voltage of the second-order filter becomes

$$V_{out} = \frac{V_{in}}{2}\left(1 + \frac{Q_l}{\omega_0 C_r' R_{comp}}\right)^{-1} \tag{2.34}$$

-1-dB output voltage compression takes place when

$$\frac{Q_l}{\omega_0 C_r' R_{comp}} \approx 12\% \tag{2.35}$$

If Q_l is low a relatively small R_{comp} can be tolerated. Or, on the other hand, voltage peaking at the resonator input is low, resulting in a high R_{comp} at that particular input voltage.

In band-pass and low-pass filters, harmonic distortion has practically no effect, as the harmonic distortion components are located clearly out of the band. However, third-order intermodulation distortion can be detected, when the two excitation frequencies and the intermodulation products are very close to each other at the pass-band. In very narrow-band filters, the two frequencies are practically equal, and the IM response is identical with the compression response.

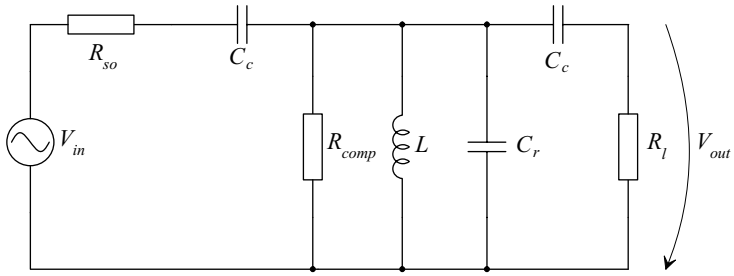

Figure 2.15 Second-order resonator filter with compression resistance

2.5 Frequency Control of Resonators

Precise control of the monolithic filter center frequency necessitates tunable resonators, since absolute component values are inaccurate in the presence of process variations. The resonance frequency of a passive resonator is defined by its LC product, and the only way to change it is to alter either the inductance or the capacitance. A passive tunable inductor is impossible to realize as an integrated circuit, whereas the varactor diode, although often regarded as an active element, functions as an electrically tunable passive capacitor. With the help of transistors, techniques like impedance multiplication or current steering can be adopted for transforming a constant passive capacitor or inductor into a variable one. This section introduces the most used frequency control techniques.

2.5.1 Varactor diodes

When a pn-junction diode is reverse-biased, its depletion capacitance can be controlled with the bias voltage. Especially, if the diode is optimally designed for this purpose, i.e. to give maximal capacitance per device area and large tuning range, it is called a varactor. For RF frequencies, a varactor looks like a series connection of a capacitor and a resistor (Figure 2.16). The resistor corresponds to the contact and intrinsic resistances in the semiconductor. It is responsible for the quality factor degradation and the noise of the varactor. A monolithic varactor also suffers from parasitic capacitances to the substrate, which somewhat cuts down

the tuning range. Extrinsic inductances set the upper frequency limit after which self-resonance will occur. In conventional integration processes, the base-emitter/collector junction of a bipolar transistor may be used as a varactor although not especially optimized for that purpose.

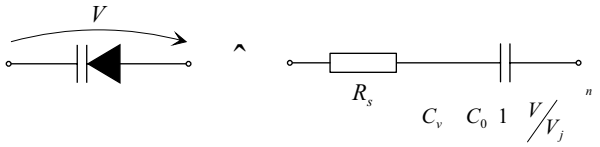

Figure 2.16 Varactor and its equivalent circuit

Typical tuning curves of a pn-varactor are shown in Figure 2.17 [2.5]. The incremental resistance of the increasingly conducting diode accounts for the fall of the quality factor curve towards positive bias voltages. The best Q value is attained at high reverse-bias conditions.

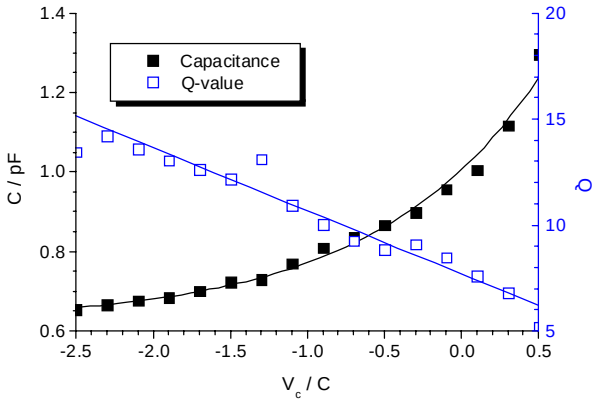

Figure 2.17 Measured capacitance and Q-value from an 8-ruple BJT base-emitter-diode varactor at 2 GHz (0.8-µm BiCMOS process)

Noise

The noise generation mechanism in a reverse-biased varactor diode is very much similar to that in a normal lossy capacitor or inductor. As the DC current through the device is negligible, only thermal noise is present, and it can be directly attributed to the series resistor of the equivalent circuit. Therefore, in a resonator filter a varactor behaves like stated in Eq. (2.31).

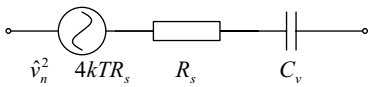

Figure 2.18 Noise equivalent circuit of a pn-varactor

Distortion

The depletion capacitance of a pn-varactor is usually formulated as

$$C_v = \frac{C_0}{\left(1 + V/V_j\right)^n} \tag{2.36}$$

where the grading factor n can vary from conventional 0.4 to hyper-abrupt 1.6. C_0 is the zero-bias capacitance and V_j the built-in potential of the junction. The expression in clearly non-linear, and hence pn-varactors are distortion-generating components. Meyer and Stephens [2.4] have analyzed distortion in varactor diodes utilizing the Volterra series method. According to their study, the third-order intermodulation and the compression ($\omega_0 \approx \omega_1 \approx \omega_2$) components of both series and parallel resonators with varactors can be expressed as

$$P_{IM3} = P\frac{Qc_2}{2\omega_0 c_0^2}\left(1-\frac{2n}{1.5(n+1)}\right), \quad C_v \approx c_0 + c_1 v_{in} + c_2 v_{in}^2 \tag{2.37}$$

where P is the average power in the loss resistor. Equation (2.37) suggests that it would be possible to null IM_3 with the particular value of n = 3. The zero is quite sharp, though, and impractical to realize.

Multiple-varactor connections can be used for enhancing greatly distortion performance. They are particularly suitable for differential resonators owing to their antisymmetry and cancellation of even harmonic components. The two types of connections, back-to-back and antiparallel, are shown in Figure 2.19:

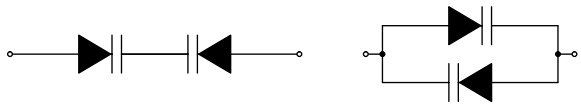

Figure 2.19 Back-to-back and antiparallel varactors

It is shown in [2.4] that the antiparallel connection is inferior, as its IM_3 is higher than that of a single varactor. It is also more difficult to arrange its biasing in practice. The back-to-back connection halves the voltage swing over individual diodes, and therefore distortion is also reduced. Moreover, it can be shown that if n = 0.5 for matched diodes, which is often the case, the third-order distortion term approaches zero. The drawback is the halved total capacitance value necessitating double-sized devices, when compared to single varactors of the same net capacitance.

2.5.2 Impedance multiplication

An impedance multiplicator consists of a passive component, usually a capacitor, whose voltage or current is sensed and multiplicated by an appropriately selected amplifier. By changing the gain of the amplifier, the net impedance of the circuit becomes variable. Depending on the type of the amplifying element, impedance multiplicators are either series- or parallel-mode circuits shown in Figure 2.20. The circuits can also transform a positive impedance into negative if the gain sign (inverting – non-inverting) is changed.

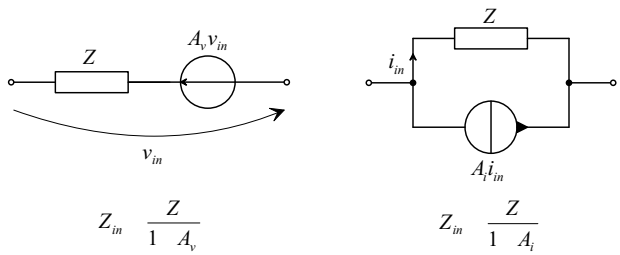

Figure 2.20 a) Series-mode impedance multiplicator with voltage amplifier;
b) Parallel-mode impedance multiplicator with current amplifier

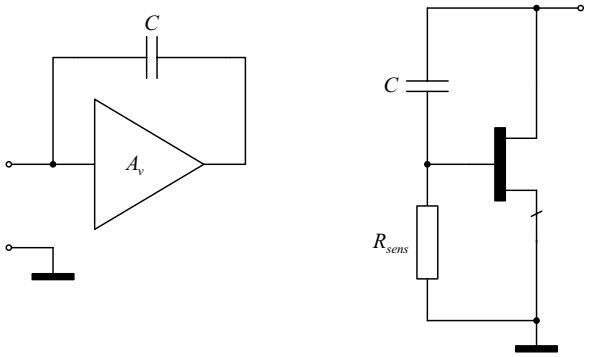

Figure 2.21 a) Miller circuit for capacitance multiplication;
b) Parallel transconductor capacitance multiplier

Usually the circuits are applied to capacitance synthesis because of the easy practical implementation and the fact that the resulting capacitance values become larger than the original. The series-mode circuit with a capacitor is also known as the Miller capacitance circuit [2.5]. Parallel-mode multiplication circuits have been reported e.g. in [2.6].

In practical implementations, the non-idealities of the controlled sources, especially non-zero output impedances, limit the performance of the impedance multiplication circuits. The input and output resistances of the voltage amplifier directly diminish the quality factor in the Miller capacitance circuit, and the same applies to the parallel multiplicators. In addition, the current amplifier in the parallel circuits must be realized as a transconductor with a current-to-voltage transformer, which, in the simplest form, implies a current-sensing resistor R_{sens} in series with the actual multiplicated impedance. This resistor has usually a dramatic reductive effect on the circuit Q.

High-frequency properties of impedance multiplicators are very much dependent on the bandwidth of the voltage or current amplifier. Near-ideal performance is usually obtained only at relatively low frequencies. With the same process parameters, amplifier-based impedance synthesizers have always more limited operating bandwidths than varactor diodes.

Noise and Distortion

In impedance multiplication circuits noise is generated by the multiplicated impedance itself and by the active amplifier circuit. The noise sources of the passive impedance – if existent – are also multiplicated by the same factor, and the resulting noise contribution corresponds to that of the passive impedance of the multiplicated value. The difference between the circuit types can be found in the active circuit noise that is also transformed in the series topologies, but left unchanged in the parallel circuits. This is a result of the circuits not being strictly dual, as the control quantities are taken from different locations due to practical issues. This has a major effect on the equivalent input noise that is lower in the parallel-mode impedance multiplicators. However, the need of current sensing resistance in practical parallel realizations causes severe noise performance degradation.

The large-signal performance of an impedance multiplication circuit is determined by the linearity of the active device/circuit. Where a current sensing resistor is required, its value has also effect on distortion: a smaller resistor gives lower distortion, as the amplifier input voltage is diminished.

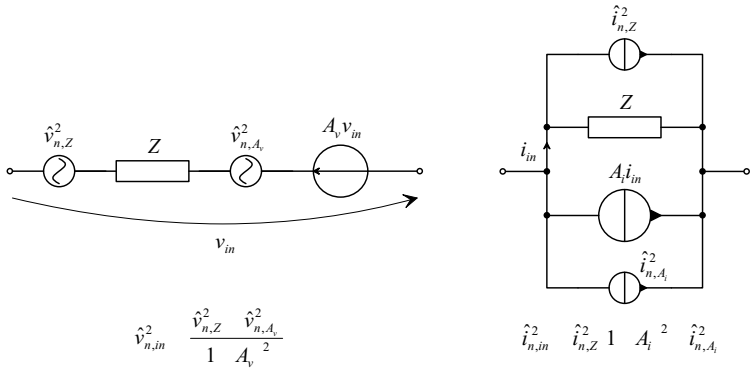

Figure 2.22 Noise mechanisms in impedance multiplication circuits

2.5.3 Current Steering

The differential Gilbert analog multiplier configured as a variable-gain amplifier can be used for synthesizing variable impedances [2.7]. Multiplication is arranged by summing complementary signal currents via controllable current splitters. The multiplicated impedance is easily inserted as a series-feedback component (Figure 2.23).

The fundamental drawback with this approach is the inherent loss resistor formed by the transconductance of the amplifying transistor. Together with parasitics and losses in the switching transistors, it will clearly reduce the achievable Q factor.

Noise and distortion properties can be directly derived from those of the analog multiplier core. Compared to the impedance multiplicators, the presence of the series steering transistors will unavoidably increase noise and somewhat worsen the large-signal properties.

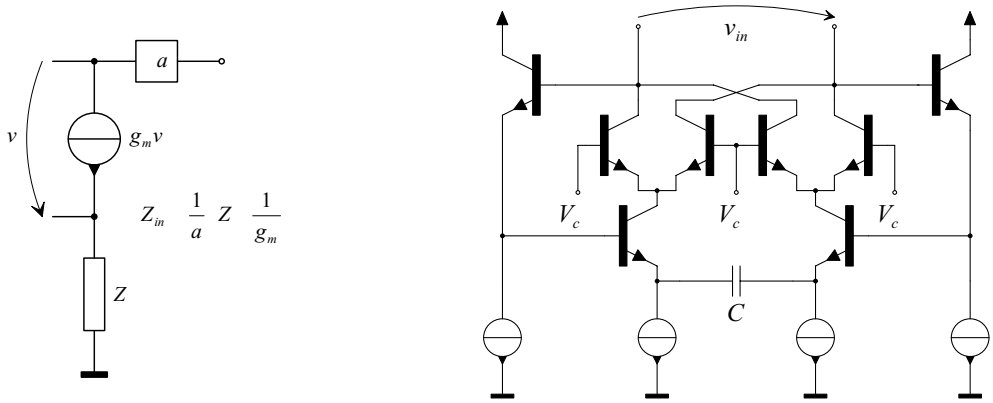

Figure 2.23 Variable impedance based on Gilbert analog multiplier; the principle and the differential implementation [2.7]

2.5.4 Capacitance Matrices

A capacitance matrix is a convenient method of controlling digitally the resonance frequency of an LC-resonator. It consists of suitably sized passive capacitors that are connected in parallel via solid-state switches. For instance, by using binary-weighted capacitor values a four-bit controlling word can tune the total capacitance in 16 discrete steps (Figure 2.25).

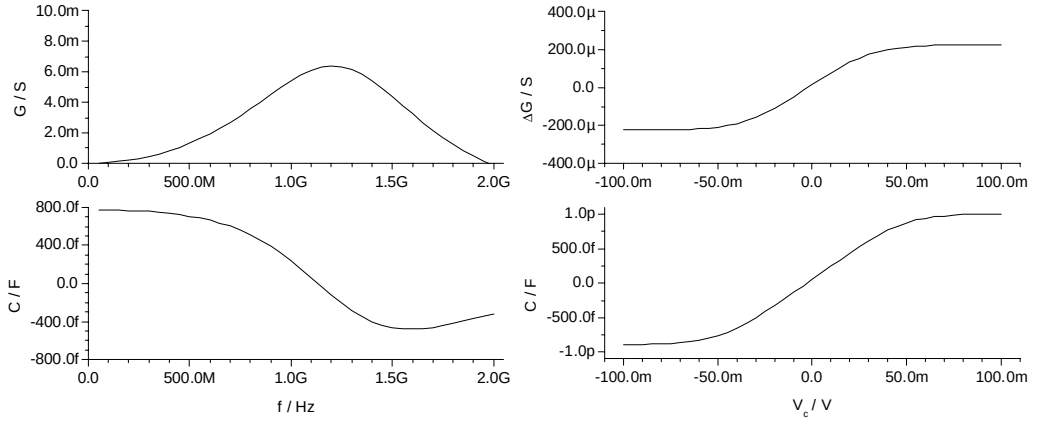

Figure 2.24 Simulated parallel conductance and capacitance of a current-steering capacitor as functions of frequency (V_c = 50 mV) and controlling voltage (f = 1 GHz), 0.8-µm BiCMOS process

The quality factor, as well as the noise performance of a capacitance matrix, is limited by the losses in the switch transistors. Large-signal properties are also inferior to a passive capacitor alone due to the solid-state switches, but still better than in active capacitance synthesizers.

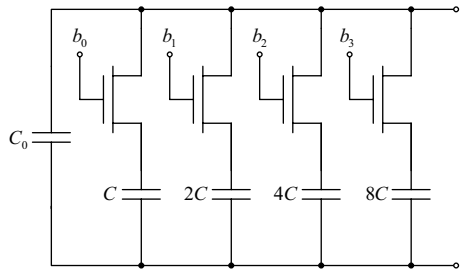

Figure 2.25 Capacitance matrix

References

[2.1] C. Yue and S. Wong, 'On-Chip Spiral Inductors with Patterned Ground Shields for Si-Based RF IC's,' *IEEE Journal of Solid-State Circuits*, Vol. 33, pp. 743-752, May 1998.

[2.2] S. Cohn, 'Direct-Coupled-Resonator Filters', *Proceedings of the IRE*, Vol. 45, pp. 187-196, February 1957.

[2.3] A. Zverev, 'Handbook of Filter Synthesis,' John Wiley, New York, 576 p., 1967.

[2.4] R. Meyer and M. Stevens, 'Distortion in Variable-Capacitance Diodes,' *IEEE Journal of Solid-State Circuits*, Vol. 10, pp. 47-54, February 1975.

[2.5] K. Stadius, R. Kaunisto and V. Porra, 'A High Frequency Harmonic VCO with an Artificial Varactor,' *Proceedings of IEEE International Conference on Electronic, Circuits and Systems*, Lisbon Portugal, Vol. 3, pp. 161-164, September 1998.

[2.6] S. Pipilos, Y. Tsividis, J. Fenk and Y. Papananos, 'A Si 1.8 GHz Filter with Tunable Center Frequency and Quality Factor', *IEEE Journal of Solid-State Circuits*, Vol. 31, pp. 1517-1525, October 1996.

[2.7] W. Chen and J. Wu, 'A 2-V 2-GHz BJT Variable Frequency Oscillator,' *IEEE Journal of Solid-State Circuits*, Vol. 33, pp. 1406-1410, September 1998.

3. NEGATIVE RESISTOR RESONATORS

3.1 Historical Perspective

The concept of using positive feedback to increase the quality factor of a resonator actually dates from the early years of radio electronics itself. It was introduced in the regenerative receiver which was independently discovered by de Forest, Armstrong, Langmuir and Meissner in 1912, but only Armstrong was given the full credit [3.1][3.2]. Only in 1934 the case was settled in de Forest's favor, but by that time the regenerative receiver had been made obsolete by improved receiver techniques, such as the superheterodyne technique.

In regenerative receivers, the amplified received voltage is fed back to the input circuit in such a phase that causes voltage increase at the input. This decreases the effective resistance of the input circuit and thereby provides greater amplification and selectivity for the input signal [3.3][3.4]. Regenerative receivers were, however, subject to oscillation if the feedback was increased beyond a certain point, causing serious interference to nearby receivers. Along with difficult controllability, this made regenerative receivers gradually loose their popularity.

The regenerative principle has lived through to our days in modern integrated resonators. They still rely on the same principle, positive feedback, in one form or another, although it always brings up the risk of instability. In fact, a high-Q active resonator operates on the brink of oscillation, which naturally sets high demands on the controlling circuit accuracy.

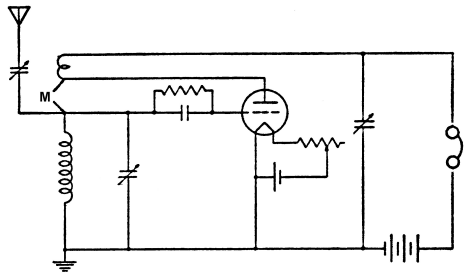

Figure 3.1 Armstrong's regenerative receiver [3.3]

3.2 General Definitions

By definition, a negative resistor is a circuit element where voltage applied across its terminals creates in-phase current of the opposite direction. Apart from few exceptions (e.g. tunneling diodes), this functionality requires controlled sources, i.e. transistors, in the realizations. High-frequency negative resistors are typically one- or twin-transistor circuits with suitable feedback components. Their response is, however, never purely resistive due to built-in parasitic reactive components. These can be embedded into the actual resonating elements, but due to series-parallel transformations, the resistive part often becomes frequency-dependent. In addition, bandwidths of the active devices are limited resulting in similar effects. Different negative resistor topologies have inherently different noise and distortion properties, and some are practically more suitable for integrated circuits than others.

An active negative resistor resonator is formed by a passive inductor-capacitor LC resonator and an active negative resistor circuit that compensates the resistive losses. It is most straightforward to connect the negative resistor directly to the loss resistor in such a way that it entirely cancels the loss at all frequencies. In other words, by connecting a negative resistor of suitable magnitude in series with the series loss resistance or in parallel with the parallel loss

resistance. Unfortunately, this is not always possible in practice, as there is usually no single definite loss resistance in an LC resonator, and it would be impractical to compensate them each with separate negative resistors. It is still possible to cancel the losses with a single negative resistor, but only at a narrower bandwidth.

3.2.1 Series and Parallel Compensation

Regardless of the resonator type, there are two approaches for compensating the resonator internal losses: series compensation and parallel compensation. Obviously, in the series compensation method the negative resistor is connected in series with the resonator, and respectively, in parallel compensation it is in parallel with the resonator. Intuitively, it is clear that series compensation is more suitable for series LC resonators and parallel compensation for parallel resonators, but there are also other issues to be considered.

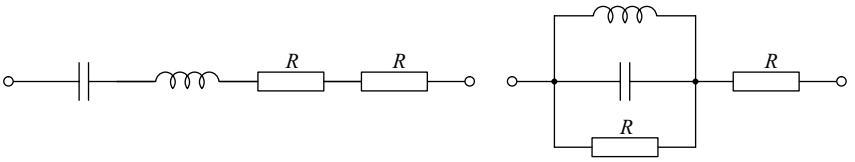

Figure 3.2 Series compensation method

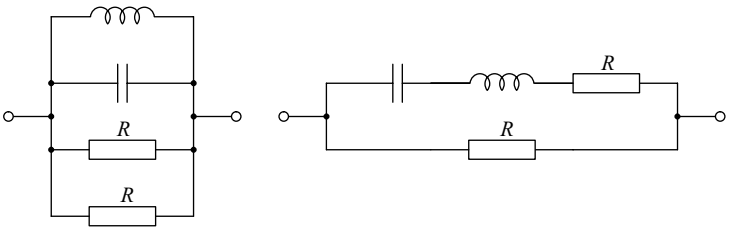

Figure 3.3 Parallel compensation method

Figure 3.2 shows the principle of series compensation for both series and parallel LC resonators. The net loss of the resonator is described by a single frequency-dependent resistor R which is then cancelled by a negative resistor of equal size. If we calculate the voltage and the current across the negative resistor at resonance, when external current I_{in} is applied across the whole circuit, we get

$$V_{-R} = -RI_{in}, \quad I_{-R} = I_{in} \tag{3.1}$$

Respectively, in Figure 3.3 the parallel compensation scheme is illustrated. Now, at external voltage V_{in}, the voltage and the current of the negative resistor at resonance are

$$V_{-R} = V_{in}, \quad I_{-R} = V_{in}/-R \tag{3.2}$$

Thus, series resonators are current driven and parallel resonators voltage driven. It is reasonable to say that active negative resistors stand up with large voltage swings better than large current swings, when current non-linearities are dominant in the transistors. For practical performance issues, it is often more preferable to connect both the resonator and the negative resistor to the ground. Therefore, parallel compensation is extensively used in integrated circuits.

3.3 Single-Transistor Negative Resistors

All single transistor negative resistors can be described with a simple three-port shown in Figure 3.4. When two of the ports are terminated with suitable impedances, a negative resistor is seen at the remaining port. The type of the transistor is of little consequence to the small-signal fundamentals. Due to limitations in the realizations of passive port impedances and in the active device biasing, not all possible variations are practically applicable, though.

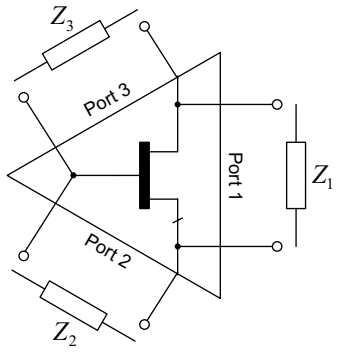

Figure 3.4 Basic structure of single-transistor negative resistors

3.3.1 Series-Mode Negative Resistances

For an RF signal, a series-mode single-transistor negative resistor looks like a series connection of reactance and negative resistance. This type is formed when Port 3 in Figure 3.4 is the input port. If the transistor is simply regarded as a voltage-controlled current source the small-signal equivalent circuit can be formed as shown in Figure 3.5:

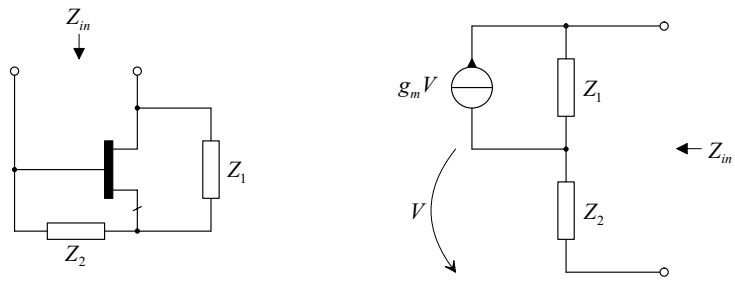

Figure 3.5 Series-mode negative resistance

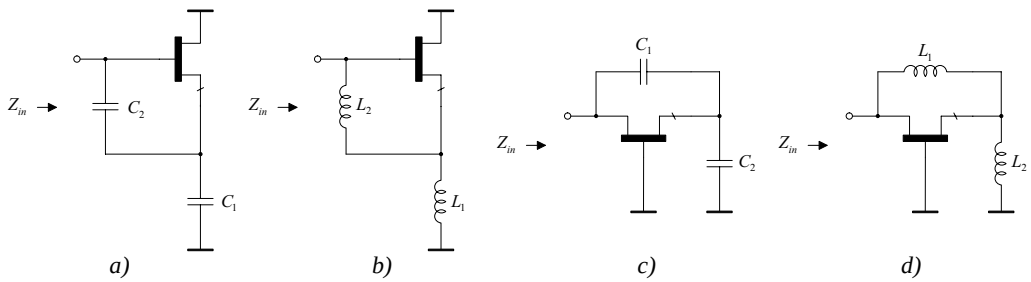

Figure 3.6 Possible transistor configurations for grounded negative resistors: a) Common-drain with capacitors [3.5] – [3.8]; b) Common-drain with inductors[3.9][3.10]; c) Common-gate with capacitors; d) Common-gate with inductors [3.11]

With one terminal grounded four different topologies can be found (Figure 3.6). The input impedance of the circuit becomes

$$Z_{in} = Z_1 + Z_2 + g_m Z_1 Z_2 \tag{3.3}$$

The real part of the input impedance is negative only if both Z_1 and Z_2 are of the same type, i.e. either inductive or capacitive. The corresponding passive equivalent circuits are shown in Figure 3.7. In practice, it is often more convenient to use capacitors as Z_1 and Z_2 since the gate-source (or base-emitter) capacitance of the transistor can be used as Z_2, or better, embedded into Z_2. On the other hand, biasing can be more easily arranged with an inductive Z_2.

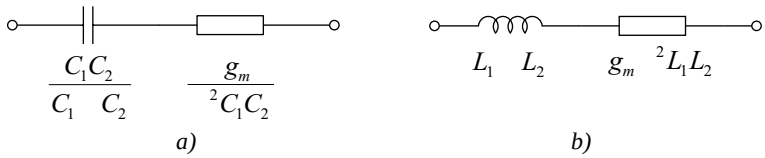

Figure 3.7 Equivalent circuits of the series-mode negative resistance: a) Z_1 and Z_2 capacitive; b) Z_1 and Z_2 inductive

Practical transistors have non-zero output conductances and other parasitic lossy elements that add positive resistance to the circuit. If inductors are used as feedback impedances, their limited quality factors have a similar effect. Together with the losses of the biasing components for the transistor, these factors cause deviation from the ideal case, and more negative resistance will be needed to compensate them.

Figure 3.8. shows some negative resistance values measured from a discrete BFR93A bipolar transistor in a capacitive common-collector connection (Figure 3.6a).

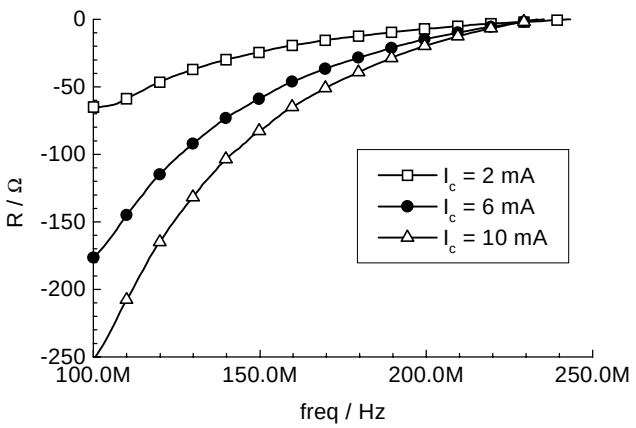

Figure 3.8 Measured negative resistance values from a common-collector BFR93A, C_1 = 100pF, C_2 = 10pF

Tuning

By definition, the value of negative resistance can be adjusted by changing the transistor bias (g_m) or by tuning either of the capacitors C_1 or C_2, e.g. by using varactors. If C_2 is omitted and C_{gs} is used as Z_2, tuning by g_m becomes ineffective since g_m and C_{gs} have a link through the constant transit frequency f_T of the transistor:

$$f_T = \frac{g_m}{2\pi C_{gs}} \quad \Rightarrow \quad R = \frac{-g_m}{\omega^2 C_1 C_{gs}} = \frac{-f_T}{2\pi f^2 C_1} \tag{3.4}$$

In this case, varactors remain the only option for tuning [3.5] – [3.7]. However, changing the varactor capacitance directly affects the equivalent series capacitance value and thus the center frequency of the resonator. This, together with the fact that high-quality varactors are difficult to realize in integrated circuits, makes this approach somewhat unattractive.

In the presence of C_2 (as in Figure 3.8), transconductance of the active device can be used for resistance tuning but again due to the g_m-C_{gs} link, the reactive part is changed to a lesser extent.

The negative resistance value can also be tuned by adding variable positive resistance e.g. in parallel with Z_1 [3.9][3.10]. While being a convenient method of tuning, the additional resistor injects excess noise into the circuit. In integrated circuits, a tunable resistor can be realized as a transistor operating in the triode region, but it may be difficult to achieve adequate resistance tuning range.

3.3.2 Parallel-Mode Negative Resistances

The other two single-transistor negative resistors are inherently parallel-mode circuits, i.e. their small-signal equivalent circuits are parallel connections.

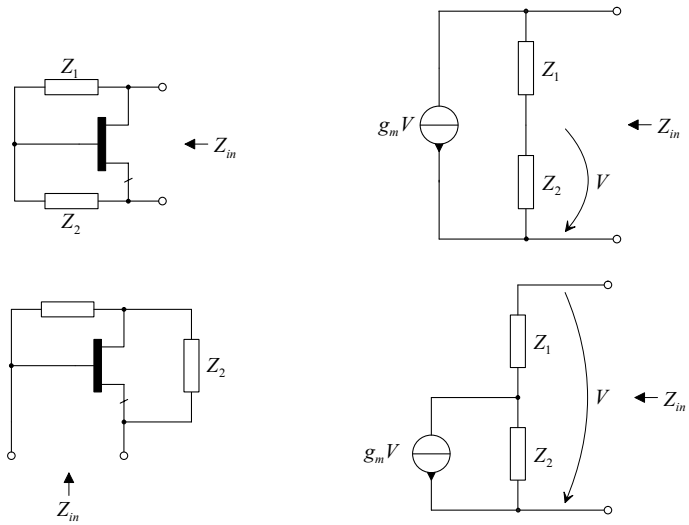

Figure 3.9 Parallel-mode negative resistor, types I and II

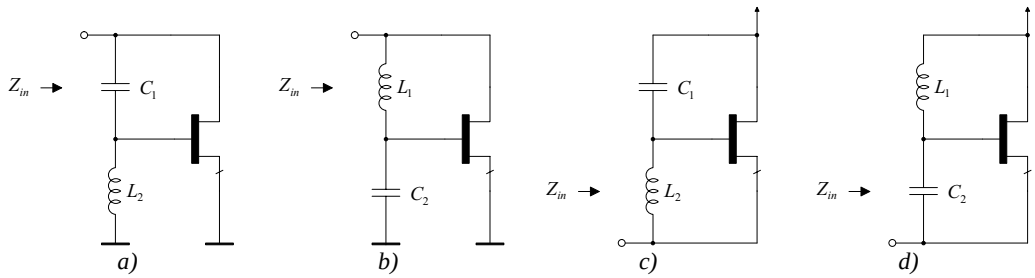

Figure 3.10 Transistor configurations for grounded negative resistors, type I: a) Common-source; b) Common-source, swapped; c) Common-drain; d) Common-drain, swapped [3.12][3.13]

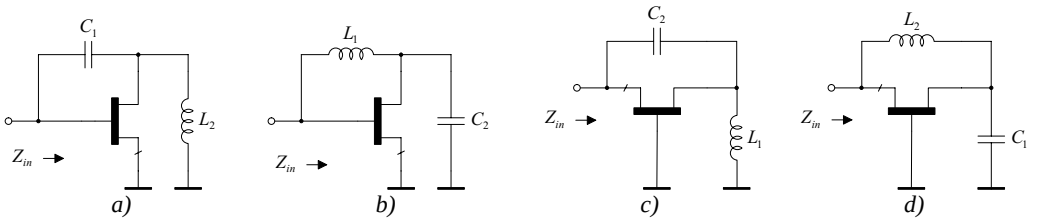

Figure 3.11 Transistor configurations for grounded negative resistors, type II: a) Common-source; b) Common-source, swapped; c) Common-gate; d) Common-gate, swapped

The input admittances become

$$Y_{in} = [Z_1 + Z_2]^{-1} + \left[\frac{1}{g_m}\left(1 + \frac{Z_1}{Z_2}\right)\right]^{-1} \tag{3.5}$$

Now the real part of the input admittance is negative only if Z_1 is capacitive and Z_2 inductive, or vice versa. The equivalent passive circuits are shown in Figure 3.12.

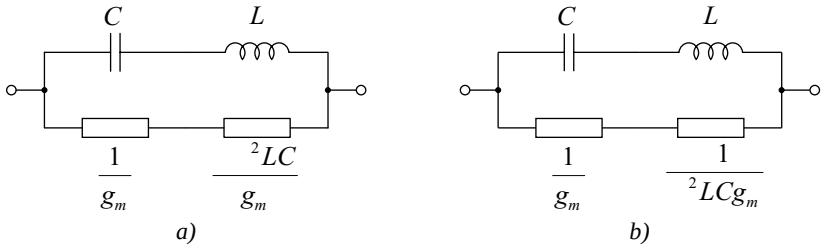

Figure 3.12 Equivalent circuits of the parallel-mode negative resistors a) Z_1 inductive, Z_2 capacitive, 'high-pass' ;b) Z_1 capacitive, Z_2 inductive, 'low-pass'

The value of effective resistance is a combination of two terms one of which is always positive. The sum becomes negative only when the operating frequency is higher ('high-pass') or lower ('low-pass') than the self-resonance frequency of the inductor-capacitor pair, i.e. $1/LC^{½}$, depending on the mutual position of the reactive elements. Again, it is more practical to have the capacitor in parallel with the gate-source capacitance of the transistor (e.g. Figure 3.10b), where it can even be omitted. In order to set the self-resonance frequency of L and C sufficiently much lower than the operating frequency, a relatively large inductor is required, especially if C is replaced with the small C_{gs}. This is a serious practical drawback of the 'high-pass' configuration, when looking at monolithic realizations. A large spiral inductor has a low self-resonance frequency, which sets the upper frequency limit of the negative resistor function.

Depending on its self-resonance frequency, the negative resistor looks either inductive or capacitive at the operating frequency. In a complete resonator the reactive element external to the negative resistor must be chosen compliantly: the external resonator component must always be of the same type as Z_2.

The topology in Figure 3.10b and Figure 3.11b were experimented with a BFR93A, and the measurement results are shown in Figure 3.13 and Figure 3.14.

Tuning

Like the series-mode circuits, a parallel-mode negative resistor can be tuned by changing the value of either C or g_m. Since the positive part is dependent only on the transconductance of the transistor and therefore variable, it is more functional to change the transistor bias for tuning

than in the series-mode circuits. This has also the benefit of leaving the self-resonance frequency untouched.

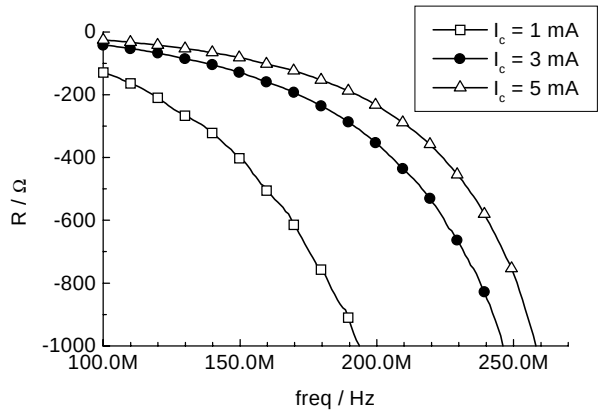

Figure 3.13 Measured negative resistance values from a common-emitter BFR93A, C = *100pF,* L = *100nH, inductor self-resonance at 280 MHz*

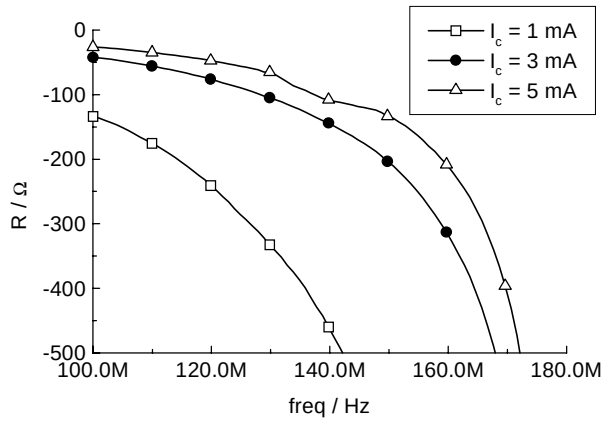

Figure 3.14 Measured negative resistance values from a common-base BFR93A, C = *100pF,* L = *100nH, inductor self-resonance at 180 MHz*

3.4 Twin-Transistor Negative Resistances

The fundamental difference between single- and twin-transistor negative resistances is the orientation of the transconductance element they involve. With two transistors it is possible to form a positive transconductance and, with suitable positive feedback, a negative resistor. As illustrated in Figure 3.15, a twin-transistor negative resistor is essentially a variation of the parallel-mode circuit (Figure 3.9) the only difference being the inversion of g_m.

Accordingly, the input admittance is

$$Y_{in} = \left[Z_1 + Z_2\right]^{-1} + \left[-\frac{1}{g_m}\left(1 + \frac{Z_1}{Z_2}\right)\right]^{-1} \tag{3.6}$$

Now the real part is negative if Z_1 and Z_2 are of the *same* type: capacitive, inductive or, although unfavorable in terms of noise, even purely resistive. The major benefit of positive transconductor negative resistances is the independence of the resistance value on frequency. Therefore, they have automatically wide operational bandwidths.

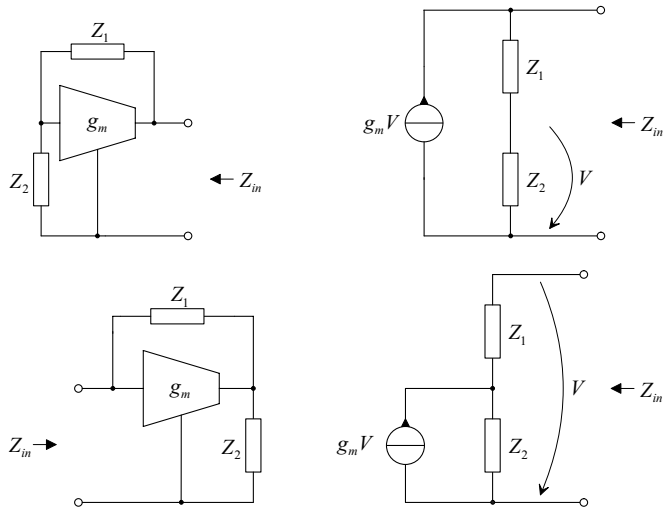

Figure 3.15 Twin-transistor negative resistor, types I and II

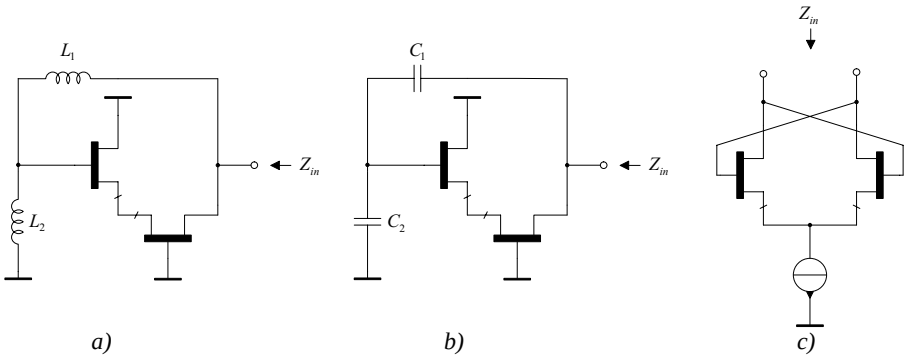

Figure 3.16 Transistor configurations for grounded negative resistors a) type I, inductive; b) type I capacitive [3.14][3.15]; c) type I differential

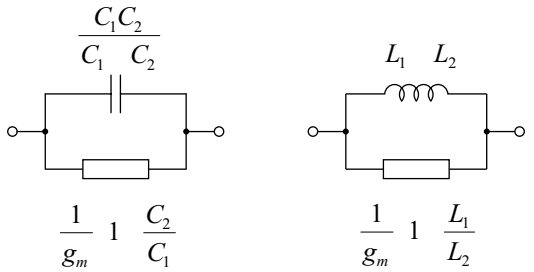

Figure 3.17 Equivalent circuits of the twin-transistor negative resistors; capacitive and inductive

The CD-CG transistor combination in Figure 3.16a,b functions as a positive transconductor with a compound g_m of $g_{m1}g_{m2} / (g_{m1} + g_{m2})$. If Z_1 is shorted ($Z_1 = 0$) and Z_2 is removed ($Z_2 = \infty$), the circuit reduces to a single negative resistor $-1/g_m$ (a positive transconductor with unity

feedback), and the well-known cross-coupled differential pair shown in Figure 3.16c is formed [3.14] – [3.20].

Tuning

Tuning of twin-transistors negative resistors is easily arranged by adjusting the current through the devices. When the transconductances of the transistors are changed, the input capacitances are also affected. This results in a slight frequency dependence of the circuit.

3.5 Noise in Negative Resistors

3.5.1 Relative Noise Resistance and Conductance

In terms of noise, active negative resistors can be regarded as passive resistors whose noise voltage and current spectral densities are

$$\begin{aligned} \hat{v}_n^2 &= 4kTr_n|R| \\ \hat{i}_n^2 &= 4kTg_n|G| \end{aligned} \tag{3.7}$$

where R and G are the negative resistance and conductance values. The coefficients r_n and g_n are so-called relative noise resistance and conductance, respectively. They give a figure of how much more or less the active negative resistor produces noise than a passive (positive) resistor of the same size. This concept provides a convenient way of comparing noise properties of different negative resistor topologies.

In series-mode circuits, i.e. where the resistor is in series with the rest of the resonator, large series resistances produce high noise voltage levels across the unloaded input nodes. On the other hand, in parallel-mode circuits large parallel *conductances* produce high short-circuit noise currents and consequently high noise voltage levels across the parallel circuit. Therefore, it is practical to use relative noise resistances and noise voltage analyses for describing series-mode negative resistances, whereas relative noise conductances and noise currents should be used for parallel-mode negative resistors.

In negative resistors, the noise source usually appears to be associated with a reactive element, mathematically regarded as a noisy capacitance or inductance. For this reason, r_n and g_n are frequency-dependent in contrast to passive resistors.

3.5.2 Transistor Noise Model

Essentially three noise mechanisms can be observed in semiconductor components [3.21]. In each semiconductor ohmic resistivity gives rise to thermal noise generation. When current flows through a semiconductor junction, shot noise always occurs due to the fluctuation in the number of charge carriers in any time interval. Inversely proportional to frequency, flicker or 1/f noise, caused by slow time-constant electron trapping, has a dominant effect at low frequencies.

The collector shot noise can be regarded as the main noise source in bipolar transistors in hand calculations. It is formulated as a current source between the collector and the emitter:

$$\hat{i}_c^2 = 2qI_c \tag{3.8}$$

Although omitted here, other noise sources in a bipolar transistor would be the thermal noise in collector, emitter and base resistances, and the base shot noise. When operating at high frequencies the 1/f noise can be neglected as long as circuits are considered linear.

Remembering that

$$I_c = g_m V_T = g_m \frac{kT}{q} \tag{3.9}$$

The collector shot noise can be written in a form that resembles thermal noise:

$$\hat{i}_c^2 = 2kTg_m \tag{3.10}$$

In field-effect transistors (junction FETs, MOSFETs, MESFETs and HEMTs) the dominating noise source is the thermal noise in the channel which is represented by a noise current source:

$$\hat{i}_d^2 = \frac{8}{3}kTg_m \tag{3.11}$$

Now, it is easy to see that in a simplified case noise in all transistor types can be accounted for with a single current source in parallel with the transconductance g_m. Its value becomes

$$\hat{i}_n^2 = 4kT\gamma g_m \tag{3.12}$$

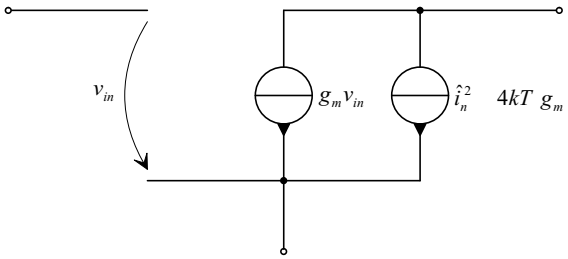

Figure 3.18 Simplified transistor noise model

The factor γ is called the noise gamma coefficient, and its value is 1/2 for bipolar transistors and 2/3 for FETs. However, in short-channel MOSFET devices it can be much larger. Although much simplified, Equation (3.12) gives a convenient way of describing noise of a single transistor transconductor, and it will be used hereafter in calculations.

3.5.3 Noise in Twin-Transistor Transconductors

A twin-transistor compound connection is needed for realizing the positive transconductor in inverted-g_m parallel-mode negative resistors. Both transistors induce mutually uncorrelated noise, but if they are identical the output noise corresponds to that of a single half-sized transistor only. The individual transistors in a compound transconductor are sized as $2g_m$ in order to get a combined transconductance of g_m, and therefore the noise properties are identical to single-transistor transconductors.

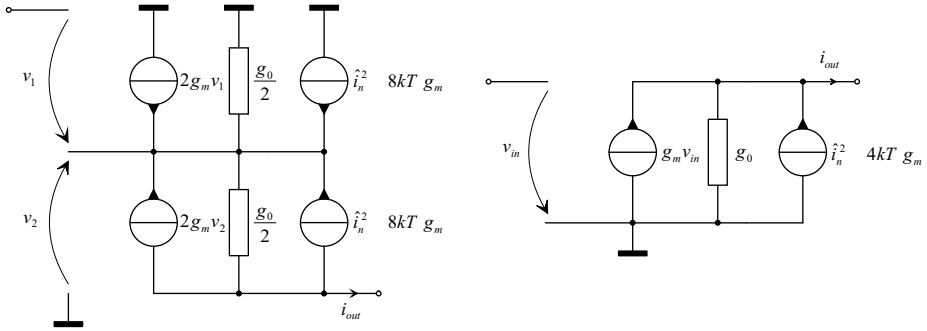

Figure 3.19 Noise in twin-transistor, positive-g_m transconductors, and the single-transistor equivalent

3.5.4 Noise in Series-Mode Negative Resistors

The equivalent circuit of the series-mode negative resistor with the noise source is shown in Figure 3.20.

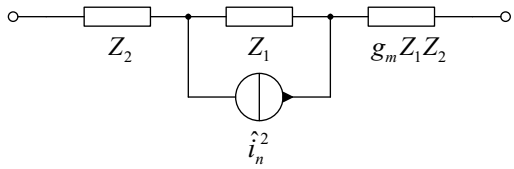

Figure 3.20 Equivalent circuit of a series-mode negative resistor with the transistor noise source

The relative noise resistance r_n can easily be defined for the circuit:

$$r_n = \gamma Z_1 / Z_2 \tag{3.13}$$

Obviously, noise can be minimized by minimizing the reactance Z_1 and maximizing Z_2, but keeping their product constant for unchanged negative resistance. A very important remark can be made from Eq. (3.13): *an active negative resistor can be – with a proper selection of the reactance ratio – less noisy than its passive counterpart ($r_n < 1$)!* This is one of the fundamental reasons why negative resistance resonators are superior to other active resonator types in terms of noise. This also implies that noise characteristics, i.e. losses, of the actual passive LC resonator components may have greater effect on the overall noise performance than the loss-compensating active circuit.

When a negative resistor is used as a part of a resonance circuit, its reactive components form conveniently either the capacitor or the inductor of the resonator. However, in reality these components are not ideal. Their losses directly contribute to the total noise of the resonator, as stated previously, and slightly change the transistor noise transfer characteristics. Those reactive components that have the lowest Q values should be chosen for the feedback components of the negative resistor. As the resonator capacitors are often realized as low-Q varactors, and integrated spiral inductors also have Q values of the same magnitude, the difference is not necessarily large, though.

3.5.5 Noise in Parallel-Mode Negative Resistors

The noise equivalent circuits of both parallel-mode negative resistors are shown in Figure 3.21.

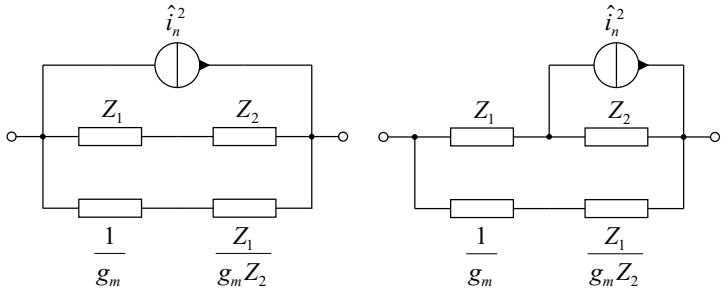

Figure 3.21 Equivalent circuits of a parallel-mode negative resistors with the transistor noise source

In parallel circuits, the relative noise conductance is used as a measure of noise performance. In the case of the type I, the noise source corresponds directly to the output noise current, and we get

$$g_n = \gamma\left|1 + {Z_1}/{Z_2}\right| = \gamma\left(w^2 - 1\right), \quad w = {\omega}/{\omega_{sr}} \tag{3.14}$$

for a 'high-pass' negative resistor where Z_1 is inductive and Z_2 capacitive and ω_{sr} is their mutual resonating frequency. The relative noise conductance rises with increasing frequency and the best results are obtained near the self-resonance of the LC pair.

The type II of parallel-mode circuits is more suitable for low-noise applications, as its relative noise conductance becomes

$$g_n = \frac{\gamma}{\left|1 + {Z_1}/{Z_2}\right|} = \frac{\gamma}{w^2 - 1} \tag{3.15}$$

Noise diminishes rapidly with increasing frequency, and potentially very low-noise parallel-mode negative resistors can be synthesized in this way.

To further enhance noise performance in parallel-mode circuits, it is important to minimize the number of noise-inducing components in the whole design. As one always needs three reactive components for a complete resonator, of which at least one is a noisy inductor and one is a noisy external tuning varactor, the third component should be noiseless: a passive capacitor. This implies that the negative resistor itself should look inductive at the operating frequency, i.e. the self-resonance frequency of L and C should be lower than the operating frequency ('high-pass' types). In this case, the negative resistor would not induce any additional noise except for the transistor noise.

3.5.6 Noise in Inverted-g_m Parallel-Mode Negative Resistors

Noise inducing mechanisms are the same in single- and twin-transistor parallel-mode negative resistances, but since no resonance is present the relative noise conductances are frequency-independent:

$$\begin{aligned} &\text{I}: \quad g_n = \gamma\left(1 + {C_2}/{C_1}\right) \quad \text{or} \quad g_n = \gamma\left(1 + {L_1}/{L_2}\right) \\ &\text{II}: \quad g_n = \frac{\gamma}{\left(1 + {C_2}/{C_1}\right)} \quad \text{or} \quad g_n = \frac{\gamma}{\left(1 + {L_1}/{L_2}\right)} \end{aligned} \tag{3.16}$$

According to Section 3.5.3, when a twin-transistor transconductor forms the non-inverting transconductor, the noise performance remains unchanged.

3.5.7 Measuring Relative Noise Resistances and Conductances

The equivalent noise resistance can be defined when the negative resistor is realized as a two-port and its noise figure F and y-parameters have been measured, using the following relation (R_0 is the characteristic resistance of the measuring system):

$$r_n = \frac{R_0}{|R|}(F-1) \tag{3.17}$$

Results from a BFR93A with two different capacitance ratios are plotted in Figure 3.22. With the larger C_2/C_1 ratio the circuit is indeed less noisy than its passive counterpart at most frequencies, even though the behavior of the real circuit is more complicated and the device noise larger than in theoretical estimations. The theoretical ratio of the relative noise resistance curves is 25 and the measured ratio is about 22. Hence, the relative accuracy of the theoretical model is fairly good.

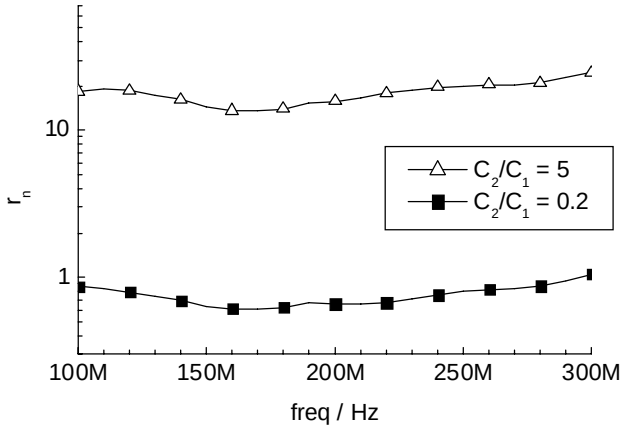

Figure 3.22 Measured relative noise resistance from a common-collector BFR93A, I_c = 5 mA

From the measured parameters the relative noise conductance of a parallel-mode negative resistor can be de-embedded as

$$g_n = \frac{G_0}{|G|}(F-1)\left|\frac{y_{21}}{y_{11}+y_{21}+G_s}\right|^2 \tag{3.18}$$

The relative noise conductances of the measured parallel-mode circuits are plotted in Figure 3.23. The results confirm the estimated behavior with the exception of the rising slope of the common-base (type II) circuit from 165 MHz on. This is due to the self-resonance of the non-ideal inductor at 250 MHz, which brings up its own peaking noise. At low frequencies the type I has lower noise as predicted by the theoretical model. The crossing frequency should be $2^{½}f_{sr}$, but in the measured circuit ($f_{sr} \approx 50$ MHz) it is much higher. Nevertheless, the type II of the parallel-mode negative resistors is clearly best in terms of noise performance at higher frequencies where also the negative resistance value is in a practicable range.

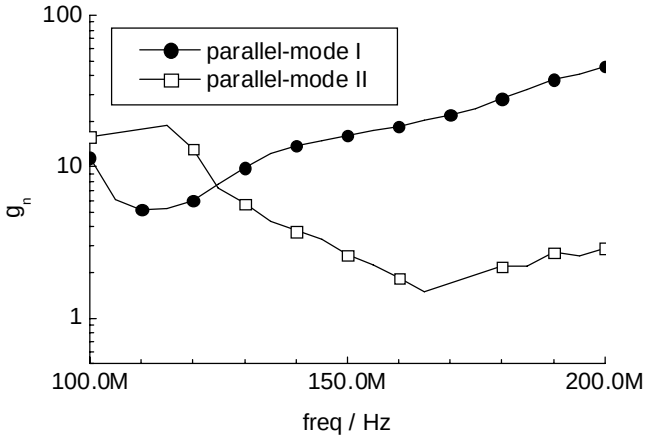

Figure 3.23 Measured relative noise conductance from a common-emitter and common-base BFR93A, I_c = 5 mA, L = 56 nH, C = 91 pF

3.6 Distortion in Negative Resistors

3.6.1 Introduction

The negative resistors discussed in this thesis are active circuits including one or more transistors. As transistors are always non-linear in the real world, the negative resistors are also unavoidably non-linear and distort the incoming signal. This will have effect on the performance of the whole resonator. In this chapter, distortion in negative resistors is analyzed on a detailed level.

A non-linear negative resistor can be described with a conductance function *g(v)* where the AC voltage across the resistor is the stimulus and the AC current through the resistor is the response: $i_{in} = g(v_{in})$. The choice of using voltage as the stimulus can be justified, if the resonator components are to be connected in parallel with the negative resistor, therefore sharing the same voltage excitation. The contribution of each resonator component can then be examined separately as current responses. The type of the non-linear function *g(v)* depends on the source of non-linearity, i.e. the transistor(s). Bipolar transistors create exponential resistance functions and field-effect transistors typically polynomial functions. The mechanism of how the non-linear behavior of the transistor affects the whole circuit is defined by the surrounding passive circuitry. Therefore, with a proper selection of impedances within a negative resistor, overall distortion can potentially be minimized.

In non-linear resistors, the concept of AC resistance is somewhat ambiguous. At very low input currents the conductance function is practically linear and the conductance value is given by the derivative $g = \partial g(v_{in})/\partial v_{in}$ at zero (or simply by the division $g = g(v_{in})/v_{in}$). When the input voltage swing is increased, the current through the resistor gradually gets compressed because a part of the response current is shifted into higher harmonic frequencies. The fundamental frequency response cannot directly be seen from the original non-linear function any more, and we must perform a harmonic analysis in order to obtain it. Having done that we can define the large-signal conductance

$$g = \frac{\mathrm{Re}\{\textit{fundamental response current}\}}{\textit{stimulus voltage } v_{in}} \tag{3.19}$$

which is a polynomial function of the input voltage. The large-signal input conductance is also called the real part of *the describing function* of the circuit. Figure 3.24 shows an exemplary non-linear fundamental response resistance curve:

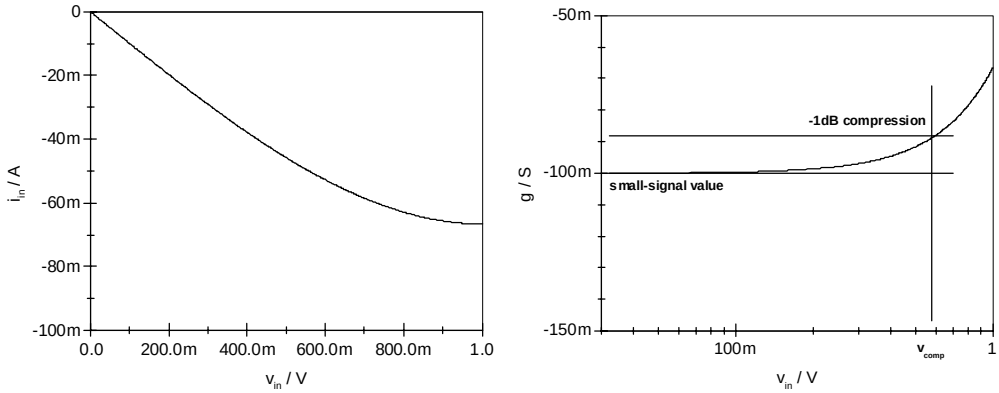

Figure 3.24 Voltage-current and conductance curves of a non-linear negative resistor

A practical measure of non-linearity is the -1-dB compression point of the negative conductance. It is the input voltage amplitude making the fundamental frequency response drop 1 dB or 10.9%. The drop of the negative conductance will show directly in quality factor degradation, when the negative resistor is a part of a parallel resonator. It also provides a good method of comparing different negative resistor topologies in terms of distortion performance.

3.6.2 Volterra Technique

The Volterra series technique is commonly used for hand calculations of harmonic responses. Due to its rapidly increasing complexity in large circuits with several non-linearities, the Volterra technique is practical only for very simplified cases. Therefore, the result is always a rough approximation of the real situation, and for more accurate analysis numerical simulation methods, such as the harmonic balance technique, must be used. Nevertheless, the Volterra method can give an insight into how the dimensioning of the electronic circuit should be done for optimal performance.

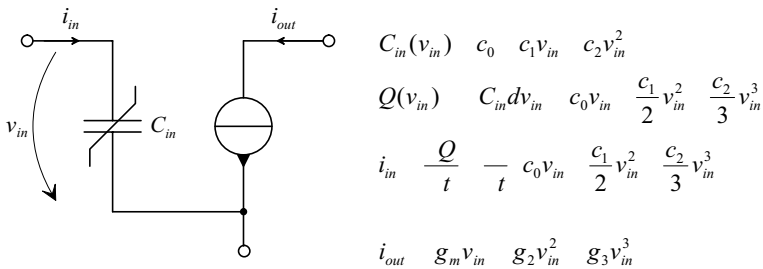

Figure 3.25 Simple non-linear model of a transistor

The prerequisite for the Volterra analysis is that the circuit under examination is weakly non-linear around the quiescent point. The circuit is weakly non-linear, or quasi-linear, if its non-linear behavior can be accurately described by the first three terms of its Volterra series

Order	Frequency of response	Response	Type of response
1	ω_1	$A_1H_1(j\omega_1)$	linear
1	ω_2	$A_2H_1(j\omega_2)$	
2	$\omega_1+\omega_2$	$A_1A_2H_2(j\omega_1, j\omega_2)$	second-order intermodulation
2	$\lvert\omega_1-\omega_2\rvert$	$A_1A_2H_2(j\omega_1,-j\omega_2)$	
2	$2\omega_1$	$\frac{1}{2}A_1^2H_2(j\omega_1, j\omega_1)$	second harmonics
2	$2\omega_2$	$\frac{1}{2}A_2^2H_2(j\omega_2, j\omega_2)$	
2	0	$\frac{1}{2}A_1^2H_2(j\omega_1,-j\omega_1)$	DC shift
2	0	$\frac{1}{2}A_2^2H_2(j\omega_2,-j\omega_2)$	
3	$2\omega_1+\omega_2$	$\frac{3}{4}A_1^2A_2H_3(j\omega_1, j\omega_1, j\omega_2)$	third-order intermodulation
3	$\lvert2\omega_1-\omega_2\rvert$	$\frac{3}{4}A_1^2A_2H_3(j\omega_1, j\omega_1,-j\omega_2)$	
3	$\omega_1+2\omega_2$	$\frac{3}{4}A_1A_2^2H_3(j\omega_1, j\omega_2, j\omega_2)$	
3	$\lvert\omega_1-2\omega_2\rvert$	$\frac{3}{4}A_1A_2^2H_3(j\omega_1,-j\omega_2,-j\omega_2)$	
3	ω_1	$\frac{3}{2}A_1A_2^2H_3(j\omega_1, j\omega_2,-j\omega_2)$	third-order desensitization
3	ω_2	$\frac{3}{2}A_1^2A_2H_3(j\omega_1,-j\omega_1, j\omega_2)$	
3	ω_1	$\frac{3}{4}A_1^3H_3(j\omega_1, j\omega_1,-j\omega_1)$	third-order compression or expansion
3	ω_2	$\frac{3}{4}A_2^3H_3(j\omega_2, j\omega_2,-j\omega_2)$	
3	$3\omega_1$	$\frac{1}{4}A_1^3H_3(j\omega_1, j\omega_1, j\omega_1)$	third harmonics
3	$3\omega_2$	$\frac{1}{4}A_2^3H_3(j\omega_2, j\omega_2, j\omega_2)$	

Table 3.1 Different responses at the output of a non-linear system described by Volterra kernels of order 1,2 and 3, excited by two sinusoids $A_1\cos\omega_1 t$ and $A_2\cos\omega_2 t$ [3.22]

[3.22]. This is also the point beyond which the calculations become overly complicated. Thus, we must assume that the non-linearities in the circuit, i.e. in the transistors, can be expressed accurately enough with a three-term power series. In a generic (field-effect) transistor, the two dominant non-linear components are the input capacitance and the transconductance (Figure 3.25).

The strength of the Volterra series lies in its capability to handle both static and dynamic non-linearities. The ordinary Taylor series can be used only for describing static memoryless non-linearities (resistances or transconductances), but for non-linear reactive components (capacitors or inductors) it is useless. However, the non-linear transistor input capacitor brings excessive complexity to the expressions, and therefore only the static transconductor will represent the transistor non-linearity hereafter. Even after this simplification, the effect of auxiliary circuitry will be clearly visible. Strictly speaking, without dynamic non-linearities, the Volterra and Taylor expansions become the same, and the Volterra analysis techniques would not necessarily have to be utilized. It is, however, convenient to use the straightforward mechanical calculation methods developed for the Volterra analysis even in this case.

In the following calculations the method of non-linear current sources will be utilized [3.22][3.23]. It is a fairly simple but elaborate way of determining the harmonic components of a non-linear circuit. The results of the calculations are the Volterra kernels of order one, two and three: $H_1(j\omega)$, $H_2(j\omega_1,j\omega_2)$, $H_3(j\omega_1,j\omega_2,j\omega_3)$. From the Volterra kernels, the corresponding harmonic components can be defined as shown in Table 3.1.

3.6.3 Non-Linear Behavior of the Series-Mode Negative Resistor

First we shall look into the series-mode negative resistor described in Section 3.3.1 and calculate its Volterra kernels. The non-linear model for the circuit is shown in Figure 3.26.

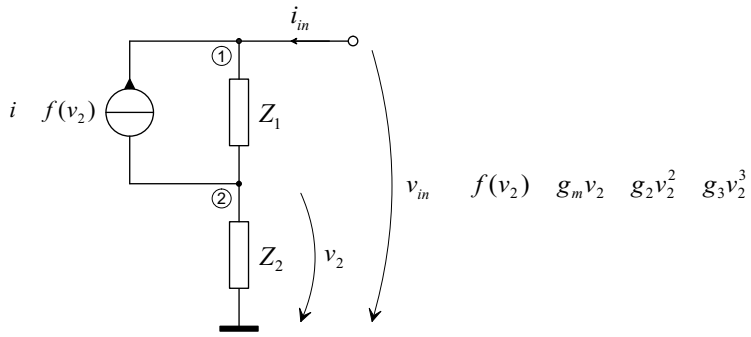

Figure 3.26 Simplified non-linear model for the series-mode negative resistor

First-order kernels

The first-order Volterra kernels are nothing but the transfer functions of the linearized circuit when the excitation voltage equals one. For the circuit in Figure 3.26 we can write the Kirchoff current equation for the node 2:

$$\big(1 - H_{1,2}(j\omega)\big)Y_1 = H_{1,2}(j\omega)\big(g_m + Y_2\big) \tag{3.20}$$

Solving Eq. (3.20) gives the first-order Volterra kernel for node 2:

$$H_{1,2}(j\omega) = \frac{Y_1}{g_m + Y_1 + Y_2} \tag{3.21}$$

Correspondingly, the first-order input current kernel becomes

$$H_{iin,1} = Y_2 H_{1,2}(j\omega) = \frac{Y_1 Y_2}{g_m + Y_1 + Y_2} = \frac{1}{Z_1 + Z_2 + Z_1 Z_2 g_m} \tag{3.22}$$

Second-order kernels

For calculating the second-order Volterra kernels, a non-linear current source must be placed in parallel with each non-linearity. The expressions of the second-order non-linear current sources are tabulated in Table 3.2, and the negative resistance circuit with the additional non-linear current sources is illustrated in Figure 3.27. For higher-order kernel calculations, the input voltage excitation is zeroed. The second-order Volterra kernels can now be solved in the similar way than the first-order kernels:

$$\begin{aligned}
&\big(0 - H_{2,2}(j\omega_1, j\omega_2)\big)Y_1(j\omega_1 + j\omega_2) = H_{2,2}(j\omega_1, j\omega_2)\big(g_m + Y_2(j\omega_1 + j\omega_2)\big) + i_{NL2} \\
&\Rightarrow \quad H_{2,2}(j\omega_1, j\omega_2) = \frac{-i_{NL2}}{g_m + Y_1(j\omega_1 + j\omega_2) + Y_2(j\omega_1 + j\omega_2)} \\
&\Rightarrow \quad H_{iin,2} = \frac{-i_{NL2} Y_2(j\omega_1 + j\omega_2)}{g_m + Y_1(j\omega_1 + j\omega_2) + Y_2(j\omega_1 + j\omega_2)}
\end{aligned} \tag{3.23}$$

From Table 3.2 we get the expression for the non-linear current source:

Type of basic non-linearity	Expression for second-order non-linear current source
(trans)conductance	$g_2 H_{1,k}(j\omega_1) H_{1,k}(j\omega_2)$
capacitance	$(j\omega_1 + j\omega_2) c_2 H_{1,k}(j\omega_1) H_{1,k}(j\omega_2)$

Table 3.2 Non-linear second-order current sources for the different basic non-linearities [3.22]

Type of basic non-linearity	Expression for third-order non-linear current source
(trans)conductance	$g_3 H_{1,k}(j\omega_1) H_{1,k}(j\omega_2) H_{1,k}(j\omega_3) + \frac{2}{3} g_2 \overline{H_{2,k}(j\omega, j\omega) H_{1,k}(j\omega)}$
capacitance	$(j\omega_1 + j\omega_2 + j\omega_3)\left[c_3 H_{1,k}(j\omega_1) H_{1,k}(j\omega_2) H_{1,k}(j\omega_3) + \frac{2}{3} c_2 \overline{H_{2,k}(j\omega, j\omega) H_{1,k}(j\omega)}\right]$
$\overline{H_{2,k}(j\omega, j\omega) H_{1,k}(j\omega)} =$ $H_{2,k}(j\omega_1, j\omega_2) H_{1,k}(j\omega_3) + H_{2,k}(j\omega_2, j\omega_3) H_{1,k}(j\omega_1) + H_{2,k}(j\omega_1, j\omega_3) H_{1,k}(j\omega_2)$	

Table 3.3 Non-linear third-order current sources for the different basic non-linearities [3.22]

$$\begin{aligned} i_{NL2} &= g_2 H_{1,2}(j\omega_1) H_{1,2}(j\omega_2) \\ &= g_2 \left(\frac{Y_1(j\omega_1)}{g_m + Y_1(j\omega_1) + Y_2(j\omega_1)} \right) \left(\frac{Y_1(j\omega_2)}{g_m + Y_1(j\omega_2) + Y_2(j\omega_2)} \right) \end{aligned} \tag{3.24}$$

It is easier to use the actual admittance expressions for Y_1 and Y_2 from now on. In the following calculations, they are treated as capacitors C_1 and C_2. The dual expressions can be used for inductors, respectively. Now, the second-order Volterra kernels become

$$H_{2,2}(j\omega_1, j\omega_2) = \frac{g_2 \omega_1 \omega_2 C_1^2}{(g_m + (j\omega_1 + j\omega_2)(C_1 + C_2))(g_m + j\omega_1(C_1 + C_2))(g_m + j\omega_2(C_1 + C_2))} \tag{3.25}$$

$$H_{iin,2}(j\omega_1, j\omega_2) = \frac{g_2 \omega_1 \omega_2 C_1^2 (j\omega_1 + j\omega_2) C_2}{(g_m + (j\omega_1 + j\omega_2)(C_1 + C_2))(g_m + j\omega_1(C_1 + C_2))(g_m + j\omega_2(C_1 + C_2))}$$

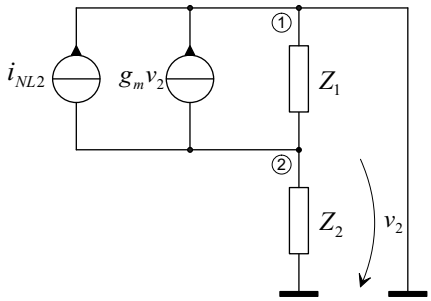

Figure 3.27 Second-order non-linear current source in the series-mode negative resistor

Third-order kernels

The third-order Volterra kernels can be calculated in a similar manner as the second-order ones, and the expressions for the corresponding non-linear current sources can be found in Table 3.3.

$$H_{iin,3} = \frac{-i_{NL3} Y_2(j\omega_1 + j\omega_2 + j\omega_3)}{g_m + Y_1(j\omega_1 + j\omega_2 + j\omega_3) + Y_2(j\omega_1 + j\omega_2 + j\omega_3)} \tag{3.26}$$

Type of response	Expression for third-order non-linear current source
third harmonic	$g_3 H_{1,2}^3(j\omega) + 2g_2 H_{2,2}(j\omega, j\omega) H_{1,2}(j\omega)$
third-order intermodulation $\lvert 2\omega_1 - \omega_2 \rvert$	$g_3 H_{1,2}^2(j\omega_1) H_{1,2}(-j\omega_2)$ $+ \frac{2}{3} g_2 \left[2H_{2,2}(j\omega_1, j\omega_1) H_{1,2}(-j\omega_2) + H_{2,2}(j\omega_1, -j\omega_2) H_{1,2}(j\omega_1) \right]$
compression or expansion	$g_3 H_{1,2}^2(j\omega) H_{1,2}(-j\omega)$ $+ \frac{2}{3} g_2 \left[2H_{2,2}(j\omega, j\omega) H_{1,2}(-j\omega) + H_{2,2}(j\omega, -j\omega) H_{1,2}(j\omega) \right]$

Table 3.4 Third-order non-linear current sources for the different types of responses

To facilitate the calculations the non-linear current source expressions can be derived separately for each harmonic component of interest. By using Table 3.1 and Table 3.3 as references, they are tabulated in Table 3.4. Thus, for the series-mode negative resistor we get

$$
\begin{aligned}
i_{NL3,HD3} &= \frac{-j\omega^3 C_1^3}{(g_m + j\omega(C_1 + C_2))^3} \left(g_3 - \frac{2g_2^2}{g_m + 2j\omega(C_1 + C_2)} \right) \\
i_{NL3,COMP} &= \frac{j\omega^3 C_1^3}{\left(g_m^2 + \omega^2 (C_1 + C_2)^2\right)(g_m + j\omega(C_1 + C_2))} \left(g_3 - \frac{2g_2^2}{3} \left(\frac{1}{g_m + 2j\omega(C_1 + C_2)} + \frac{2}{g_m} \right) \right)
\end{aligned}
\tag{3.27}
$$

and further

$$
\begin{aligned}
H_{iin,HD3} &= \frac{-3\omega^4 C_1^3 C_2}{(g_m + j\omega(C_1 + C_2))^3} \left(g_3 - \frac{2g_2^2}{g_m + 2j\omega(C_1 + C_2)} \right) \\
H_{iin,COMP} &= \frac{\omega^4 C_1^3 C_2}{\left(g_m^2 + \omega^2 (C_1 + C_2)^2\right)(g_m + j\omega(C_1 + C_2))} \left(g_3 - \frac{2g_2^2}{3} \left(\frac{1}{g_m + 2j\omega(C_1 + C_2)} + \frac{2}{g_m} \right) \right)
\end{aligned}
\tag{3.28}
$$

The third-order intermodulation products can be defined in the same way. When negative resistors are used in narrow-band filters, the two excitation frequencies must be very near each other in order to ensure that the IM products are at the pass-band as well. It is therefore reasonable to approximate that the third-order IM response magnitude is identical with the compression response ($\omega_1 \approx \omega_2$) if the two excitation voltages have the same magnitude.

Distortion components

After having calculated the appropriate Volterra kernels we can finally identify each harmonic component in question. With the aid of Table 3.1, they can be written as shown in Table 3.5. The complexity of the expressions arises from the fact that series-mode negative resistances should be excited by current, not voltage, and connected in series with the actual (series) resonator. The practical filters discussed here employ, however, parallel resonators with voltage excitation, and hence also series-mode negative resistances must be treated as parallel negative conductances. It is also very difficult to realize sufficiently small negative resistance values for series compensation in practice.

The theory shows that by dimensioning the circuit parameters suitably, the third-order compression kernel will cross zero and become negative. Instead of compression, expansion will take place in that case, and problems may occur in the form of instability at high signal levels. By ensuring that $g_m^2 << \omega^2 (C_1 + C_2)^2$ this problem is circumvented.

The results in Table 3.5 show that the shunt capacitance C_1 at the transistor output has the greatest impact on distortion, and so it should be minimized. However, this is in contradiction with the requirement for lowest noise, if the value of C_2 is respectively increased for

Type of response	Response i_{in}, capacitive Z_1 Z_2
fundamental	$v_{in} \Big/ \left(\frac{1}{j\omega C_1} + \frac{1}{j\omega C_2} - \frac{g_m}{\omega^2 C_1 C_2} \right)$
second harmonic	$v_{in}^2 \frac{g_2 j\omega^3 C_1^2 C_2}{(g_m + j\omega(C_1+C_2))^2 (g_m + 2j\omega(C_1+C_2))}$
third harmonic	$-\frac{3v_{in}^3}{4} \frac{\omega^4 C_1^3 C_2}{(g_m + j\omega(C_1+C_2))^3 (g_m + 3j\omega(C_1+C_2))} \left(g_3 - \frac{2g_2^2}{g_m + 2j\omega(C_1+C_2)} \right)$
compression ($g_3 < 0$)	$\frac{3v_{in}^3}{4} \frac{\omega^4 C_1^3 C_2}{(g_m + j\omega(C_1+C_2))^2 (g_m^2 + \omega^2(C_1+C_2)^2)} \left(g_3 - \frac{2g_2^2}{3} \left(\frac{1}{g_m + 2j\omega(C_1+C_2)} + \frac{2}{g_m} \right) \right)$

Table 3.5 Harmonic distortion components for the series-mode negative resistor with capacitors

maintaining the desired negative resistance value [Section 3.5.4]. A trade-off between lowest noise and lowest distortion exists.

The -1-dB conductance compression for the series-mode negative resistor takes place, as explained in Section 3.6.1, when

$$\frac{\mathrm{Re}\{i_{in}(\text{compression})\}}{\mathrm{Re}\{i_{in}(\text{fundamental})\}} = 10.9\% \tag{3.29}$$

Using the expressions from Table 3.5, we can write

$$\begin{aligned} &\frac{3}{4} v_{in,comp}^2 K_C \frac{\omega^2 C_1^2}{g_m \left(g_m^2 + \omega^2 (C_1+C_2)^2 \right)^2} = 10.9\% \\ &K_C = \mathrm{Re}\left\{ (g_m - j\omega(C_1+C_2))^2 \left(g_3 - \frac{2g_2^2}{3} \left(\frac{1}{g_m + 2j\omega(C_1+C_2)} + \frac{2}{g_m} \right) \right) \right\} \end{aligned} \tag{3.30}$$

The theoretical -1-dB conductance compression voltage is then

$$v_{in,comp}^2 = \frac{0.145}{K_C} \frac{g_m \left(g_m^2 + \omega^2 (C_1+C_2)^2 \right)^2}{\omega^2 C_1^2} \tag{3.31}$$

Measured results

The theoretical estimations were verified by measuring the s-parameters of a BFR93A-based series-mode negative resistor as a function of the input power. The circuit is the same as in Figure 3.22. with the same bias point. To convert the 50Ω-referenced output power from the analyzer into the peak voltage across the circuit the following transformation was used:

$$v_{in} = \sqrt{400 P_{in}} \left| \frac{Z_{in}}{Z_{in} + 100} \right| \tag{3.32}$$

As seen from Figure 3.28 the circuit with a high C_1 and a low C_2 has a clearly lower compression point than the other, which is in good agreement with the theory in qualitative terms. Due to the limited power sweeping capability of the s-parameter analyzer, the -1-dB or 10.9% resistance compression points could not be reached in measurements. The 2%-compression points are 24 mV and 93 mV, respectively.

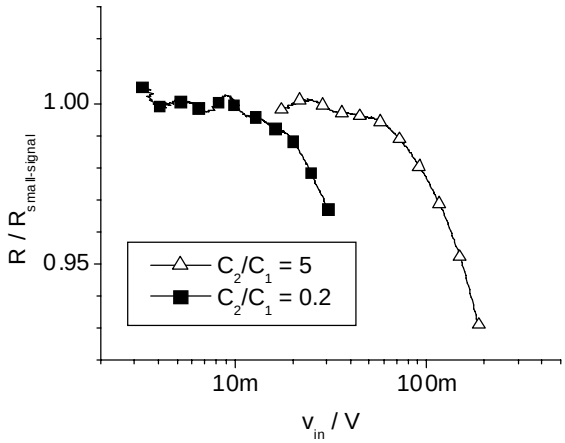

Figure 3.28 Measured resistance compression from a common-collector BFR93A, I_c = 5 mA, f = 150 MHz

3.6.4 Non-Linear Behavior of the Parallel-Mode Negative Resistors

By using the same calculation procedure as in the previous chapter, we can define the Volterra kernels and consequently the harmonic components of the parallel-mode negative resistors [Section 3.3.2]. The expressions are much simpler as voltage excitation is well suited for parallel-mode circuits. The results are summarized in Table 3.6 for the types I and II. Only the 'high-pass' configurations, i.e. inductive Z_1 and capacitive Z_2, are discussed; the dual 'low-pass' expressions can be obtained from these easily.

It seems that the type I suffers from greater distortion than the type II at frequencies near the self-resonance frequency ω_{sr}, but vice versa if the operating frequency is sufficiently large. For the type I, there is a contradiction between low-noise and low-distortion requirements, but interestingly this does not apply to the type II. [Section 3.5.5].

The -1-dB conductance compression points can be defined in the same manner as previously:

$$\begin{aligned} v_{in,comp}^2 &= 0.145\frac{g_m}{g_3}\left(1-w^2\right)^2, \quad w=\omega/\omega_{sr} && \text{Type I} \\ v_{in,comp}^2 &= 0.145\frac{g_m}{g_3} && \text{Type II} \end{aligned} \tag{3.33}$$

At frequencies higher than twice the self-resonance frequency, the type I has better compression performance.

Measured results

The measured conductance compression curves of both parallel-mode negative resistance types are shown in Figure 3.29. The circuits are again the same as in the noise measurements.

Type of response	Response, type I inductive Z_1 capacitive Z_2	Response, type II inductive Z_1 capacitive Z_2
fundamental	$v_{in}\left(\frac{g_m + j\omega C}{1-w^2}\right)$	$v_{in}\left(\frac{g_m + j\omega C}{1-w^2}\right)$
second harmonic	$\frac{v_{in}^2}{2}\frac{g_2}{(1-w^2)^2}$	$\frac{v_{in}^2}{2}\frac{g_2}{1-4w^2}$
third harmonic	$\frac{v_{in}^3}{4}\frac{g_3}{(1-w^2)^3}$	$\frac{v_{in}^2}{4}\frac{g_3}{1-9w^2}$
compression	$\frac{3v_{in}^3}{4}\frac{g_3}{(1-w^2)^3}$	$\frac{3v_{in}^2}{4}\frac{g_3}{1-w^2}$

Table 3.6 Harmonic distortion components for the parallel-mode negative resistors

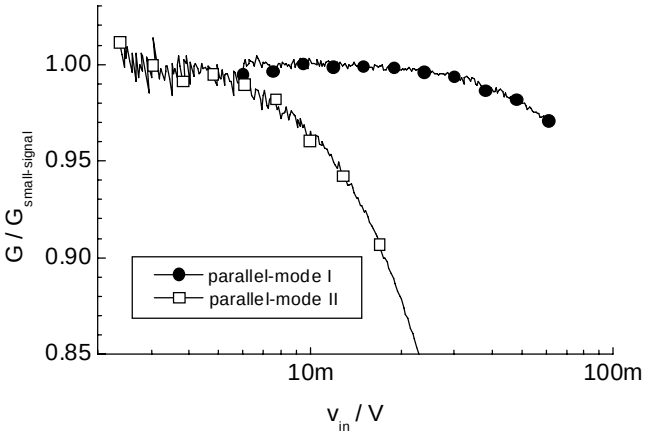

Figure 3.29 Measured conductance compression from a common-base and common-emitter BFR93A, I_c = 5 mA, f = 150 MHz, f_{sr} = 50 MHz

The self-resonance frequency of both measured circuits was about 50 MHz, and as the measuring frequency was three times higher (150 MHz), the type I ought to have approximately eight times higher a compression point than the type II by the theory. By examining Figure 3.29, an excellent match between the theory and the practice can be observed (2% compression voltages 50 mV and 7.6 mV), given the fact that even the slightest variation in the resonance frequency changes the distance between the compression points considerably.

3.6.5 Non-Linear Behavior of the Positive-g_m Parallel-Mode Negative Resistors

The harmonic components of the parallel-mode negative resistors with non-inverting transconductors follow basically the same format as those of normal parallel-mode negative resistors. They are listed in Table 3.7. The responses with inductive impedances Z_1 and Z_2 can be easily obtained by a substitution $\omega C_{1,2} \rightarrow 1/\omega L_{1,2}$ in the expressions.

Distortion performance cannot be enhanced without altering the fundamental negative conductance value, unless g_m is changed simultaneously. It is obvious that if the voltage division ratio in the transistor input is lowered (C_2/C_1 increased), the distortion performance of the whole circuit gets better at the expense of a larger need of transconductance. This requires more bias current through the device, which is often undesirable.

Type of response	Response, type I capacitive Z_1 and Z_2	Response, type II capacitive Z_1 and Z_2
fundamental	$v_{in}\frac{C_1}{C_1+C_2}\left(-g_m+j\omega C_2\right)$	$v_{in}\frac{C_1}{C_1+C_2}\left(-g_m+j\omega C_2\right)$
second harmonic	$-\frac{v_{in}^2}{2}g_2\left(\frac{C_1}{C_1+C_2}\right)^2$	$-\frac{v_{in}^2}{2}g_2\frac{C_1}{C_1+C_2}$
third harmonic	$-\frac{v_{in}^3}{4}g_3\left(\frac{C_1}{C_1+C_2}\right)^3$	$-\frac{v_{in}^3}{4}g_3\frac{C_1}{C_1+C_2}$
compression	$-\frac{3v_{in}^3}{4}g_3\left(\frac{C_1}{C_1+C_2}\right)^3$	$-\frac{3v_{in}^3}{4}g_3\frac{C_1}{C_1+C_2}$

Table 3.7 Harmonic distortion components for the positive-g_m parallel-mode negative resistors

The –1-dB compression points for the positive-g_m negative resistors become

$$\begin{aligned} v_{in,comp}^2 &= 0.145\frac{g_m}{g_3}\left(1+C_2/C_1\right)^2 \quad \text{Type I} \\ v_{in,comp}^2 &= 0.145\frac{g_m}{g_3} \qquad\qquad\quad \text{Type II} \end{aligned} \tag{3.34}$$

3.6.6 Effect of the Differential Transconductor

The non-inverting transconductor required by positive-gm negative resistors cannot be realized with a single transistor, and a twin-transistor CD-CG compound transconductor is needed. The same transistor configuration is also the basis of the differential circuits. It is commonly known that a differential transconductor suppresses even-order distortion components due to its anti-symmetrical nature. This also applies to the single-ended compound circuit in Figure 3.30, providing that the two component transconductors are of the same size.

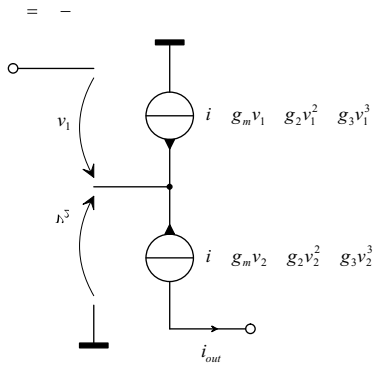

Figure 3.30 Simple non-linear model for the compound transconductor

The circuit in Figure 3.30 corresponds to a single non-inverting transconductor of the value

$$i_{out} = \frac{g_m}{2}v_{in} + \frac{1}{4}\left(\frac{g_3}{2}-\frac{g_2^2}{g_m}\right)v_{in}^3 = g_{mc}v_{in} + g_{3c}v_{in}^3 \tag{3.35}$$

The combined transconductance value has been halved, and twice the bias current of an inverting single-transistor transconductor will be needed. The second-order component has disappeared, but the relative value of the third-order component has grown ($g_3 < 0$).

The absence of the second-order coefficient g_{2c} has an effect on the distortion performance in the series-mode circuits where g_{2c} contributes directly to the third-order harmonic distortion and compression responses. On the other hand, in the parallel-mode negative resistors the second-order coefficient has no effect on the third-order responses, and the degraded g_{3c} even worsens the situation. Therefore, twin-transistor parallel-mode negative resistors do not benefit from the compound transconductances.

3.7 Dynamic Range of Negative Resistance Resonators

3.7.1 Definition

The definition of dynamic range is futile if the frequency band is not limited. Therefore, it is necessary to examine the whole negative resistance resonator with a well-specified limited frequency band.

When a negative resistor is connected in parallel with a lossy LC resonator, its small-signal value ought to compensate the unloaded resonator losses completely at resonance. The current through the negative resistor is the sum of the fundamental response current and the compression current, as described earlier. Now, the fundamental response is totally cancelled by the passive resonator dissipation resistance, and the only first-order term left is the current through the load resistor G_l. We can write the compression condition:

$$\frac{v_{in,comp}G_l - \left|\mathrm{Re}\{i_{in}(compression)\}\right|}{v_{in,comp}G_l} = 89.1\% \;\Rightarrow\; Q_l\frac{\left|\mathrm{Re}\{i_{in}(compression)\}\right|}{v_{in,comp}\omega_0 C} = 10.9\% \qquad (3.36)$$

This equation gives the input voltage at which the total resonator input current, or the resonator input power, is compressed –1 dB from its small-signal value.

We can combine Equations (3.29) and (3.36), and as the fundamental response in Eq. (3.29) must now be equal to $\omega_0 C/Q_0$, we get

$$\frac{\mathrm{Re}\{i_{in,negres}(comp)(v_{in,comp,negres})\}}{v_{in,comp,negres}}Q_0 = \frac{\mathrm{Re}\{i_{in,negres}(comp)(v_{in,comp,reson})\}}{v_{in,comp,reson}}Q_l \qquad (3.37)$$

Since the third-order compression terms are proportional to v^3, the expression becomes

$$v^2_{in,comp,reson} = \frac{Q_0}{Q_l}v^2_{in,comp,negres} \qquad (3.38)$$

This important equation shows the relation between the -1-dB compression voltages of the negative resistor and the corresponding compensated LC resonator at resonance. The same result has been obtained in [3.20] and [3.24] after somewhat inaccurate analyses, though.

The dynamic range of an active resonator can now be defined as the ratio:

$$DR = \frac{Q_0}{Q_l}\frac{v^2_{in,comp,negres}}{(\text{rms noise voltage})^2} \qquad (3.39)$$

3.7.2 Negative Resistance Resonator Noise

The total noise of a negative-resistance compensated resonator consists of the contributions of the passive resonator noise and the negative resistance noise. At a narrow band, the parallel conductance of the negative resistor is equal to that of the lossy resonator, so that the unloaded net conductance is zero. The injected noise current becomes

$$\begin{aligned} \hat{i}_n^2 &= \hat{i}_{n,res}^2 + \hat{i}_{n,neg}^2 = 4kTG_p(1+r_n) \quad \text{series-mode} \\ \hat{i}_n^2 &= \hat{i}_{n,res}^2 + \hat{i}_{n,neg}^2 = 4kTG_p(1+g_n) \quad \text{parallel-mode} \end{aligned} \tag{3.40}$$

provided that the loaded Q of the resonator is high enough. Thus, near resonance the noise voltage spectral density of the negative resistance resonator is

$$\hat{v}_n^2 \approx \frac{\hat{i}_n^2}{\left| G_l + j\omega C + \frac{1}{j\omega L} \right|^2} = 4kTG_p(1+r_n, g_n) \frac{\omega^2 L^2}{\omega^2 L^2 G_l^2 + (\omega^2 LC - 1)^2} \tag{3.41}$$

At resonance this yields

$$\hat{v}_n^2\big|_{\omega_0} = 4kT\left(1+r_n, g_n\big|_{\omega_0}\right)\frac{G_p}{G_l^2} = 4kTR\left(1+r_n, g_n\big|_{\omega_0}\right)Q_l^2 \tag{3.42}$$

Consequently, the total rms noise voltage of the negative resistance resonator becomes

$$\bar{v}_n^2 = \frac{1}{2\pi}\int_0^\infty \hat{v}_n^2 d\omega \approx \frac{kT}{C}\frac{Q_l}{Q_0}\left(1+r_n, g_n\big|_{\omega_0}\right) \tag{3.43}$$

It is assumed that the relative noise resistances and conductances are constant over the narrow resonator bandwidth, when Q_l is high.

The noise performance of the different negative resistor types can be easily compared by looking into their relative noise resistances or conductances. Nevertheless, the greatest effect has the ratio of the loaded Q of the resonator and the unloaded Q of the inductor/capacitor. With low-Q components, noise is excessive in narrow-band filters regardless of the negative resistor type.

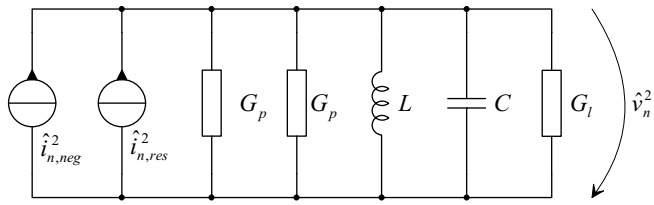

Figure 3.31 Negative resistance resonator noise

3.7.3 Dynamic Range of Negative Resistor Resonators

By combining the results from Equations (3.39) and (3.43), we can define the dynamic range of any negative resistance resonator:

$$DR = 10\log\frac{v_{in,comp}^2}{\bar{v}_n^2} = 10\log\left(\frac{Q_0}{Q_l}\right)^2 \frac{v_{in,comp}^2 C}{kT\left(1 + r_n, g_n\big|_{\omega_0}\right)} \tag{3.44}$$

The ratio Q_0/Q_l is crucial when the dynamic range is to be maximized. For instance, almost a 10-dB enhancement in the dynamic range is achieved if the passive inductor quality factor is increased from 5 to 15.

For a series-mode negative resistor we get by Eq. (3.31)

$$DR = 10\log\frac{v_{in,comp}^2}{\bar{v}_n^2} = 10\log\frac{0.145}{K_C}\left(\frac{Q_0}{Q_l}\right)^2 \frac{g_m\left(g_m^2 + \omega_0^2(C_1 + C_2)^2\right)^2 C}{kT\left(1 + \gamma C_2 \big/ C_1\right)\omega_0^2 C_1^2} \tag{3.45}$$

Respectively, the dynamic ranges of the parallel-mode negative resistors can be derived from the appropriate equations. For the types I and II, they become:

$$\begin{aligned} DR &= 10\log\left(\frac{Q_0}{Q_l}\right)^2 \frac{0.145 g_m (w^2-1)^2 C}{g_3 kT\left(1 + \gamma(w^2-1)\right)} \quad \text{Type I} \\ DR &= 10\log\left(\frac{Q_0}{Q_l}\right)^2 \frac{0.145 g_m C}{g_3 kT\left(1 + \gamma/(w^2-1)\right)} \quad \text{Type II} \end{aligned} \tag{3.46}$$

And finally for the positive-g_m circuits

$$\begin{aligned} DR &= 10\log\left(\frac{Q_0}{Q_l}\right)^2 \frac{0.145 g_m (1 + C_2/C_1)^2 C}{g_3 kT\left(1 + \gamma(1 + C_2/C_1)\right)} \quad \text{Type I} \\ DR &= 10\log\left(\frac{Q_0}{Q_l}\right)^2 \frac{0.145 g_m C}{g_3 kT\left(1 + \gamma/(1 + C_2/C_1)\right)} \quad \text{Type II} \end{aligned} \tag{3.47}$$

The resonating capacitance C includes any eventual stray capacitance coming from the negative resistance, and therefore there is a connection between the internal capacitance of the negative resistor and the total resonating capacitance. Preferably, the contribution from the negative resistor capacitances is kept small, as they tend to vary along with resistance tuning.

3.7.4 Comparison

To get a hands-on view of the theoretical dynamic ranges of each negative resistor type it is necessary to compare the topologies with realistic numerical values of components. The exemplary parameters chosen for the comparison are:

- ω_0 = 4 GHz , Q_l = 100
- resonating L = 2 nH, Q_0 = 15
- g_m = 10 mS, g_2 = 2 mA/V^2, g_3 = -200 µA/V^3 (TriQuint MESFET 4 x 16µm)
  (g_{mc} = 10 mS, g_{2c} = 0, g_{3c} = -1.0 mA/V^3 for compound transconductors with double-size transistors)

For simplification, the negative resistor components are chosen in such a way that the resonance condition is fulfilled, i.e. no external capacitance is connected. This can be regarded as the

worst case scenario but gives a good basis for comparison. The numerical results are gathered in Table 3.8:

Type of negative resistor		rms noise voltage / µV	compression voltage / dBmV	dynamic range / dB
series-mode	$C_1 > C_2$	206	56	70
	$C_1 < C_2$	515	70	76
parallel-mode	type I	612	78	82
	type II	199	60	74
twin-transistor parallel-mode	type I	574	71	76
	type II	199	53	67

Table 3.8 Computational noise voltages, compression points and dynamic ranges for the different negative resistor topologies

There is practically little difference between the dynamic ranges of the negative resistor topologies considered here, although the parallel-mode circuits seem to be the best. Due to the differential pair, the twin-transistor circuits suffer from slightly higher third-order distortion components than the others. It must be noted, however, that if inverting-transconductor circuits were to be realized in (quasi-)differential form, their distortion performance would be inferior to that of the circuits with non-inverting transconductors.

In actual circuits, it is impossible to achieve the figures shown in Table 3.8, as the distortion mechanisms are much more complex in reality. For instance, the non-linear input capacitances of the transistors have non-negligible effect on performance, but it is reasonable to assume that all the circuits suffer from them in a similar way. The distortion definitions here only give some guidelines for dimensioning negative resistors, and the absolute numerical figures are only valid for theoretical comparisons between different negative resistance structures.

In the calculations it is assumed that the resonating capacitance is noiseless and linear. This is not true in realistic resonators, which has a considerable effect on noise and distortion, and thus dynamic range in the resonator. The properties of the negative resistors themselves are not affected, but in a direct comparison with gyrator-based resonators, the non-ideal resonating capacitor, often a varactor, must be taken into account.

3.8 Practical Negative Resistor Resonators

Practical aspects of negative resistor resonator design are discussed in this section. Realized circuit examples are given on the basis of published articles. Measured data is presented when available.

3.8.1 Feasibility for Integration

The previous sections deal with the underlying theoretical background of different negative resistor types. However, many of the seemingly good topologies suffer from considerable performance deterioration when realized as integrated circuits. The main causes are process tolerances, especially in passive components, biasing arrangements and supply voltage sensitivities.

Spiral inductors are the lowest-quality passive components in integrated circuits, and therefore they should be avoided whenever possible. In negative resistors that employ inductors, i.e. series-mode circuits with inductors and single-transistor parallel-mode circuits, positive loss resistance is generated by the loss resistances of the inductors. This can be compensated by increasing the negative resistance value at the expense of power consumption, which is naturally undesirable. The inductive series-mode resistors also include two spiral inductors increasing the required die area.

All the negative resistor topologies, except the twin-transistor type with unity feedback, rely on passive auxiliary components in synthesizing negative resistance. Thus, the values of these components directly affect the negative resistance value. As absolute variations of integrated passive components are large, the uncertainty of the resulting negative resistance is high. Topologies where the ratio of passive component values rather than their absolute values is determining are far better suited for integration, as the relative component variations are small. The parallel-mode inverted-g_m negative resistors meet this requirement, and for their robustness, they are best suited for realization as integrated circuits. Naturally, all negative resistor types can be tuned and adapted to variations, but if their tuning ranges are narrow, this may not suffice.

Biasing of the active devices introduces more non-idealities to the practical circuits. DC bias voltages and currents must be provided for the transistor inputs and outputs. In many cases some of these can be brought into the circuit via DC-coupled resonator inductors, and since the inductors are inseparable parts of the total resonator circuits, no performance reduction follows. For instance, the outputs of the differential negative resistor transistors [Section 3.4] get their DC bias voltages and currents through the actual resonating inductors connected to the positive supply. Topologies where an inductor is connected between the base and the collector of the transistor (Figure 3.10b,d and Figure 3.11b,c) do not need further base bias in bipolar realizations, if zero base-collector voltage is permitted. Following the same pattern, an inductor between the gate and the source of the transistor enables easy biasing to I_{dss} in FET circuits (Figure 3.6b and Figure 3.10a,c). The freedom of choosing bias points is lost in these cases, though, and the transconductances of the FETs become fixed making tuning difficult. For totally independent biasing, the inductors must be AC-coupled via capacitors, and the bias voltages and current must be provided via as large resistors as possible. The bias resistors have also a negative effect on noise performance.

The resistance tuning of negative resistance circuits is usually best achieved by adjusting the device transconductances. This necessitates the utilization of a controllable current source that feeds the core transistors. The current source is realized as an additional transistor with non-zero output conductance. The current source transistor loads the negative resistor, increasing the amount of negative resistance needed for compensation. In the best topologies, the current source connects to a low-impedance point where its non-idealities are least visible, like in differential parallel-mode negative resistors.

Supply voltage sensitivity is an issue in integrated circuits where its stability cannot always be ensured. This is a problem in single-transistor topologies, as their performance is very much affected by the transistor parasitics which in turn are supply-dependent. The extent of supply sensitivity is so great in these circuits that the operating voltages can be regarded as tuning voltages. The twin-transistor positive-g_m negative resistors do not suffer from this phenomenon.

Considering all the practical problems discussed here, it becomes clear that the positive-g_m negative resistors, such as the differential cross-coupled pairs, are most feasible in terms of integration, although single-transistor topologies might show better theoretical performance in some cases.

3.8.2 Realized Single-Ended MESFET Negative Resistor Resonator

A negative resistance can be realized with a positive transconductance and unity feedback usually found in VCO circuits (Figure 3.32). If the identical transistors are modeled with the transconductance g_m, the output conductance g_{ds} and the gate-source capacitance C_{gs}, the single-ended input admittance becomes

$$Y_{in} = -\frac{g_m - g_{ds}}{2} + j\omega\frac{C_{gs}}{2} \tag{3.48}$$

corresponding to a negative resistor in parallel with a capacitor. When connected in parallel with a lossy LC resonator, the minimum Q value of the inductor that just can be compensated with a given g_m is

$$Q \approx \sqrt{\frac{C}{L}} \frac{2}{g_m - g_{ds}} \tag{3.49}$$

where L and C are the passive resonator component values. In practice, Q-values of less than five can easily be compensated. Since the basic operation relies only on the transconductance, sensitivity to parasitics and to the supply voltage is inherently low, and tuning is trivial by changing the drain currents. The input nodes are the same for the signal and for the drain bias, which makes it possible to use a single passive inductor as both the resonating and biasing element. The nodal impedances are low, and the maximum possible voltage swing can be obtained at the input.

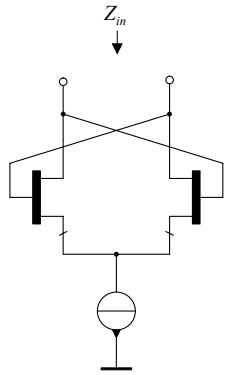

Figure 3.32 Differential negative resistance

An integrated single-ended resonator with active negative resistance loss compensation was designed for the GEC-Marconi F20 GaAs-MESFET process [3.14]. The targeted center frequency was 2.4 GHz, which is tunable within +/- 100 MHz via a varactor-connected MESFET. The schematic of the circuit is shown in Figure 3.33, and a photograph of the layout in Figure 3.34. The chip size without the RF and bias pads is 0.6×0.6 mm^2.

The sizes of the transistors are 1×100µm. For optimum noise performance, they are biased to approximately 20% of I_{dss}. The external bias adjusts the current and g_m of the two MESFETs, and thus the Q value of the resonator. In a practical filter, this adjustment is essential for optimum response and stability. A compensation capacitance can be added in parallel with the current source MESFET to lower the effective gain at high frequencies. This brings the absolute conductance minimum within the frequency tuning range and further desensitizes the circuit against variations of the transistor C_{gs}. The varactor size is 4×80µm giving a capacitance range of 0.2 - 0.6 pF.

Hewlett-Packard's MDS and Helsinki University of Technology's APLAC simulation software, and the Parker-Skellern MESFET model with enhanced capacitance descriptions were used throughout the design [3.25][3.26][3.27]. The model gives an excellent match between simulations and measurements in the normal operating region of a device but unfortunately, it does not model resistive losses in a varactor-connected MESFET properly. The difficulty of obtaining a meaningful equivalent circuit in the cold FET region into which the I-V and C-V models fit, and the high sensitivity of the circuit to the bias dependence of the gate resistance, are the main problems in the model extraction. This led to far too high a varactor Q value in the simulations, resulting in a downward shift of the conductance minimum frequency, and

naturally a requirement for larger currents to compensate the extra loss. These were not taken into account in the original simulations. Consequently, the frequencies of the conductance minimum and the resonance do not coincide as expected, and the power consumption is somewhat higher. The effective series resistance of a varactor is a non-linear function of its bias, giving lower values along with decreasing V_g. A very good agreement between the measured performance of the resonator and the CAD model was obtained by increasing the series resistance of the varactor with a 15-Ω resistor in the device model.

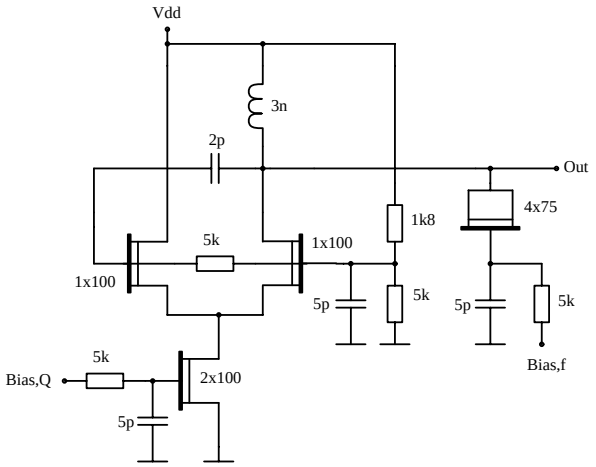

Figure 3.33 Schematic diagram of the designed MESFET negative resistor resonator

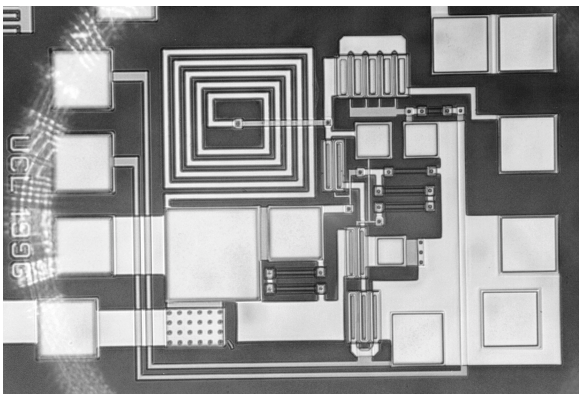

Figure 3.34 Microphotograph of the resonator circuit

The measured input admittance is shown in Figure 3.35. The operating point is I_{dc} = 9 mA, $V_{bias,f}$ = 2.8 V, and $V_{bias,Q}$ = -0.65 V. The unaccounted varactor loss has shifted the conductance minimum down to 1.9 GHz. This does not cause any stability problems as long as no resonance occurs in the region where $\mathrm{Re}\{Y_{in}\}$ is negative. Both the conductance and susceptance curves cross zero at almost the same frequency point resulting in a very high unloaded Q.

Figure 3.36a shows the resonance frequency as a function of the varactor tuning voltage $V_{bias,f}$ for different Q-tuning voltages $V_{bias,Q}$. The change in frequency, when $V_{bias,Q}$ is varied, is due to the bias-dependent gate-source capacitances in the MESFETs even with a constant frequency tuning voltage. The Q tuning, or the conductance tuning characteristics are shown in Figure 3.36b. High-Q operation and, on the other hand, stability can be assured with the wide tuning range around zero conductance.

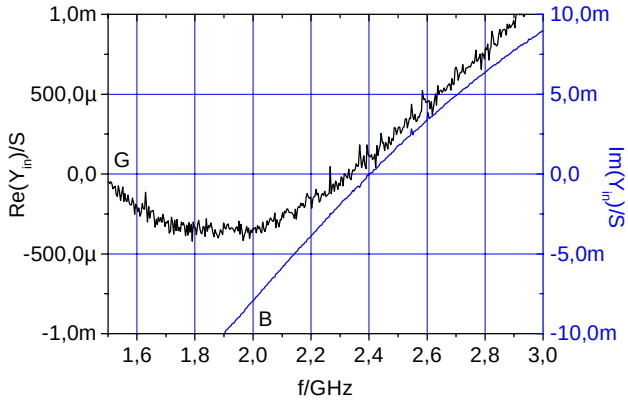

Figure 3.35 Measured Y_{in} of the MESFET negative resistor resonator

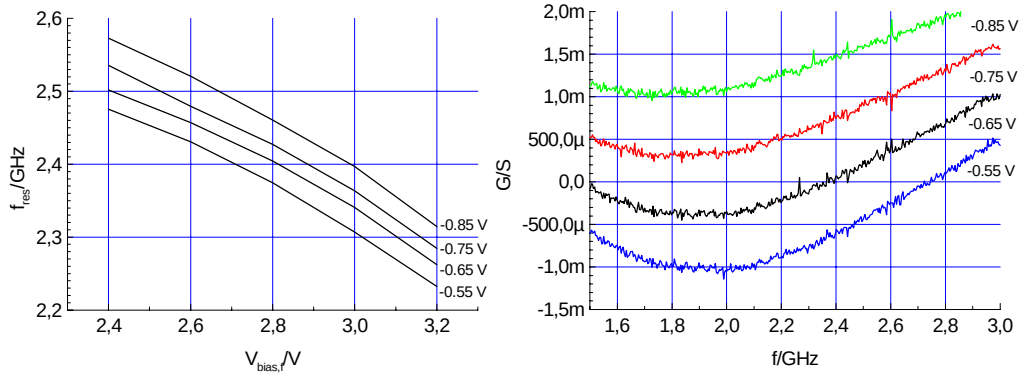

Figure 3.36 a) Resonance frequency tuning ($V_{bias,f}$); b) Conductance tuning ($V_{bias,Q}$)

The insensitivity to the supply voltage is demonstrated in Figure 3.37. The increase of $|S_{11}|$ is only about 0.5 dB, when the operating voltage is raised from 2.5 V to 3.0 V, and 0.25 dB from 3.0 V to 4.0 V. These minor deviations can easily be compensated by adjusting the biases accordingly.

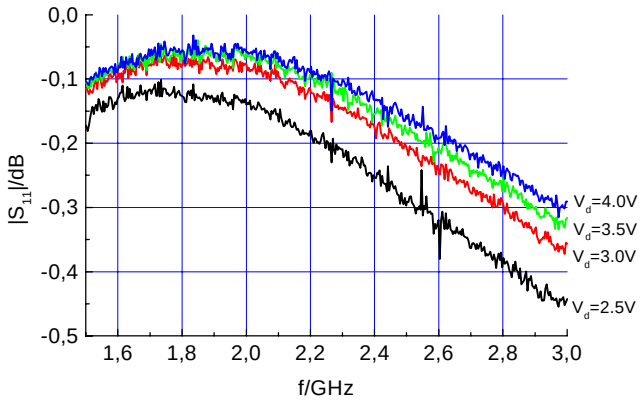

Figure 3.37 Sensitivity to the supply voltage

The 1-dB power compression point was measured by feeding a variable-power signal at the resonance frequency into the circuit and observing the reflected power level. The difference between the two power levels i.e. the 'gain' of the circuit is shown in Figure 3.38. The result is 9.5 dBm corresponding to an input voltage swing of approximately 1.3 V_{pp}. This is not the conductance compression point discussed in Section 3.6, though, as power compression is very much affected by the varactor.

The main factor limiting the large signal performance is not the active negative resistance itself but the capacitance non-linearity of the diode connected MESFET. This can be improved by adding another varactor in the back-to-back connection [Section 2.5.1]. This cuts the resonating capacitance value in half, and in order to maintain the same resonance frequency the inductor value or preferably the varactor size must be doubled.

The noise performance of the resonator could not be measured by standard means, since the circuit was only realized as a one-port. More information can be obtained from the filter-mode measurements discussed in Chapter 5.

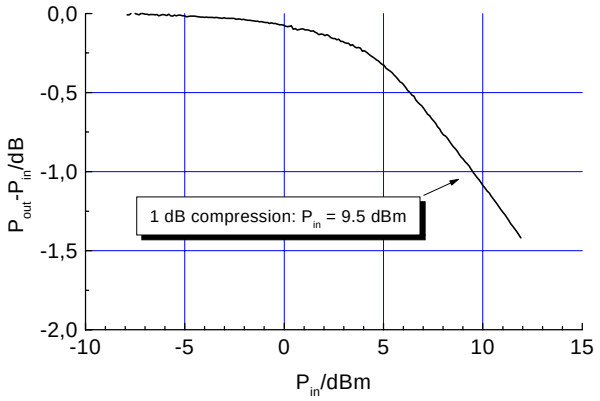

Figure 3.38 Large signal performance of the MESFET resonator

References

[3.1] E. H. Armstrong, 'The Regenerative Circuit,' *Proceedings Radio Club of America*, April 1915.

[3.2] E. H. Armstrong, 'Some Recent Developments of Regenerative Circuits,' *Proceedings of the IRE*, Vol. 10, pp. 244-260, August 1922.

[3.3] W. O. Swinyard, 'The Development of the Art of Radio Receiving from the Early 1920's to the Present,' *Proceedings of the IRE*, Vol. 50, pp. 793-798, May 1962.

[3.4] C. Buff, 'Radio Recevers – Past and Present,' *Proceedings of the IRE*, Vol. 50, pp. 793-798, May 1962.

[3.5] A. Presser, 'Varactor-Tunable, High-Q Microwave Filter,' *RCA Review*, Vol. 42, pp. 691-705, December 1981.

[3.6] S. Chandler, I. Hunter and J. Gardiner, 'Active Varactor Tunable Bandpass Filter,' *IEEE Microwave and Guided Wave Letters*, Vol. 3, pp. 70-71, March 1993.

[3.7] U. Karacaoglu and I. Robertson, 'MMIC Active Bandpass Filters Using Varactor-Tuned Negative Resistance Elements,' *IEEE Transactions on Microwave Theory and Techniques*, Vol. 43, pp. 2926-2932, December 1995.

[3.8] J. Macedo and M. Copeland, 'A 1.9-GHz Silicon Receiver with Monolithic Image Filtering,' *IEEE Journal of Solid-State Circuits*, Vol. 33, pp. 378-386, March 1998.

[3.9] W. Aparin and P. Katzin, 'Active, Self-Adjusting L-S Band MMIC Filters,' *IEEE GaAs IC Symposium Digest*, pp. 41-44, 1994.
[3.10] W. Aparin and P. Katzin, 'Active GaAs MMIC Band-Pass Filters with Automatic Frequency Tuning and Insertion Loss Control,' *IEEE Journal of Solid-State Circuits*, Vol. 30, pp. 1068-1073, October 1995.
[3.11] C. Chang and T. Itoh, 'Microwave Active Filters Based on Coupled Negative Resistance Method,' *IEEE Transactions on Microwave Theory and Techniques*, Vol. 38, pp. 1879-1884, December 1990.
[3.12] D. Adams and R. Ho, 'Active Filters for UHF and Microwave Frequencies,' *IEEE Transactions on Microwave Theory and Techniques*, Vol. 17, pp. 662-670, September 1969.
[3.13] B. Hopf, I. Wolff and M. Gugliemi, 'Coplanar MMIC Active Bandpass Filters Using Negative Resistance Circuits,' *IEEE Transactions on Microwave Theory and Techniques*, Vol. 42, pp. 2598-2602, December 1994.
[3.14] R. Kaunisto, D. Webster and D. Haigh, 'Improved MMIC Active Filters Based on Passive LC Resonators with Active Negative Resistance Circuits,' *Proceedings of IEE Colloquium on Advanced Signal Processing for Microwave Applications*, Stevenage UK, pp. 3/1-3/6, November 1996.
[3.15] R. Kaunisto, K. Stadius and V. Porra, 'Active MMIC Filters with Negative resistance Compensation,' *Electronic Letters*, Vol. 34, pp. 1236-1237, June 1998.
[3.16] W. Kuhn, F. Stephenson and A. Elshabini-Riad, 'A 200 MHz CMOS Q-Enhanced LC Bandpass Filter,' *IEEE Journal of Solid-State Circuits*, Vol. 31, pp. 1112-1122, August 1996.
[3.17] W. Kuhn, N. Yanduru and A. Wyszynski, 'Q-Enhanced LC Bandpass Filters for Integrated Wireless Applications,' *IEEE Transactions on Microwave Theory and Techniques*, Vol. 46, pp. 2577-2585, December 1998.
[3.18] R. Duncan, K. Martin and A. Sedra, 'A Q-Enhanced Active RLC Bandpass Filter,' *IEEE Transactions on Circuits and Systems – II*, Vol. 44, pp. 341-347, May 1997.
[3.19] S. Pipilos and Y. Tsividis, 'Design of Active RLC Integrated Filters with Application in the GHz Range,' *1994 IEEE International Symposium Circuits Syst. Dig.*, pp. 645-648.
[3.20] S. Pipilos, Y. Tsividis, J. Fenk and Y. Papananos, 'An Si 1.8 GHz RLC Filter with Tunable Center Frequency and Quality Factor,' *IEEE Journal of Solid-State Circuits*, Vol. 31, pp. 1517-1525, October 1996.
[3.21] P. Gray and R. Meyer, 'Analysis and Design of Analog Integrated Circuits – Second Edition,' John Wiley, New York, 771 p., 1984.
[3.22] P. Wambacq and W. Sansen, 'Distortion Analysis of Analog Integrated Circuits,' Kluwer Academic Publishers, Dordrecht, 501 p., 1998.
[3.23] S. Maas, 'Non-linear Microwave Circuits,' Artech House, Norwood, 478 p., 1988.
[3.24] W. Kuhn, F. Stephenson and A. Elshabini-Riad, 'Dynamic Range of High-Q OTA-C and Enhanced-Q LC RF Bandpass Filters,' *Proceedings of IEEE Midwest Symposium on Circuits and Systems*, pp. 767-771, 1994.
[3.25] A. Parker, 'Implementing SPICE Models with High-Order Continuity and Rate Dependence,' *IEE Proceedings of Circuit, Devices and Systems*, Vol. 141, pp. 251-257 April 1994.
[3.26] A. Parker, J. Scott, 'Modelling and Characterisation of GaAs Devices,' Chapter 6 of Low Power HF Microelectronics, Ed. G. Marchado, IEE Books, London, 1028 p., 1996.
[3.27] D. Webster, M. Darvishzadeh and D. Haigh, 'Improved Total Charge Capacitor Model for Short Channel MESFETs,' *IEEE Microwave and Guided Wave Letters*, Vol. 6, pp. 351-353, October 1996.

4. GYRATOR RESONATORS

4.1 Historical Perspective

4.1.1 Passive Magnetic Gyrators

In 1948, a new two-port network element was proposed by B. D. H. Tellegen of Philips Research Laboratory [4.1]. Tellegen realized that all two-ports containing only resistors, capacitors, inductors and transformers are linear, constant, passive and reciprocal. In order to find a new fundamental element, he had to rule out one of these properties. He considered the last one, reciprocity, to be of least importance in the network theory, and suggested that a new non-reciprocal element, the gyrator, can be regarded as the fifth fundamental circuit element. The ideal passive gyrator is described by

$$\begin{bmatrix} i_1 \\ i_2 \end{bmatrix} = \begin{bmatrix} 0 & g \\ -g & 0 \end{bmatrix} \begin{bmatrix} v_1 \\ v_2 \end{bmatrix} \tag{4.1}$$

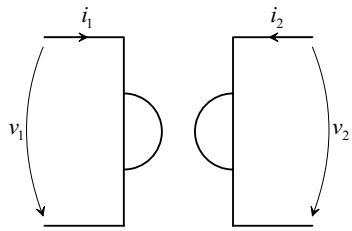

Figure 4.1 Symbol for the ideal gyrator as proposed by Tellegen

The quantity g is called 'gyration conductance'. Tellegen noticed that a capacitance connected to the secondary terminals will look like an inductor at the primary terminals $L = C/g^2$, or vice versa $C = g^2L$. This is the most important property of the gyrator, as it enables the synthesis of inductors. More generally, any admittance Y connected to the secondary terminals is converted to its dual g^2/Y. This phenomenon is called immittance conversion.

The name gyrator origins from the gyroscopic terms that occur in the state equations of coupled rotating masses. In fact, a mechanical gyrator (a gyroscopic coupler) can be demonstrated. Tellegen presented the electric equivalents of gyroscopic state equations and suggested that a construction in Figure 4.2 could function as a gyrator.

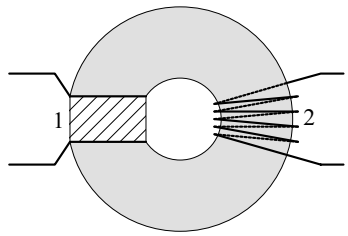

Figure 4.2 Construction of a passive gyrator

The medium between the electrodes of the primary terminal must consist of particles carrying both permanent electric and permanent magnetic dipoles. By Tellegen, these conditions can be met with small ferromagnetic filings in an appropriate fluid. Alternatively,

media with gyromagnetic properties can be used. Magnetic gyrators have also been realized by using the Hall effect in a semiconductor [4.2] or the Faraday effect in a ferrite [4.3]. Yet another method of constructing a passive gyrator is to exploit the non-reciprocal properties of coupled electric and magnetic transducers (the piezoelectric-piezomagnetic gyrator [4.4]). It is clear that these kind of passive gyrators have little practical importance in filter design, and they should be regarded only as demonstrations of the gyrator effect. However, ferromagnetic circulators are widely used as gyrators in microwave circuits.

4.1.2 Electronic Gyrators

When the two gyrator conductances g are equal, the gyrator is passive and non-dissipative. In general, this need not be the case, and the gyrator conductances can be unequal but still opposite in sign. Then, depending on their ratios, the gyrator is either active or dissipative. The conductance matrix can be split into two parts:

$$\mathbf{y} = \begin{bmatrix} 0 & g_1 \\ 0 & 0 \end{bmatrix} + \begin{bmatrix} 0 & 0 \\ -g_2 & 0 \end{bmatrix} \tag{4.2}$$

Now the matrices correspond to ideal voltage-controlled current sources, i.e. transconductors, with opposite signs. This brings up the principle of the electronic gyrator:

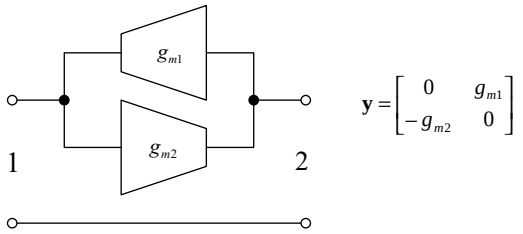

Figure 4.3 Electronic gyrator

To form an active inductor, a capacitor is connected to one port. The impedance seen from the other port is then, according to the immittance conversion theorem,

$$L = \frac{C_g}{g_{m1} g_{m2}} \tag{4.3}$$

where C_g is the port capacitance, the gyrator capacitance.

One of the first electronic gyrators was presented by Bogert in 1955 [4.5], but the concept really made advances during the following years, when transistors became readily available. Several electronic gyrators based on antiparallel transconductors were presented in the 1960's [4.6][4.7][4.8]. The main objective at that time, as well as nowadays, was to realize inductorless filters. As transistors were becoming cheaper, it was predicted that they would replace the costly wound inductors in some sense or another in the future. Orchard [4.9] suggested that the best way of designing inductorless filters is to replace each inductor in a conventional LC ladder filter by a synthesized inductor, i.e. a capacitively terminated gyrator. This is because of the inherent insensitivity of LC ladder filters, although rather many active components are needed.

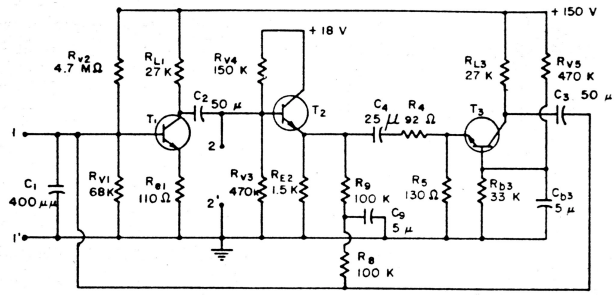

Figure 4.4 Typical gyrator topology from 1965 [4.6]

The first partially integrated gyrators began to show in the early 1970's along with the development of integrated operational amplifiers [4.10][4.11]. However, the rapid evolution of other active continuous-time and especially discrete-time filtering techniques, like switched-capacitor filters, made gyrator filters obsolete very soon in terms of integration. Only after high-frequency integrated circuits and MMICs became a hot topic in the late 1980's, integrated microwave gyrators became potential circuit elements for active filtering.

4.1.3 MMIC Gyrators

The need for minimization of mobile radio RF front ends led to growing interest in high-frequency integrated circuits in the 1980's. Many of the functional blocks of a radio transceiver could be realized monolithically, but filters remained a major problem. Although integrated spiral inductors were now available, their quality factors were unacceptably low for filtering. They also occupied a lot of expensive chip area. Traditional active filters could not be used, as high gain amplifiers or sufficiently fast clock signals were unrealizable. In this context, S. Hara revived the old idea of gyrator-based active inductors in 1988 [4.12].

Hara's active inductors are shown in Figure 1.5. They are nothing but ordinary gyrators where the gate-source capacitance of the inverting MESFET acts as the termination capacitor. The inverting stage is cascode-connected for increased bandwidth. In the first version [4.12], the non-inverting transconductor is simply realized as a resistor, whereas the second version [4.13] employs a common-gate MESFET.

Later, the problems concerning the Q value of Hara's inductors were elaborated by the author, which lead to studies on phase compensation techniques [4.14] – [4.17].

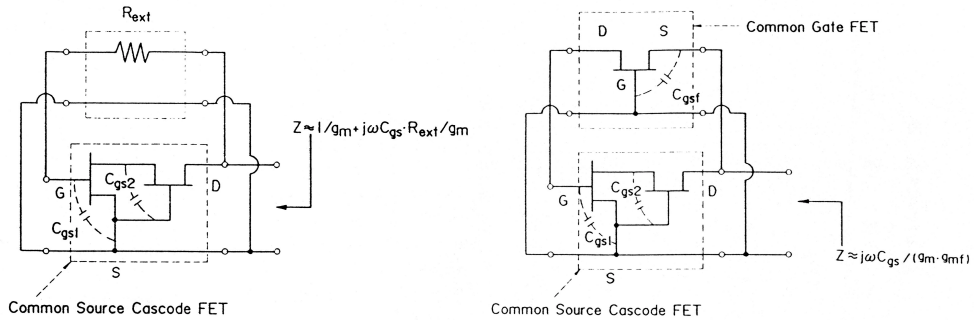

Figure 4.5 Hara's two types of active inductors [4.12][4.13]

4.2 Non-Ideal Gyrators

Ideal electronic gyrators do not exist in practice; therefore, it is imperative to consider the mechanisms causing imperfections and their effects on the gyrator performance. The y-matrix in Equation (4.4) describes a non-ideal gyrator:

$$\mathbf{y} = \begin{bmatrix} y_{p1} & g_{m1}e^{-j\phi_1} \\ -g_{m2}e^{-j\phi_2} & y_{p2} \end{bmatrix} \tag{4.4}$$

The complex gyration admittances $g_{m1}e^{-j\phi 1}$ and $g_{m2}e^{-j\phi 2}$ describe the phase shift in the transconductors. The non-zero diagonal elements y_{p1} and y_{p2} represent the parasitic admittances at the corresponding ports. They occur as a result of the finite output conductances in the transconductors. Imperfections due to an external biasing network will alter the port impedances and thus affect on the gyrator performance, too.

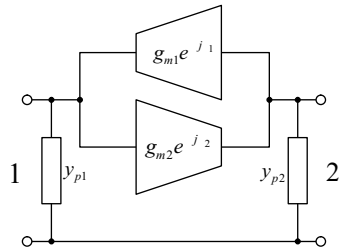

Figure 4.6 Non-ideal gyrator

4.2.1 Non-Ideal Transconductor

The simplified non-ideal transconductor used in the theoretical studies is shown below. It consists of an input resistance r_i and a capacitance c_i, which can be identified as the base (gate) resistor and the base-emitter (gate-source) capacitor of a bipolar (field-effect) transistor in a single-transistor inverting transconductor. The output resistor r_o corresponds to the output conductance of the transistor, respectively. In addition, the transconductance element itself has limited bandwidth and phase shift due to the transit-time effect. If compared to the previous factors, it is of little importance, though. Other phase-shifting elements not shown here, such as output and Miller capacitances, can be embedded into the gyrator or the resonating capacitor and the input capacitor c_i.

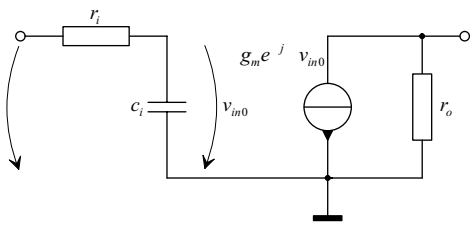

Figure 4.7 Non-ideal transconductor

4.2.2 Effects of Finite Transconductor Bandwidth and Phase Lag

Neglecting the transit-time effect, the input network of the transconductor can be described also with a complex transconductor element g_m' according to the following relation:

$$g_m v_{in0} = \frac{g_m v_{in}}{1 + j\omega r_i c_i} = g'_m e^{-j\phi_i}, \quad g'_m = \frac{g_m}{\sqrt{1+\omega^2 r_i^2 c_i^2}}, \quad \phi_i = \arctan \omega r_i c_i \tag{4.5}$$

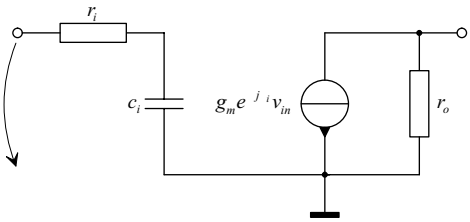

Figure 4.8 Non-ideal transconductor with a complex g_m

The pole at input results in a limited transconductor bandwidth and changes the inductance value at high frequencies. The phase lag -ϕ_i corresponds to negative resistance and leads to instability in the absence of Q-degrading losses.

4.2.3 Effects of Non-ideal Port Impedances

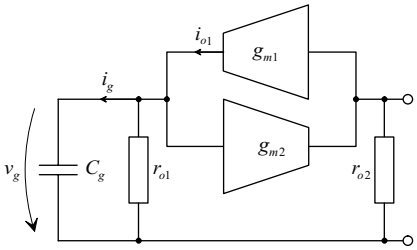

Figure 4.9 Active inductor with non-zero output conductances

The output impedance of one transconductor and the input impedance of the following one connect directly in parallel with the corresponding port impedance and cause deviations in the inductance value and the quality factor. The parasitic capacitive components increase the value of the gyrator capacitance and hence the gyrator inductance, whereas the resistive components decrease the quality factor. The voltage across the gyrator capacitor (and the input voltage of the other g_m) can be expressed as

$$\begin{aligned} v_g &= \frac{i_g}{j\omega C_g} = \frac{i_{o1}}{j\omega C_g} \frac{j\omega r_{o1} C_g}{1 + j\omega r_{o1} C_g} = \frac{g'_{m1} e^{j\phi_{o1}}}{j\omega C_g} v_{in,gm1}, \\ g'_{m1} &= \frac{g_{m1}}{\sqrt{1+1/\omega^2 r_{o1}^2 C_g^2}}, \quad \phi_{o1} = \arctan 1/\omega r_{o1} C_g \end{aligned} \tag{4.6}$$

if the loading due to the input of the following transconductor is embedded into r_{o1} and r_{o2}. The phase lead ϕ_{o1} corresponds to positive resistance and lowers the Q value. The output resistance of the inverting transconductor r_{o2} connects directly in parallel with the rest of the circuit.

4.3 Non-Ideal Active Inductor

Combining the results from Section 4.2, we can write the equation for the input admittance of a non-ideal active inductor:

$$
\begin{aligned}
&Y_{in} = \frac{\dot{g}_{m1}\dot{g}_{m2}}{j\omega C_g} e^{j\Delta\phi} + {}^{1}\!\Big/\!_{r_{o2}}, \\
&\dot{g}_{m1} = \frac{g_{m1}}{\sqrt{1+\omega^2 r_{i1}^2 c_{i1}^2}\sqrt{1+{}^{1}\!\Big/\!_{\omega^2 r_{o1}^2 C_g^2}}}, \quad \dot{g}_{m2} = \frac{g_{m2}}{\sqrt{1+\omega^2 r_{i2}^2 c_{i2}^2}} \\
&\Delta\phi = \phi_{o1} - \phi_{i1} - \phi_{i2} = \arctan {}^{1}\!\Big/\!_{\omega r_{o1} C_g} - \arctan \omega r_{i1} c_{i1} - \arctan \omega r_{i2} c_{i2}
\end{aligned}
\tag{4.7}
$$

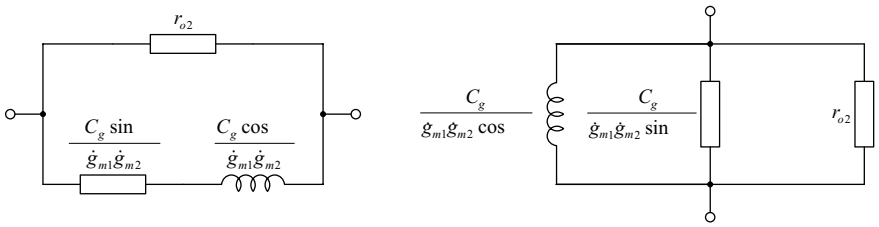

Figure 4.10 Series and parallel equivalent circuits of a non-ideal active inductor

The quality factor of the inductor becomes

$$
Q = \left[\tan\Delta\phi + \frac{\omega C_g}{\dot{g}_{m1}\dot{g}_{m2} r_{o2}} \sec\Delta\phi \right]^{-1} \tag{4.8}
$$

When used as an active resonator the circuit is connected in parallel with the resonating capacitor C_r. Then the resonance frequency and Q at resonance become

$$
\omega_0^2 = \frac{1}{LC_r} = \frac{\dot{g}_{m1}\dot{g}_{m2}}{C_g C_r}\cos\Delta\phi \quad \Rightarrow \quad Q_0 = \left[\tan\Delta\phi + \frac{1}{\omega_0 r_{o2} C_r} \right]^{-1} \tag{4.9}
$$

If we disregard the phase shift caused by the input connections of the transconductors (valid e.g. in MESFETs), and set $g_{m1} = g_{m2} = g_m$, $r_{o1} = r_{o2} = r_o = 1/g_o$, $C_g = C_r = C$, the resonance frequency can be written as

$$
\omega_0^2 = \frac{g_m^2 \cos\Delta\phi}{C^2\sqrt{1+{}^{1}\!\Big/\!_{\omega_0^2 r_o^2 C^2}}} = \frac{g_m^2}{C^2\left(1+{}^{1}\!\Big/\!_{\omega_0^2 r_o^2 C^2}\right)} \quad \Rightarrow \quad \omega_0 = \frac{g_o}{C}\sqrt{\left(\frac{g_m}{g_o}\right)^2 - 1} \tag{4.10}
$$

and the quality factor at ω_0 reduces to

$$
Q_0 = \frac{\omega_0 r_o C}{2} = \frac{1}{2}\sqrt{\left(\frac{g_m}{g_o}\right)^2 - 1} \approx \frac{g_m}{2g_o}, \quad \text{if } \frac{g_m}{g_o} >> 1 \tag{4.11}
$$

The same result is also obtained in [4.9] and [4.18]. If the g_m/g_o ratio is low, as in MESFETs, Q will become impractically low. In general, $1/\tan\Delta\phi$ is a very steep function at small arguments, and the quality factor of a gyrator-based active inductor collapses rapidly even if the net phase shift is only a few degrees. Ideally, it approaches infinity when

$$\Delta\phi \to -\arctan 1\Big/\omega_0 r_{o2} C_r \tag{4.12}$$

By Eq. (4.7), this requires that a phase-lagging RC-network exist at the input of either/both transconductors.

4.3.1 Non-Ideal Active Inductor Bandwidth

According to Eq. (4.7) and Figure 4.10, the series-mode inductance value of an active inductor is

$$L = \frac{C_g \cos\Delta\phi}{\dot{g}_{m1}\dot{g}_{m2}} = \frac{C_g}{g_{m1}g_{m2}}\left(1 - \omega^2 r_{i1}c_{i1}r_{i2}c_{i2} + \frac{r_{i1}c_{i1} + r_{i2}c_{i2}}{r_{o1}C_g}\right) \tag{4.13}$$

This implies that the positive inductance bandwidth of the circuit is

$$\omega_{L=0} = \frac{1}{r_i c_i}\sqrt{1 + \frac{2r_i c_i}{r_o C_g}} \approx \frac{1}{r_i c_i}, \quad r_o C_g >> r_i c_i \tag{4.14}$$

if $r_{i1} = r_{i2} = r_i$ and $c_{i1} = c_{i2} = c_i$. Thus, the input poles of the transconductors define the inductor bandwidth. Usually, however, the self-resonance frequency of the active inductor is lower than the inductance bandwidth, and it sets the limit of usability. The self-resonance circuit is formed by parasitic capacitance at the output, i.e. the output capacitance of one transconductor and roughly the input capacitance of the other.

$$\omega_{sr} \approx \sqrt{\frac{\dot{g}_{m1}\dot{g}_{m2}\cos\Delta\phi}{C_g(c_{o2} + c_{i1})}} \approx \frac{g_m}{C_g}, \quad C_g = c_{i1} >> c_{o2}, \quad g_{m1} = g_{m2} = g_m \tag{4.15}$$

4.3.2 Active Inductor High-Q Operation

The third and the most severe mechanism limiting the active inductor frequency range is its high-Q bandwidth. The parallel conductance of an active inductor is (Figure 4.10)

$$g_{tot} = g_{o2} + \frac{\dot{g}_{m1}\dot{g}_{m2}\sin\Delta\phi}{\omega C_g} \tag{4.16}$$

For simplicity, we assume that phase lag is present only at one transconductor input. Now we get after substitutions in Eq. (4.7)

$$g_{tot} = g_{o2} + \frac{g_{m1}g_{m2}r_{o1}\left(1 - \omega^2 r_i r_{o1} c_i C_g\right)}{\left(1 + \omega^2 r_i^2 c_i^2\right)\left(1 + \omega^2 r_{o1}^2 C_g^2\right)} \tag{4.17}$$

This function has a global minimum at ω_{Qmax}:

$$\frac{\partial g_{tot}}{\partial \omega} = 0 \quad \Rightarrow \quad \omega_{Q\max}^2 = \frac{1}{r_i r_{o1} c_i C_g}\left(1 + \frac{r_i c_i + r_{o1} C_g}{\sqrt{r_i c_i r_{o1} C_g}}\right) \tag{4.18}$$

The other requirement is that parallel conductance must become zero at this frequency. According to the condition given in Eq. (4.12)

$$\omega_{Q\max}^2 = \frac{r_i c_i + r_{o1} C_g + r_{o2} C_r}{r_i r_{o1} r_{o2} c_i C_g C_r} \tag{4.19}$$

With Eq. (4.18) and (4.19) combined, we finally get

$$\begin{aligned} r_i c_i r_{o1} C_g &= r_{o2}^2 C_r^2 \\ r_i c_i + r_{o1} C_g &= r_{o2} C_r \left(\omega_{Q\max}^2 r_{o2}^2 C_r^2 - 1\right) \end{aligned} \tag{4.20}$$

and further

$$\begin{aligned} r_i c_i &= \frac{r_{o2} C_r}{2}\left(\omega_{Q\max}^2 r_{o2}^2 C_r^2 - 1 \mp \sqrt{\left(\omega_{Q\max}^2 r_{o2}^2 C_r^2 - 1\right)^2 - 4}\right) \\ r_{o1} C_g &= \frac{r_{o2} C_r}{2}\left(\omega_{Q\max}^2 r_{o2}^2 C_r^2 - 1 \pm \sqrt{\left(\omega_{Q\max}^2 r_{o2}^2 C_r^2 - 1\right)^2 - 4}\right) \end{aligned} \tag{4.21}$$

Equation (4.21) fixes the transconductor input and output poles for infinite Q at ω_{Qmax}. The transconductor values must be appropriately chosen to set the resonance to this frequency (Eq.(4.9)). It is noteworthy to remark that it is not sufficient to adjust only the transconductor input RC-network for the maximum-Q frequency; the loss in conjunction with the gyrator capacitance must be adjustable as well. The minimum attainable high-Q frequency is square root of three times higher than the output pole frequency:

$$\omega_{\min} = \sqrt{3}/r_{o2} C_r \quad \Rightarrow \quad r_i c_i = r_{o1} C_g = r_{o2} C_r \tag{4.22}$$

Figure 4.11 is a graphical representation of Eq. (4.21) when $r_{o2}C_r$ is set to a typical value of 1 ns.

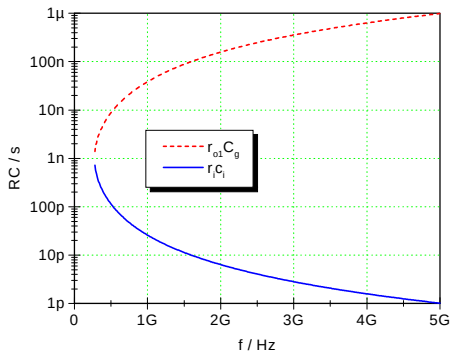

Figure 4.11 RC-products within a high-Q active inductor

Since the RC-products are highly non-linear functions of frequency, their linear adjusting does not move the high-Q region linearly. Therefore, it is generally unfeasible to get them track with a varying resonance frequency by e.g. adjustable resistors.

As an example, parameters for 1 GHz and 4 GHz given by the previous equations are tabulated in Table 4.1. The corresponding output conductances and Q-values are plotted in Figure 4.12.

	$r_i c_i$	C_g	r_{o1}	C_r	r_{o2}	$g_{m1} g_{m2}$
1 GHz	78,1 ps	4 pF	512 Ω	2 pF	200 Ω	$(19{,}5\ \mathrm{mS})^2$
4 GHz	19,5 ps	4 pF	128 Ω	0,5 pF	200 Ω	$(39{,}0\ \mathrm{mS})^2$

Table 4.1 Theoretical parameter values for active inductors

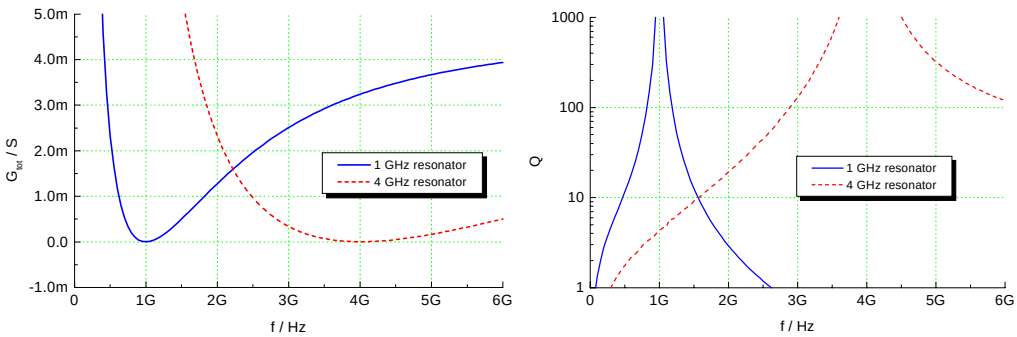

Figure 4.12 a) Output conductance and b) Q of 1 GHz and 4 GHz active inductors

As shown in Figure 4.12, the high-Q bandwidth of an active inductor is strongly dependent on frequency being much wider at high frequencies. The nearer the resonance frequency is to the minimum high-Q frequency the narrower and more sensitive the high-Q region is. Figure 4.13 shows how the high-Q bandwidth depends on the ratio $k = \omega_{Qmax} / \omega_{min}$.

As a rough approximation, the active inductor bandwidth of Q > 100 when $k = 2$ is three times wider than the minimum ($k = 1$), or five times wider when $k = 3$. Since the minimum high-Q frequency cannot be lowered limitlessly in practical integrated circuits, the operating frequency of a high-Q active inductor must be sufficiently high.

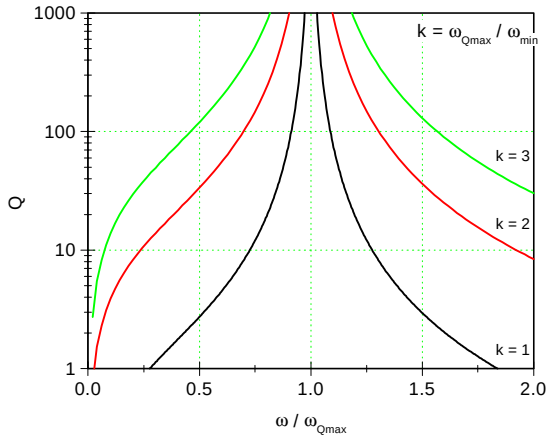

Figure 4.13 High-Q bandwidth of an active inductor

4.3.3 Controlling Resonance Frequency and Q

Effect of g_m

The resonance frequency of an active inductor resonator can easily be tuned by varying the transconductor values. As approximately applies

$$\omega_0 \sim \sqrt{g_{m1} g_{m2}} \tag{4.23}$$

the resonance frequency is directly proportional to the transconductor values if they are equal. Usually the transconductors are on the same bias line, which makes this requirement easy to fulfill remembering that transconductance is proportional to the DC current through the device.

According to Eq. (4.18), the position of the Q maximum is independent on the transconductance product. The high-Q frequency does not track with the shifting resonance frequency when the transconductors are tuned, which is naturally a serious drawback. The parallel conductance value is proportional to the transconductor product (Eq. (4.17)), and although the location of the conductance minimum (Q maximum) does not move, its value, together with the Q factor, will change the transconductors are tuned. This behavior is illustrated in Figure 4.14, where the upper curves correspond to lower transconductances and vice versa.

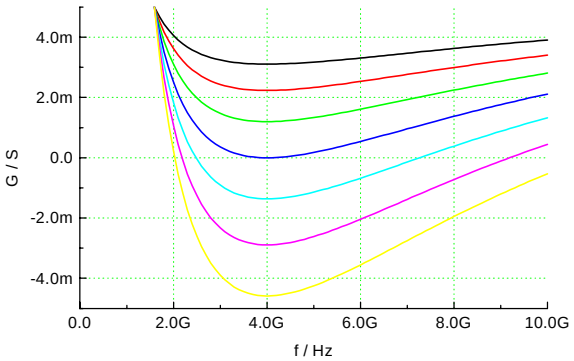

Figure 4.14 Conductance with changing g_m

One can see from Figure 4.14 that although the conductance minimum position remains unchanged, the zero-crossing frequency does change. It is indeed possible to design a high-Q resonator not for the conductance minimum but for the zero-crossing frequency. This frequency is defined by the magnitude of the parallel conductance which can be tuned e.g. with r_{o1} as well as with g_m. Since the resonance condition fixes inductance and the transconductors at each ω_0, tuning of r_{o1} remains the only practical way to adjust the Q value. The fact that conductance becomes negative on either side of the resonance frequency will make the definition of Q ambiguous, but will not result in instability provided that no parasitic LC-resonance is present within the region of negative conductance.

Effect of r_{o1}

As stated previously, also loss resistance r_{o1} in conjunction with the gyrator capacitance must be variable in addition to the transconductors, so that both inductance and loss can be optimized simultaneously. As seen from Eq. (4.18), the position of the Q maximum can be adjusted with r_{o1}. An equally effective alternative would be to tune the input resistance r_i, but it is more difficult to arrange in practice. The resistance r_{o1} also affects the magnitude of the parallel conductance (Eq. (4.17)) and unfortunately also the gyrator inductance, and hence the

resonance frequency (Eq. (4.13)). This brings up the problem of concurrent tuning: resonance frequency tuning and Q tuning cannot be performed separately. This sets great demands on the eventual automated tuning circuitry. The effect of changing r_{o1} on the net conductance of the gyrator is shown in Figure 4.15:

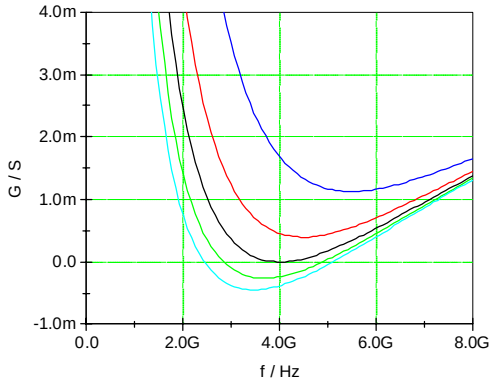

Figure 4.15 Conductance with changing r_{o1}

4.4 Active Inductor Noise

Noise is a very important issue in gyrator-based active inductors. The very nature of the gyrator with the gyration conductances implies that even in an ideal case the noise contribution from these resistive components cannot be avoided. It can be said that an electronic gyrator has a minimum noise production independent of the electronic design [4.19][4.20]. The additional noise contribution of the active devices can then be expressed with the coefficient γ, as previously.

When capacitors are connected at each port of a gyrator to form an active resonator, the gyrator noise sources remain the same, and the circuit can be represented as in Figure 4.16. Alternatively, the noise voltage sources at the inputs of the transconductors could be transferred into current sources at the outputs. When looking at the passive equivalent circuit of this configuration, we see that the noise source from g_{m1} can be expressed as a series voltage source in conjunction with the simulated inductance L. The other noise source forms a parallel current source for the resonating capacitor C, respectively. We can imagine that the active resonator susceptances become noisy in contrast to passive resonators where resistive components generate noise. As each susceptance at resonance is Q times larger than the loss conductance in a passive resonator, it can be concluded that the total noise of an active inductor resonator must be 2Q times that of a passive resonator with identical parameters [4.21].

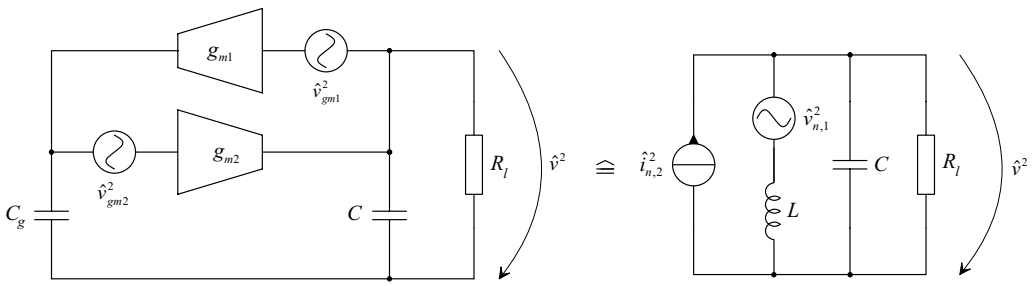

Figure 4.16 Active inductor resonator with noise sources and its passive equivalent circuit

The two noise components, the voltage source and the current source, can be formulated as

$$\hat{v}_{n,1}^2 = \hat{v}_{gm1}^2,\ \hat{i}_{n,2}^2 = g_{m2}^2 \hat{v}_{gm2}^2 \tag{4.24}$$

where v_{gm1} and v_{gm2} are the equivalent input noise voltages of the transconductors. The total noise voltage spectral density over the resonator becomes

$$\hat{v}^2 = \frac{\hat{v}_{gm1}^2 + \omega^2 L^2 g_{m2}^2 \hat{v}_{gm2}^2}{\omega^2 L^2 G_l^2 + (\omega^2 LC - 1)^2} \tag{4.25}$$

At the center frequency this yields

$$\hat{v}^2\Big|_{\omega_0} = Q_l^2 \left(\hat{v}_{gm1}^2 + g_{m2}^2 \omega_0^2 L^2 \hat{v}_{gm2}^2 \right) \tag{4.26}$$

In high-frequency circuits the transconductors are usually realized as single transistors, and using the transistor input noise approximation $4kT\gamma g_m$, we get the final form:

$$\hat{v}^2\Big|_{\omega_0} = 4kT\gamma \frac{Q_l^2}{g_{m1}} \left(1 + \frac{C_g}{C} \right) = 4kT\gamma Q_l^2 \left(\frac{1}{g_{m1}} + \frac{g_{m2}}{\omega_0^2 C^2} \right) \tag{4.27}$$

This shows again the relation between the high loaded quality factor and high noise. Obviously, maximized g_{m1} and minimized g_{m2} result in lowest noise, but due to practical limitations, they cannot usually be chosen optimally.

The total rms noise of an active inductor resonator can be obtained from Eq. (4.25) by integration:

$$\overline{v}^2 = \frac{\hat{v}_{gm1}^2}{2\pi} \omega_0 \int_0^\infty \frac{d\omega}{\omega^2 L^2 G_l^2 + \left(\omega^2 LC - 1\right)^2} + \frac{g_{m2}^2 \hat{v}_{gm2}^2}{2\pi} \int_0^\infty \frac{\omega^2 L^2 d\omega}{\omega^2 L^2 G_l^2 + \left(\omega^2 LC - 1\right)^2} \tag{4.28}$$

With the previous assumptions, this becomes

$$\overline{v}^2 = \frac{kT\gamma}{C} Q_l \sqrt{\frac{g_{m2}}{g_{m1}}} \left(\sqrt{\frac{C_g}{C}} + \sqrt{\frac{C}{C_g}} \right) = \frac{kT\gamma}{C} Q_l \frac{\omega_0}{g_{m1}} \left(C_g + C \right) \tag{4.29}$$

In a simplified case where $g_{m1} = g_{m2}$ and $C_g = C$, this yields

$$\overline{v}^2 = \frac{2kT\gamma}{C} Q_l \tag{4.30}$$

which is in good agreement with the calculations in [4.19] and [4.21].

At this point it is interesting to see how the active inductor resonator noise compares to that of negative resistor resonators. From Eq. (4.27) we can identify the effective noise resistance R which can be associated with that of the passive inductor $R = R_s(1+r_n,g_n)$ in a negative resistance resonator [Section 3.5.1]. Thus, it is possible to define 'the effective unloaded noise quality factor' for a gyrator resonator, which shows what would be the magnitude of Q_0 in the passive inductor inducing the same amount of noise as an active inductor. It becomes

$$Q_{0,noise} = \frac{\omega_0 (1 + r_n, g_n)}{\gamma g_{m2} \left(\frac{1}{C} + \frac{1}{C_g} \right)} \tag{4.31}$$

With realistic parameters $Q_{0,noise}$ is very low, typically less than one. Therefore, it is reasonable to draw the conclusion that active inductor resonators are always clearly inferior to negative resistor resonators in terms of noise performance.

The noise calculations here are very much idealized, and they do not account for additional noise from Q-enhancing phase-shift circuits or their frequency-dependence. Nevertheless, they do show the effect of the main parameters to be dimensioned and give a suitable basis for comparisons. These results can even be extended to g_m-C filters constructed from integrators instead of gyrators, since the signal paths of the g_m-C biquadratic filters reduce to those of gyrator filters [4.21]. Hence, the inherent noise behavior is similar.

4.5 Active Inductor Distortion

4.5.1 Introduction

The non-linearities in the transconductors give rise to distortion effects in gyrator-based active inductors. Similarly as in negative resistors, compression will cause increasing loss at the fundamental frequency and thus degradation of Q. As active inductors are primarily supposed to affect the phase characteristics of the resonator, the phase behavior at compression must also be examined.

The Volterra-series method is also applicable for gyrators with the same conditions as discussed in Section 3.6. Although very much simplified, the non-linear transconductor (or transistor) model used here is the same as in negative resistor calculations. In spite of the fact that realistic active inductors suffer from much more complicated distortion mechanisms than presented here, the calculations give insight on how the dimensioning of the essential circuit parameters contribute to the distortion performance, at least in qualitative terms.

The large-signal inductance of an active inductor can be expressed in the similar way as the large-signal conductance of a negative resistor. Its reactance can be referred as the imaginary part of the describing function:

$$\omega L = \frac{\textit{stimulus voltage } v_{in}}{\mathrm{Im}\{\textit{fundamental response current}\}} \tag{4.32}$$

The change in the response current, and thus in the inductance, at the fundamental frequency with increasing input voltage can be described with the *-1-dB inductance compression* of the circuit. The −1-dB (or 10.9%) inductance change will shift the resonance frequency approximately 6% upwards, which is in most cases unacceptable and must somehow be compensated in potential applications.

Even if the gyrator-based active inductor is lossless in the small-signal approximation, the non-linear effects will introduce loss conductance at higher input voltage levels, resulting in a reduction of the circuit quality factor. Just like in negative resistors, this can be accounted for by examining the real part of the fundamental response current.

4.5.2 Volterra Kernels

Figure 4.17 depicts an active inductor with non-linear transconductors. The transconductor i_1 becomes non-inverting, when the polarity of its controlling voltage is inverted. This affects only odd-order terms in the current expression. For mathematical reasons, a conductance G_g must be added in parallel with the gyrator capacitor C_g, otherwise some distortion components become infinite in theory.

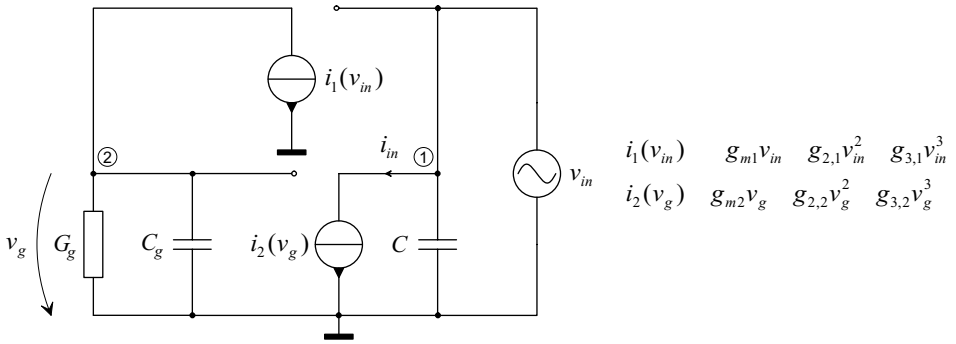

Figure 4.17 Gyrator resonator with non-linear transconductors

Following the same procedure as previously with negative resistors, we can calculate the first-order Volterra kernels for the gyrator inductor. When the excitation voltage is set to unity, we get

$$H_{1,2}(j\omega) = \frac{g_{m1}}{G_g + j\omega C_g}, \quad H_{iin,1}(j\omega) = \frac{g_{m1}g_{m2}}{G_g + j\omega C_g} \tag{4.33}$$

The second-order Volterra kernels become respectively:

$$\begin{aligned} H_{2,2}(j\omega_1, j\omega_2) &= \frac{-i_{NL2,1}}{G_g + (j\omega_1 + j\omega_2)C_g} \\ H_{iin,2}(j\omega_1, j\omega_2) &= \frac{-i_{NL2,1}g_{m2}}{G_g + (j\omega_1 + j\omega_2)C_g} + i_{NL2,2} \end{aligned} \tag{4.34}$$

where the non-linear currents are

$$\begin{aligned} i_{NL2,1} &= g_{2,1} \\ i_{NL2,2} &= \frac{g_{2,2}g_{m1}^2}{(G_g + j\omega_1 C_g)(G_g + j\omega_2 C_g)} \end{aligned} \tag{4.35}$$

Finally, the expressions for the third-order Volterra kernels are

$$\begin{aligned} H_{3,2}(j\omega_1, j\omega_2, j\omega_3) &= \frac{i_{NL3,1}}{G_g + (j\omega_1 + j\omega_2 + j\omega_3)C_g} \\ H_{iin,3}(j\omega_1, j\omega_2, j\omega_3) &= \frac{i_{NL3,1}g_{m2}}{G_g + (j\omega_1 + j\omega_2 + j\omega_3)C_g} + i_{NL3,2} \end{aligned} \tag{4.36}$$

The third-order non-linear current sources for each type of non-linear response are as follows:

$$\begin{aligned}
i_{NL3,1} &= g_{3,1} \\
i_{NL3,2} &= \frac{g_{3,2}g_{m1}^3}{(G_g + j\omega C_g)^3} - \frac{2g_{2,2}g_{2,1}g_{m1}}{(G_g + 2j\omega C_g)(G_g + j\omega C_g)} && \text{HD}_3 \\
i_{NL3,2} &= \frac{g_{3,2}g_{m1}^3}{(G_g + j\omega C_g)(G_g^2 + \omega^2 C_g^2)} && \text{IM}_3, \text{COMP} \\
&\quad - \frac{2g_{2,2}g_{2,1}g_{m1}}{3}\left[\frac{1}{(G_g + 2j\omega C_g)(G_g - j\omega C_g)} + \frac{2}{G_g(G_g + j\omega C_g)}\right] && (\omega_1 \approx \omega_2)
\end{aligned} \tag{4.37}$$

In high-Q inductors $G_g << \omega C_g$, and therefore the kernel expressions can be considerably simplified. For instance, Eq. (4.37) is approximated as

$$\begin{aligned}
i_{NL3,1} &= g_{3,1} \\
i_{NL3,2} &= -\frac{g_{3,2}g_{m1}^3}{j\omega^3 C_g^3} + \frac{g_{2,2}g_{2,1}g_{m1}}{\omega^2 C_g^2} && \text{HD}_3 \\
i_{NL3,2} &= \frac{g_{3,2}g_{m1}^3}{j\omega^3 C_g^3} - \frac{2g_{2,2}g_{2,1}g_{m1}}{3}\left[\frac{1}{2\omega^2 C_g^2} + \frac{2}{j\omega C_g G_g}\right] && \text{IM}_3, \text{COMP}
\end{aligned} \tag{4.38}$$

4.5.3 Distortion Components

Utilizing Table 3.1, we can now identify each distortion component in interest. The expressions are gathered in Table 3.5 in which G_g is omitted where possible. We can see that when G_g is very small the expression for the compression response becomes dominated by the last large imaginary term. Hence, the dominant compression mechanism in high-Q active inductors is the inductance compression. Obviously, if the second-order non-linearities in the active devices were minimized the problem would be alleviated. Differential transconductors with suppressed even-order non-linearities can be used for this purpose. In addition, the real part of the compression response, which is responsible for Q degradation, would be minimized in differential configurations.

Compressing inductance and the resulting shift of resonance have a reductive effect on Q in practical active inductors, since the phase shifting circuitry necessary for high-Q operation is narrow-banded without exception. The Q maximum is therefore sharp and more or less constant in frequency. As the resonance frequency is deviated from this point, the circuit Q will drop quickly, although the input signal level is not yet high enough for the actual conductance compression to show up.

The -1-dB inductance compression point can mark the upper limit of the active inductor dynamic range. As the total imaginary input current at the fundamental frequency is

$$i_{in} \approx v_{in}\frac{g_{m1}g_{m2}}{j\omega C_g} - v_{in}^3\frac{g_{2,1}g_{2,2}g_{m1}}{j\omega C_g G_g} \tag{4.39}$$

the circuit can be represented by two parallel inductors, and the condition for -1-dB/10.9% compression is

Type of response	Response i_{in}
fundamental	$v_{in}\dfrac{g_{m1}g_{m2}}{j\omega C_g}$
second harmonic	$-\dfrac{v_{in}^2}{2}\left(\dfrac{g_{2,1}g_{m2}}{2\,j\omega C_g}+\dfrac{g_{2,2}g_{m1}^2}{\omega^2 C_g^2}\right)$
third harmonic	$\dfrac{v_{in}^3}{4}\left(\dfrac{g_{3,1}g_{m2}}{3\,j\omega C_g}-\dfrac{g_{3,2}g_{m1}^3}{j\omega^3 C_g^3}+\dfrac{g_{2,1}g_{2,2}g_{m1}}{\omega^2 C_g^2}\right)$
compression ($g_3 < 0$)	$\dfrac{3v_{in}^3}{4}\left(\dfrac{g_{3,1}g_{m2}}{j\omega C_g}+\dfrac{g_{3,2}g_{m1}^3}{j\omega^3 C_g^3}-\dfrac{2g_{2,1}g_{2,2}g_{m1}}{3}\left(\dfrac{1}{2\omega^2 C_g^2}+\dfrac{2}{j\omega C_g G_g}\right)\right)$

Table 4.2 Harmonic distortion components for the gyrator-based active inductor

$$\frac{-L_{comp}}{L_{fund}}=\frac{G_g g_{m2}}{v_{in,comp}^2 g_{2,1}g_{2,2}}=\frac{\omega_0 C_g g_{m2}}{v_{in,comp}^2 g_{2,1}g_{2,2}Q_{0,actind}}=10.9\% \tag{4.40}$$

where $Q_{0,actind} = \omega_0 C_g/G_g$ is the unloaded quality factor of the active inductor. The compression point is

$$v_{in,comp}^2 \approx 9.17\frac{\omega_0 C_g g_{m2}}{g_{2,1}g_{2,2}Q_{0,actind}} \tag{4.41}$$

At very high Q values the theoretical compression point approaches zero, or in other words, the input current goes to infinity. This is naturally impossible in practical circuit realizations, where the biasing and other auxiliary circuits limit the current swing. Therefore, even when the active inductor is trimmed to be completely lossless, its compression voltage is non-zero, though small.

4.5.4 Dynamic Range

Now that both the noise and compression characteristics are known we can determine the theoretical dynamic range of a gyrator-based active resonator. It is assumed that the unloaded Q of the active inductor is high enough not to increase the noise level substantially.

When an active inductor forms a parallel resonator with a capacitor *C*, the fundamental response current of the resonator becomes zero at resonance. Following the same procedure as with negative resistors, the condition for the total resonator current compression is

$$\frac{G_l v_{in,comp}-\left|i_{in}(compression)\right|}{G_l v_{in,comp}}=89.1\% \quad\Rightarrow\quad \frac{\left|i_{in}(compression)\right|}{G_l v_{in,comp}}=10.9\% \tag{4.42}$$

Combining Equations (4.40) and (4.42), we can write:

$$\frac{\left|\left\{i_{in,actind}(comp)(v_{in,comp,actind})\right\}\right|}{v_{in,comp,actind}}\omega_0 L=\frac{\left|\left\{i_{in,actind}(comp)(v_{in,comp,reson})\right\}\right|}{v_{in,comp,reson}\omega_0 C}Q_l \tag{4.43}$$

The third-order compression terms are proportional to v^3, and after cancellation we finally get

$$v_{in,comp,reson}^2 = \frac{v_{in,comp,actind}^2}{Q_l} \tag{4.44}$$

The result connects the compression voltages of active inductor resonators with those of bare active inductors. It is shown in [4.21]-[4.24] that the same expression applies to any OTA-C resonator/filter, regardless of the used topology. In the context of this thesis, it is very important to note that the compression point of an active inductor resonator is Q_0 times lower than that of a negative resistor resonator, if the maximum voltages for the active circuits are equal. Here, Q_0 refers to the unloaded quality factor of the compensated passive LC resonator.

By Eqs (4.29) and (4.44), we can be directly write the equation for the dynamic range of an active inductor resonator:

$$DR = 10\log\frac{9.17}{Q_l^2}\frac{g_{m1}g_{m2}C}{kT\gamma\left(1+C/C_g\right)g_{2,1}g_{2,2}Q_{0,actind}} \tag{4.45}$$

Compared to negative resistor resonators, the dynamic range is Q_0^2 times lower, provided again that the active circuit compression points are equal. Thus, even with LC quality factors as low as 10, the degradation in the dynamic range is substantial (20 dB).

To get a comparable view on the magnitude of the active inductor dynamic range, we substitute the numerical parameter values used in Section 3.7.4 in the equation:

ω_0 = 4 GHz , Q_l = 100
simulated L = 2 nH, Q_0 = 1000
C_g = 0.2 pF, C = 0.79 pF
$g_{m1,2}$ = 10 mS, $g_{2,1} = g_{2,2}$ = 2 mA/V^2, $g_{3,1} = g_{3,2}$ = -200 µA/V^3 (TriQuint MESFET 4 × 16 µm)

With these parameter values Eq. (4.45) gives $DR \approx 31$ dB which is even in this idealized case clearly lower than those of negative resistor resonators [Section 3.7.4].

	rms noise voltage / µV	**compression voltage / dBmV**	**dynamic range / dB**
Active inductor resonator	917	31	31

Table 4.3 Computational noise voltage, compression point and dynamic range for the active inductor resonator

In practical active inductor resonators, Q enhancement in the form of phase shifters is always needed for an high unloaded Q. As these are strongly frequency-dependent and usually narrow-banded, they have effect on the noise transfer functions. Moreover, regardless of the construction, they will inject excess noise into the circuit. These factors unaccounted here will change the noise characteristics of active inductors and so diminish the available dynamic range.

The phase shifting network often includes active components that introduce additional distortion sources. The gyrator port where the gyrator capacitor C_g is connected is subject to higher voltage swings than the input port, as the gyrator capacitor is usually smaller than the resonating capacitor C. This intensifies the effect of the phase shifter non-linearity. Additional reduction of dynamic range due to these elements is substantial in realistic circuits.

The input capacitances of the transconductors are included in both C_g and C, often dominating the former. As these are non-linear, they will manifest themselves as increased distortion in the circuit. If the circuit is designed in such a way that most of capacitance comes from passive capacitors, not from the transconductors, this distortion contribution is smaller. If

the non-linear capacitances had been taken into account in the Volterra kernel calculations, they would have made the expressions too complicated and unillustrative for the scope of this study.

There is reason to underline again that the figures presented are results of very much simplified analyses, and therefore not attainable in practice. However, they give good grounds for judging the performance of each topology and dimensioning the essential circuit parameters, and show the order of magnitude of the non-ideal effects. In spite of their favorable properties in terms of practical integration (no need for area-consuming and low-quality passive inductors), the gyrator-based active resonators are less attractive alternatives for high-frequency active filters than the negative resistor resonators.

4.6 Practical Active Inductors

Several realized active inductors and resonators for microwave frequencies are presented in this section. They all share the same basic structure based on a gyrator, i.e. they include an inverting and a non-inverting transconductor without exception. The most important properties of the circuits are explained and techniques for increasing their Q value are discussed.

4.6.1 Hara's Circuits and Its Derivatives

The new possibilities of MMIC integration brought up the idea of active inductance simulation with MESFETs in the late 1980's, when extensive work for developing high-performance integrated active inductors was made by Hara et al. [4.12][4.13]. Their first realization employs simply a resistor as the non-inverting transconductor. The gyrator capacitance is formed solely by the gate-source capacitance of the transistor.

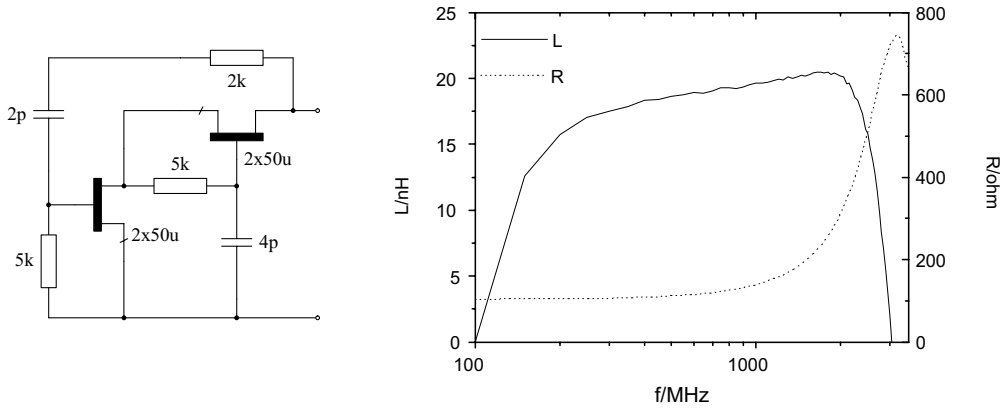

Figure 4.18 a) Hara's first generation active inductor realized with the GMMT-F20 process; b) Measured inductance and series resistance [4.25]

The circuit approximates a series-connection of an inductor and a resistor:

$$L \approx \frac{C_{gs}}{g_m^2} + \frac{C_{gs}}{g_m G_{FB}}, \quad R_s \approx \frac{1}{g_m} \tag{4.46}$$

As the feedback resistor simulates badly a transconductor, Hara's first-generation inductor is inherently lossy and therefore not a prospective candidate for filter design.

Hara's second generation topology shown in Figure 4.19a has better performance as the non-inverting transconductor is realized with a common-gate transistor. A somewhat different approach is presented by Zhang et al. [4.26]. By employing the theory of second-generation

current conveyors (CCII), they have managed to develop a floating active inductor. The theoretical performance is, however, actually similar to the inductor of Hara et al.

Unfortunately, the properties of these circuits have been calculated by approximating the transistors with the gate-to-source capacitance C_{gs} and the transconductance g_m only. However, the drain-to-source conductance g_{ds} of the real transistor is a crucial parameter when evaluating active inductor circuits. When this element is added to the transistor models, the performance degrades rapidly, since it is connected directly across the output as parallel conductance. Regrettably, the theoretical calculations tend to become more complicated and simplifications are necessary.

The limited g_{ds} of a GaAs MESFET was first taken into account in [4.25]. Two new active inductor circuit configurations were presented, and the crucial parameter g_{ds} was held in theoretical examinations all the time. The topologies were found by a systematic search from the group of potential feedback configurations. The circuits combined in a single schematic drawing are shown in Figure 4.19b.

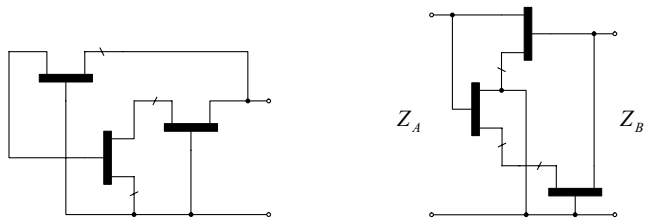

Figure 4.19 a) Hara's second-generation active inductor; b) Alinikula's active inductor

The circuit in Figure 4.19a is practically lossless at low frequencies only in the ideal case. The addition of g_{ds} clearly worsens the characteristics by lowering the equivalent parallel resistance (Figure 4.20).

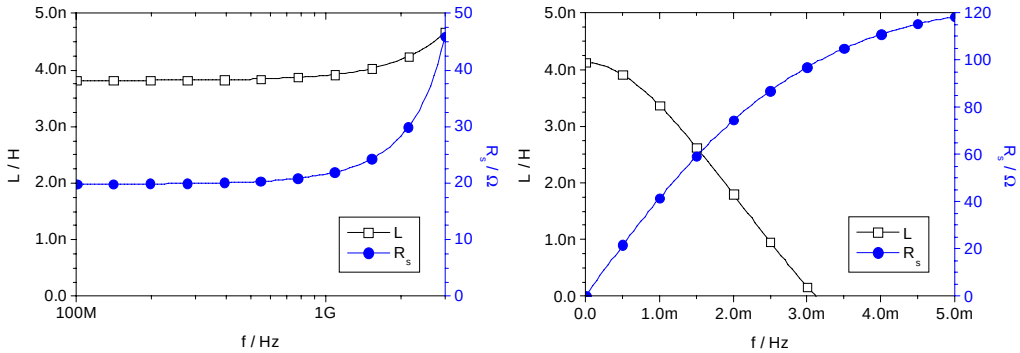

Figure 4.20 a) L and R vs. frequency (Hara); b) L and R vs. g_{ds}, f=1 GHz (Hara); g_{m1}, g_{m2}, g_{m3} = 5 mS, g_{ds1},g_{ds2},g_{ds3} = 500 μS and C_{gs1},C_{gs2},C_{gs3} = 0.1 pF

The calculations and the simulations were made on the assumption that all the active elements in the circuits considered are of equal size. This is by no means the optimal dimensioning for the best achievable performance, but considerably simplifies the practical implementation. It allows the transistors to be placed in series with the same drain current and makes simple gate biasing possible. These are all favorable aspects in integrated circuit design.

In normal FET processes the ratio g_m/g_{ds} can be as low as 10. Thus, this unpleasant property almost solely dictates the performance, while the benefits of the possibly high f_T are few. The only way to improve the results is to use another technology or to reduce the effect of g_{ds}. The latter can be done with a circuit topology shown in Figure 4.21a [4.14] – [4.17]. When

approximating the performance without g_{ds}, the proposed circuit is found to be more lossy at some frequencies than the circuit suggested by Hara et al. However, the performance of this circuit is less dependent on g_{ds}.

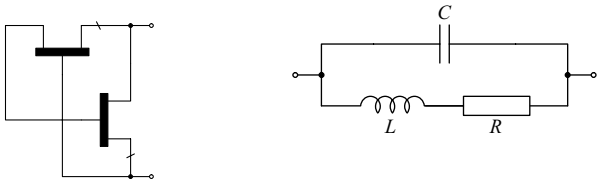

Figure 4.21 a) Principle of the active inductor circuit by the author;
b) Equivalent circuit of the active inductor, g_{ds} ignored

The theoretical performance of the proposed circuit in the ideal case ($g_{ds} = 0$) can be easily calculated: its inductance, series resistance and parallel capacitance become

$$L = \frac{C_{gs}}{\omega^2 C_{gs}^2 + g_m^2}, \quad R = \frac{\omega^2 C_{gs}^2}{g_m(\omega^2 C_{gs}^2 + g_m^2)}, \quad C = C_{gs} \tag{4.47}$$

These calculated quantities correspond to the equivalent circuit components in Figure 4.21b.

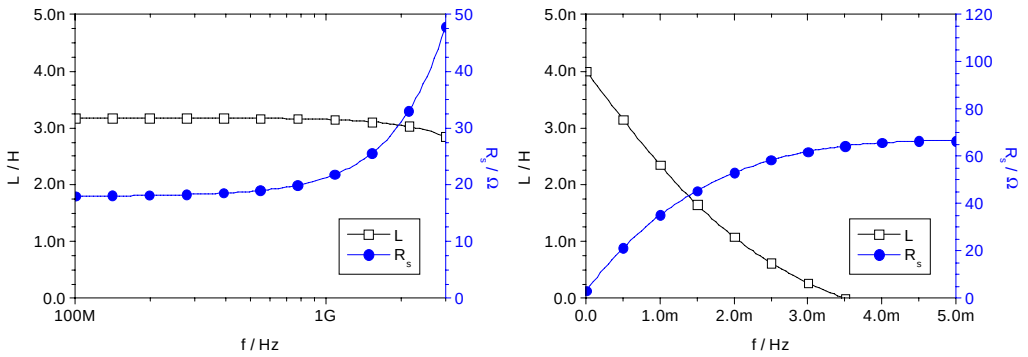

Figure 4.22 a) L and R_s vs. frequency (author); b) L and R_s vs. g_{ds}, f = 1 GHz

The simulated results are illustrated graphically in Figure 4.22. As the frequency grows the losses rise more rapidly than in the previous case, while the inductance is rather constant. The parameter values remain the same as in Figure 4.20. If the results in Figure 4.22b are compared with those in Figure 4.20b, one can remark that now g_{ds} has obviously less effect on the performance, especially when it is large.

When g_{ds} is added to the transistor models the equations become

$$L = C_{gs}\left[g_m^2\left(1 - \frac{g_{ds}^2}{g_m^2}\right)\right]^{-1}, \quad R_s = \left[g_m\left(\frac{g_m}{g_{ds}} - \frac{g_{ds}}{g_m}\right)\right]^{-1}, \quad R_p = \left[g_m\left(2\frac{g_{ds}}{g_m} + 1\right)\right]^{-1}, \quad C = C_{gs} \tag{4.48}$$

The equations (4.48) and the corresponding equivalent circuit in Figure 4.23 include a parallel and a series resistor in order to show the effect of the g_m/g_{ds} ratio.

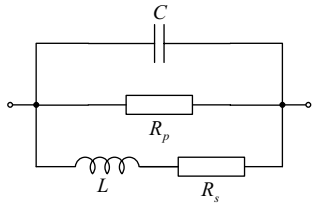

Figure 4.23 Equivalent circuit of the active inductor with g_{ds}

In addition to the previous one, the suggested topology has a few other benefits: above all its simplicity and compatibility with processes. However, it should be noted that the absolute value of inductance is rather low, mainly due to the non-scaled transistors. In test structures, much higher values can be achieved with scaled transistors and separate biasing. Another way to increase inductance is to add a gyrator capacitor to the gate of the lower transistor at the cost of diminished bandwidth.

The reason why the proposed active inductor topology gives better results when g_{ds} is taken into account, lies in the fact that the non-inverting common-gate transistor has a low input impedance compared to the output impedance of the inverting common-source transistor. Therefore, the former loads the latter considerably causing performance degradation. The cascode connection for the inverting transconductor used by Hara et al. has approximately twice the output impedance of a single transistor, and hence the loading effect is emphasized in Hara's circuits.

Practical implementations of active inductors suffer from degraded performance comparing to the ideal case. The existence of the Miller capacitance C_{gd} in the transistors affects the frequency characteristics of the circuit. The coupling capacitors limit the lowest usable frequency and increase the series resistance, not to mention the space on the chip they require. The RF decoupling of the bias line by means of active loads clearly raises the losses, too.

The active inductor circuit was first tested as a part of a simple LC-filter processed by the GEC-Marconi foundry [4.16][4.17]. The process was GEC-Marconi F20 with a 0.5-μm channel length and a 20-GHz f_T. The low performance of the filter could easily be noticed. This was due to the low Q-value of the inductors, which is unavoidable in normal high-g_{ds} GaAs active inductor structures.

4.6.2 Bipolar Active Inductors

The g_m/g_{ds} ratio is the most important factor contributing to the small-signal performance of an active inductor. In FET processes, this parameter is unavoidably small, while in bipolar processes it can be several thousands. This gives a strong motivation to use bipolar transistors instead of FETs. The limited β of the bipolar transistor causes some deviation but being normally in the range of 100 it has almost no effect whatsoever.

A more significant effect results from the base-spreading resistance of the bipolar transistor. The series resistance of the bipolar active inductor tends to make a dip at a certain frequency, as shown in Figure 4.24b. If required, this feature can partly be eliminated by keeping the base resistance as low as possible, that is, by choosing an appropriate transistor structure. Proper structures commonly have multiple base contacts and a long stripe-shaped emitter region. The base resistance also affects the inductance value, worsening the flatness of the frequency response but also increasing the highest achievable value. In fact, the inductance in the low-loss frequency region can be called 'super-inductance' with the reactance value of $X = \omega^2 L_{super}$. This dispersive effect can be advantageous in filter design, as it virtually increases the number of poles and thus makes the response steeper.

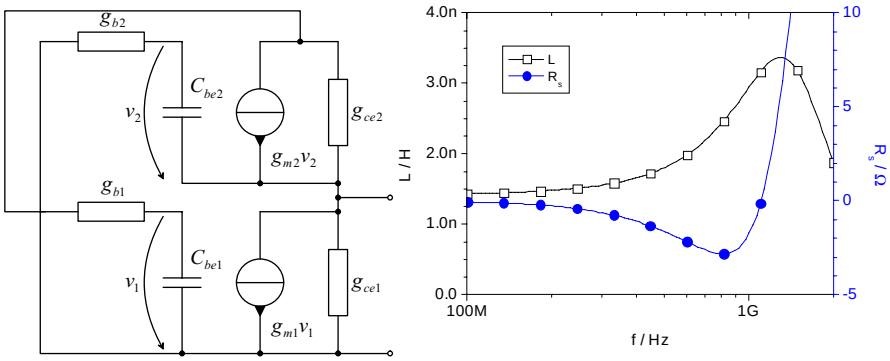

Figure 4.24 a) Small-signal representation of a bipolar active inductor;
b) L and R_s vs. frequency, g_{m1}, g_{m2} = 75 mS, g_{ce1}, g_{ce2} = 100 μS, g_{b1}, g_{b2} = 33 mS and C_{be1}, C_{be2} = 8 pF

The resistance dip is well predicted by the theoretical studies in Section 4.3. In fact, the base resistance of the bipolar transistor together with its base-emitter capacitance forms a phase-shifting network described earlier. Hence, this Q-enhancing quality is inherent in bipolar active inductors, even to such an extent that instability may become a serious problem. It must be noted that in real circuits there are more loss-generating mechanisms, such as biasing, which affect the depth of the resistance dip.

The large g_m of the BJT reduces the inductance value, but at the same time the bigger C_{be} compensates this change. The larger g_m also facilitates the AC-coupling: the coupling capacitors need not be as large as in MESFET circuits with the same amount of phase compensation.

A major advantage of the bipolar active inductor is its low power consumption. Compared to the MESFET inductors, only a fraction of the operating current is needed to achieve adequate performance. This should be a welcomed feature in low-power applications.

4.6.3 Q-Enhancement

The fall of the inductor series resistance in bipolar circuits is primarily due to the base resistance of the upper feedback transistor. If this resistance can be kept low, the minimum value and the corresponding frequency of the series resistance dip can be controlled with an additional resistor connected to the base of the feedback transistor. Thus, it is possible to increase the Q value at a certain narrow frequency band. Applied to FET-based circuits, this technique is particularly useful, since FETs lack sufficiently large gate resistances. The inherently high losses of MESFET-based inductors can be cancelled within a certain frequency band in this way.

Basically, Q enhancing is based on a phase-lagging network in the transistor inputs [Section 4.3]. Two different methods for phase compensation have been used: phase shift with an ordinary RC-network [4.27][4.28], or phase shift within the positive transconductor as a form of gate resistance in the common-gate FET, as described earlier [4.16][4.17][4.28]. RC-networks are uncomplicated to design and realize, but they tend to become quite narrow-banded and difficult to adjust externally. A single RC-stage gives a phase compensation of

$$\Delta\phi = -\arctan \omega RC \tag{4.49}$$

Since the phase error of a practical active inductor varies along with process variations and tuning, the phase compensation circuit must be adaptive. This can be implemented with variable resistors (e.g. triode-connected FETs) or variable capacitors (varactor diodes).

If a resistor R_{Qen} is connected at the gate of the common-gate transistor, the additional phase shift across the transistor becomes

$$\Delta\phi_c = -\arctan \omega R_{Qen} C_{gs} \tag{4.50}$$

This gives an alternative way of phase compensation, although the basic operation is the same as in RC-networks. This scheme employs only one additional resistor, fixed or adjustable, without bulky capacitors, and is therefore compact.

4.6.4 Realized MESFET Active Inductors

A GaAs-MESFET active inductor circuit utilizing the Q-enhancing resistor technique is shown in Figure 4.25. The controlling resistance is realized with a MESFET operating in the triode region. The equivalent series resistance value, and thus the location of the Q-maximum, can be controlled by the external DC voltage $V_{bias,Q}$ applied to the gate of this device. As shown in the theoretical discussions in Section 4.3, the loss resistance in conjunction with the gyrator port 2 must be variable, too. This adjustment can be made by controlling the topmost RF-decoupling MESFET with another external voltage $V_{bias,f}$. In this circuit, the transconductances of the active devices were chosen to be constant, and the voltage $V_{bias,f}$ also controls the inductance value. The measured inductance and Q-value of the circuit at the Q-maximum are plotted in Figure 4.26.

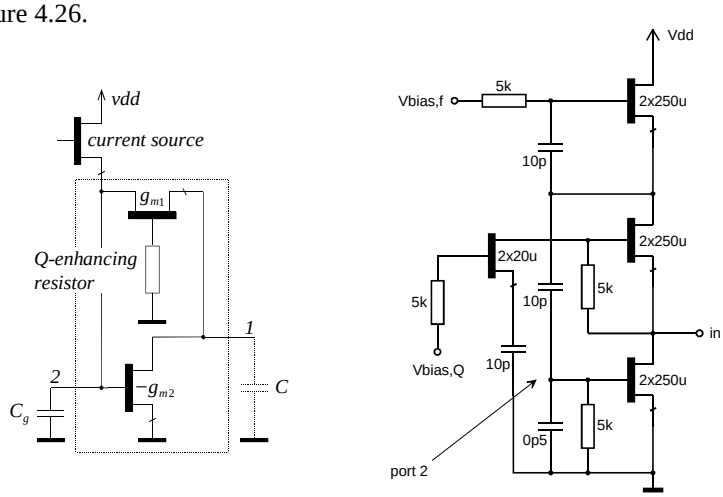

Figure 4.25 a) Principle of the Q-enhancing resistance; b) MESFET active inductor with Q-enhancing resistance, processed with GEC-Marconi F20

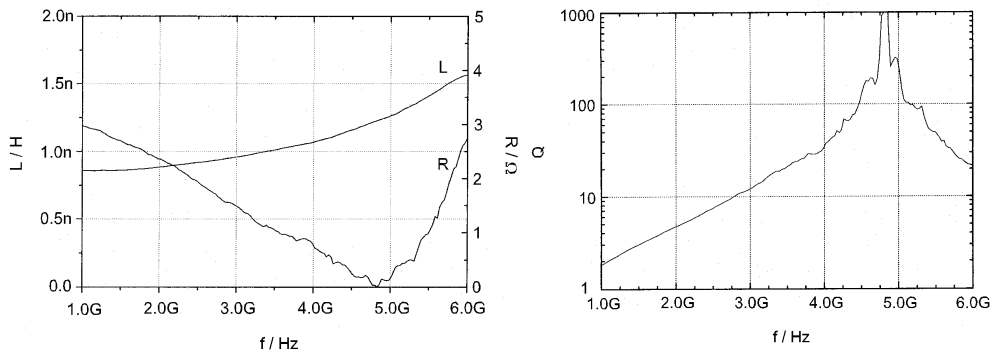

Figure 4.26 a) Measured inductance and resistance of the MESFET active inductor; b) Measured unloaded Q of the MESFET active inductor

Simulated MESFET active inductors utilizing the other type of phase shifter, i.e. a normal RC network, has been reported in [4.27] and [4.28] for demonstration purposes only. Two different resonator topologies have been taken into inspection. The first one in Figure 4.27a employs a modified differential pair as the non-inverting transconductor. The benefit of this structure is that now the non-inverting stage is a common-drain – common-gate combination with high input impedance. Therefore, loading at the inverting transconductor output, and the sensitivity to g_m/g_{ds}, is smaller. The transconductance values in this topology are always smaller than in single-device transconductors, resulting in higher inductance values. This makes its utilization in resonators rather difficult, as the resonating capacitor becomes very small.

The second active resonator topology in Figure 4.27b is a variation of the previous circuit in Figure 4.25. The phase compensation for high-Q operation is realized using both methods: a Q-enhancing resistor at the gate of the common-gate MESFET and an additional RC network at the inverting stage input. Two phase shifters were needed, as the transconductances of the devices were small in the used process (the low-power, low-threshold voltage GEC-Marconi L20).

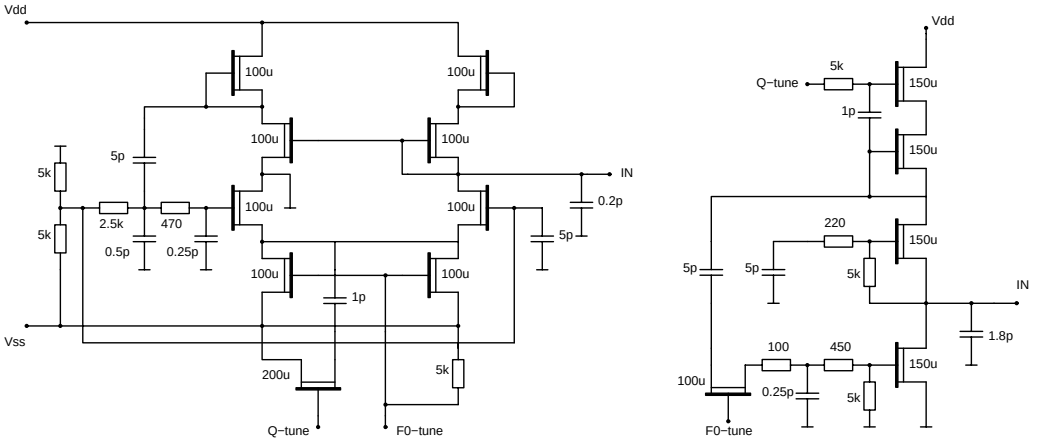

Figure 4.27 Active inductor resonators with RC phase shifters

The simulated S_{11} of both resonators are shown in Figure 4.28. The total power consumptions became 49 mW and 70 mW, respectively. Less transconductance is needed for high-Q operation in the differential-based active inductor resonator, and thus its power consumption is lower.

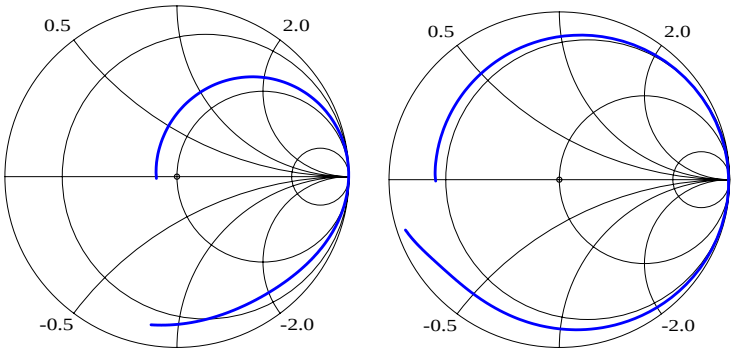

Figure 4.28 Simulated S_{11} of the two active resonators

4.6.5 Realized Bipolar Active Inductors

As stated before, bipolar technologies with high g_m/g_{ce} ratios and in-built phase-shifting capabilities are best suited for low-power high-Q active inductors. At microwave frequencies, there are two alternatives for integration of bipolar devices: high-speed silicon processes (BJT) and heterojunction GaAs or SiGe processes (HBT). In terms of basic theory or practical design, no essential differences can be found between the technologies, except for the fact that HBT processes have considerably higher transition frequencies and better-quality passive components. In fact, HBT technologies with semi-insulating substrates combine the benefits of GaAs-MESFET and Si-BJT processes. Both Si-BJT and GaAs-HBT technologies have been applied to the design of active resonators in this section.

GaAs-HBT active resonator

The underlying topology of the HBT active inductor [4.29] is again based on the Q-enhanced version in Figure 4.25a. The inductance is formed in a gyrator realized with a common-emitter and a common-base transistor connections (Figure 4.29a). The high losses in a standard gyrator configuration are compensated by the extra Q-enhancing resistor in the base of the non-inverting transistor, giving additional phase shift and ensuring high-Q operation at the desired frequency band.

The schematic diagram of the realized circuit is shown Figure 4.29b. The current of the transistor chain is controlled via the current mirror Q3,Q5. This adjustment controls the gyrator transconductances in Q2 and Q3, and thus the inductance value enabling the center frequency tuning of the resonator. The PIN-diode connected HBT Q4 forms a voltage-controlled resistor which shunts part of the signal to the ground and adjusts the Q value of the resonator. Q1 isolates the signal from the supply, and Q6 is for biasing. Only a little additional phase compensation in the form of R_{Qen} is needed, thanks to the very high g_m/g_{ce} ratio of the HBTs.

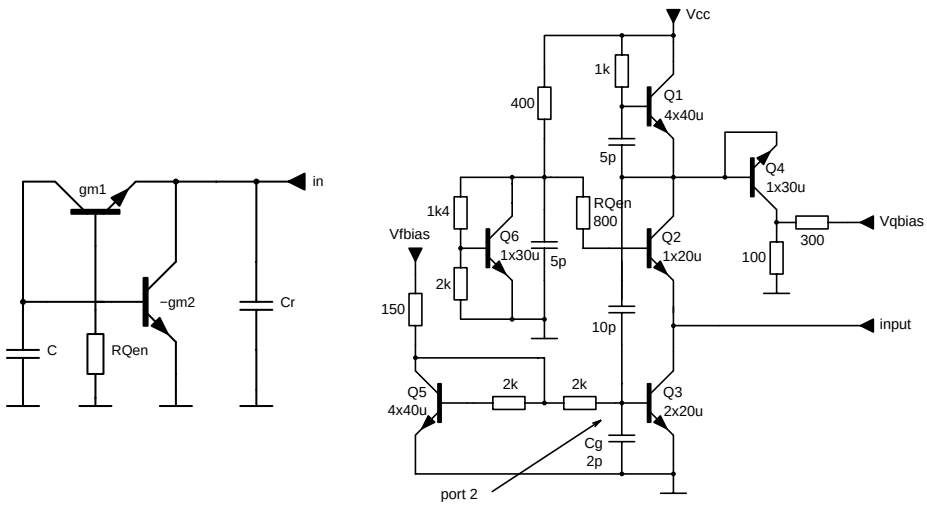

Figure 4.29 a) HBT realization of a gyrator with a Q-enhancing resistor in the base of the non-inverting transistor; b) Schematic diagram of the realized HBT active resonator

A GaAs/$Al_{0.3}Ga_{0.7}As$ HBT technology with SPICE compatible transistor models was used in the design. The f_T and f_{max} of the devices were 22 GHz and 55 GHz, respectively.

The measured inductance and series resistance curves together with the resulting unloaded Q are shown in Figure 4.30. The operating current of the resonator, drawn from a 3-V supply, varies from 2.3 mA to 3.3 mA, depending on the frequency adjustment. At the optimum, it is

2.8 mA leading to a power consumption of only 8.3 mW. This is a fraction of that of GaAs MESFET active inductors.

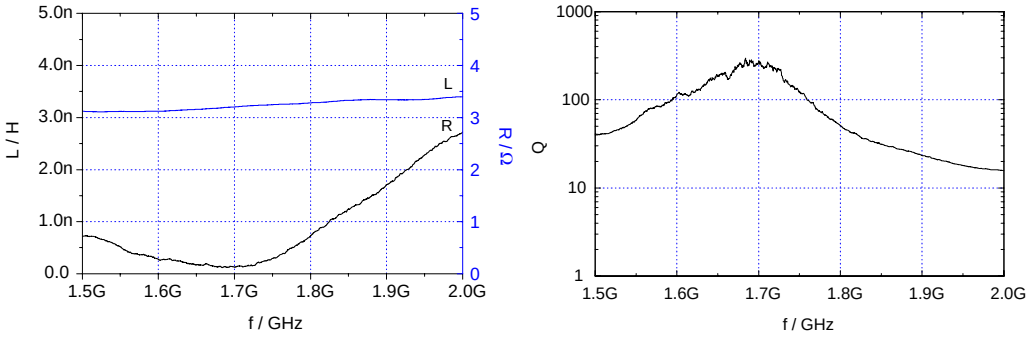

Figure 4.30 a) Measured inductance and resistance of the HBT active inductor; b) Measured unloaded Q of the HBT active inductor

Silicon-BJT active resonator

In this section, a differential Si-BJT microwave active inductor with a minimal number of passive components is presented [4.30]. The core of the resonator is a conventional active inductance simulating circuit. Two of these are connected appropriately to form a differential structure. Thanks to the existence of virtual ground nodes, many of the cumbersome passive coupling components can be omitted in the differential realization.

The Q-enhancement is realized with a tunable active phase shifting stage between the two transconductors. Furthermore, the base resistance of a bipolar transistor in a non-inverting common-base stage contributes to phase correction. According to Section 4.3, tuning of the phase shift compensation affects the Q value but unavoidably also the inductance. On the other hand, when the inductance is tuned by chancing the values of the transconductances with bias current, the output conductance values, and thus the phase error, are changing accordingly. Therefore, both quantities must always be tuned simultaneously.

Figure 4.31 shows the schematic diagram of the differential active resonator. It attenuates the even-order harmonic components and potentially gives better distortion performance than a single-ended topology. It must be noted, however, that the dynamic range enhancement described in Section 4.5 does not apply here, as the transconductors themselves are not differential. The transistors Qp3,n3 are the inverting and Qp2,n2 the non-inverting stages for the positive and negative signals. Qp4,n4 and the resistor-connected Q5 form the active feedback/phase-shifting network that can be tuned with the voltage V_{qb} to produce an exact phase shift for high-Q operation. The effective phase shift can be approximated with

$$\Delta\phi_{corr} = -\arctan\frac{\omega\left(g_m C_g - G_{tun} C_{gs4}\right)}{g_m\left(G_{tun} + g_m\right) + \omega^2 C_{gs4}\left(C_{gs4} + C_g\right)} \tag{4.51}$$

where C_g corresponds to the base-emitter capacitances of the devices Qp3,n3 acting as the gyrator capacitors, and G_{tun} is the RF conductance of Q5. The common-collector stage also isolates the high-impedance output of the non-inverting transconductor together with the active loads Qp1,n1, and provides DC level shifting. The wide tuning range for quality factor ensures stability in all conditions. The transconductances of the devices, and thus the inductance and the resonance frequency, are controlled by their I_c, i.e. the bias current I_{bias}. The effective high-Q inductance tuning range is from 1.9 nH to 2.7 nH, corresponding to resonance frequencies from

2.5 GHz to 3 GHz. In contrast to earlier active inductors, this topology does not employ passive components that have effect on the performance or sensitivity of the circuit. Especially, no high quality floating capacitors difficult to realize on silicon are required. The only capacitors in the resonator are Cra and Crb, the grounded resonating capacitors. Their losses are easily tuned out. The circuit operates at a 3-V supply voltage and draws 12 – 25 mW DC power depending on the current frequency bias setting.

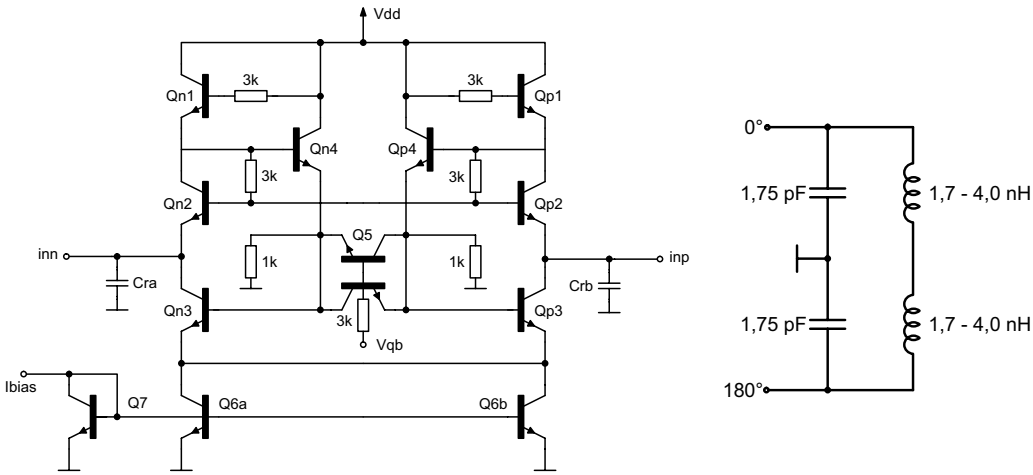

Figure 4.31 Schematic diagram of the differential BJT active resonator and its small-signal equivalent circuit

The simulated conductance and susceptance at 3 GHz and the resulting Q-value are plotted in Figure 4.32, respectively. Conductances at different tuning voltages and the frequency tuning characteristics are shown in Figure 4.33.

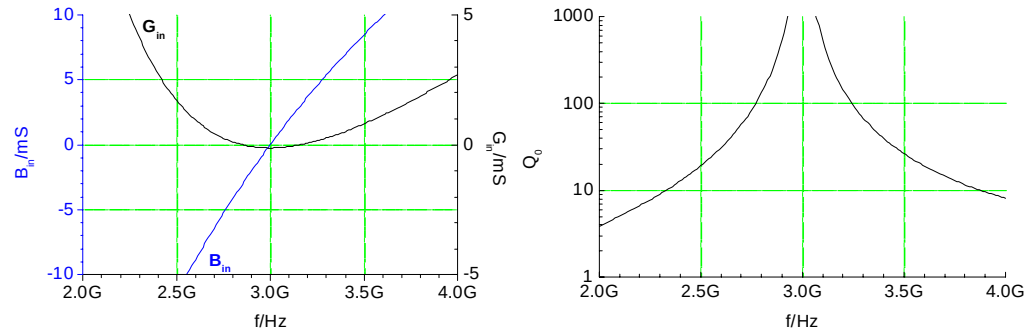

Figure 4.32 a) Simulated admittance of the BJT active resonator at 3 GHz; b) Simulated unloaded Q of the BJT active resonator

The simulated output noise voltage is 17 nV/Hz$^{1/2}$ which is more than twice the theoretical absolute minimum with the same Q_l = 10. Additional noise sources in the transconductors as well as in the auxiliary devices are not included in hand calculations, and this accounts for the difference. It should be noted that the theoretical values give the absolute performance limit only.

A test chip including a differential resonator and a differential band-pass filter was processed with a 0.8-µm Bi-CMOS technology. A microphotograph of the resonator circuit is shown in Figure 4.34. The active circuit area is 200 × 300 µm^2.

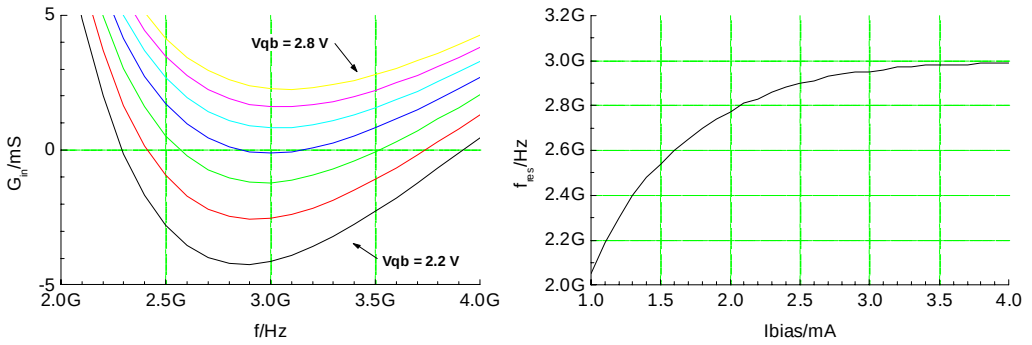

Figure 4.33 a) Conductance tuning vs. control voltage V_{qb};
b) Resonance frequency tuning vs. bias current I_{bias}

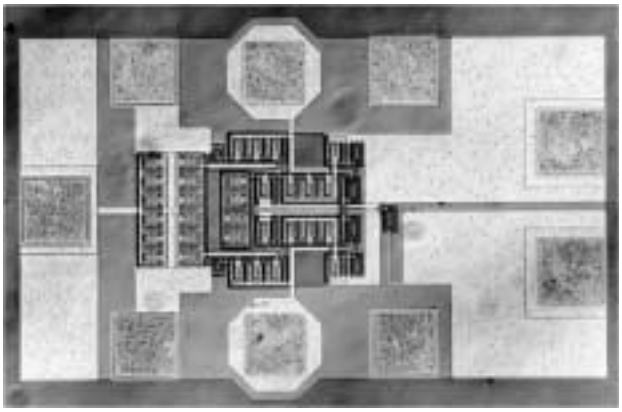

Figure 4.34 Chip layout of the active inductor

The measured small-signal characteristic curves are shown in Figure 4.35. The operating frequency range in wider than predicted by simulations, but the highest achievable high-Q resonance frequency is 120 MHz lower than anticipated.

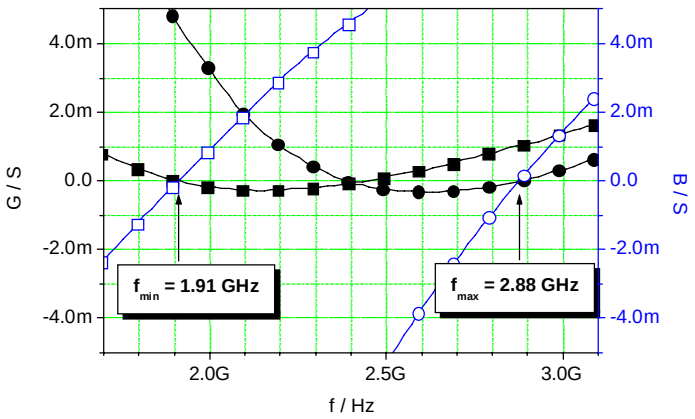

Figure 4.35 Measured conductance and susceptance of the BJT active resonator

Since differential resonators are two-ports, the y-parameters, corresponding to a differential one-port, must be calculated from the actual measured values by using the formula in Section

2.2.3. As far as measurement techniques are concerned, one of the greatest advantages of two-port circuits is that their noise figures can be measured, and the corresponding one-port noise source values de-embedded [Section 3.5.7]. This is why no measured noise data could be obtained from the previous single-ended active inductor resonators. Only by constructing a filter with well-known component values, and then measuring its noise properties, one can de-embed information on the actual single-ended resonator.

The de-embedded noise current of the differential BJT resonator in the vicinity of resonance is shown below (Q_l = 10). For comparison, respective measured and de-embedded data from a negative resistor resonator [5.4] is plotted in the same figure along with the passive equivalent. The active inductor resonator suffers from about four times higher a noise level than the negative resistor resonator, which is well in line with the theoretical estimations. The measured output noise voltage at resonance is 18.1 nV/Hz^{½}, while the theoretical minimum calculated from Eq. (4.27) would be 10.9 nV/Hz^{½}.

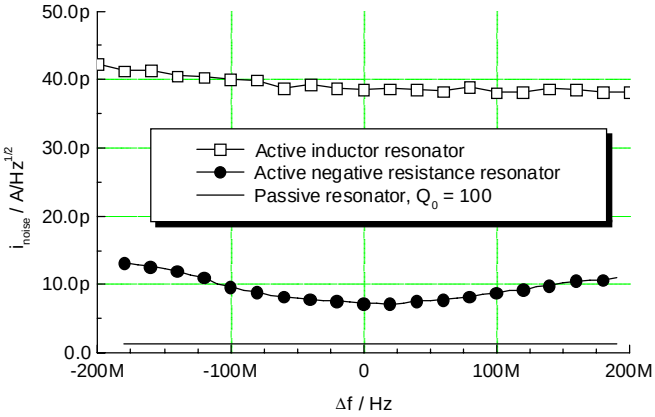

Figure 4.36 Noise currents of different resonator types, de-embedded from measured data

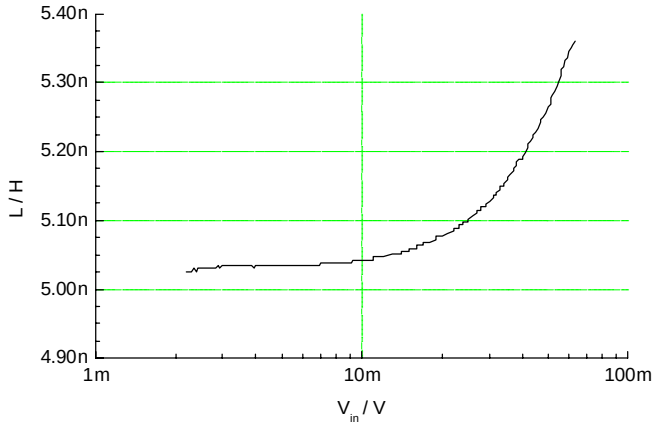

Figure 4.37 Measured inductance expansion of the BJT active resonator

Figure 4.37 depicts the measured inductance compression, or in this case expansion, of the circuit at 2.4 GHz. The extrapolated +1-dB expansion point is approximately 80 mV. Applying the definition for dynamic range given in Section 4.5.4, we can conclude that the dynamic range of this active inductor is roughly

$$DR = 20\log\left(\frac{80\text{mV}}{18\text{nV}/\sqrt{\text{Hz}}}\sqrt{\frac{10}{2.4\text{GHz}}}\right) \approx 49\text{dB} \tag{4.52}$$

when the loaded quality factor is 10 (BW = 240 MHz).

References

[4.1] B. Tellegen, 'The Gyrator, a New Network Element', *Philips Research Report*, Vol. 3, pp. 81-101, April 1948.

[4.2] W. Mason, W. Hewitt and R. Wick, 'Hall Effect Modulators and Gyrators Employing Magnetic Field Independent Orientations in Germanium', *Journal of Applied Physics*, Vol. 24, pp. 166-175, February 1953.

[4.3] C. Hogan, 'The Ferromagnetic Effect at Microwave Frequencies and Its Applications; the Microwave Gyrator', *Bell Systems Technical Journal*, Vol. 31, pp. 1-31, January 1952.

[4.4] M. Onoe and M. Sawabe, 'A Piezoelectric-Piezomagnetic Gyrator', *Proceedings of the IRE*, Vol. 50, pp. 1967-1973, September 1962.

[4.5] B. Bogert, 'Some Gyrator and Impedance Inverter Circuits', *Proceedings of the IRE*, Vol. 43, pp. 793-796, July 1955.

[4.6] B. Shenoi, 'Practical Realization of a Gyrator Circuit and RC-Gyrator Filters', *IEEE Transactions on Circuit Theory*, Vol. 12, pp. 374-380, September 1965.

[4.7] W. Holmes, S. Gruetzmann and W. Heinlein, 'High-Performance Direct-Coupled Gyrators', *Electronics Letters*, Vol. 3, pp. 45-46, February 1967.

[4.8] R. Riordan, 'Simulated Inductors Using Differential Amplifier', *Electronics Letters*, Vol. 3, pp. 50-51, February 1967.

[4.9] H. Orchard, 'Inductorless Filters', *Electronics Letters*, Vol. 2, pp. 224-225, June 1966.

[4.10] H. Orchard, 'Inductorless Bandpass Filters', *IEEE Journal of Solid-State Circuits*, Vol. 5, pp. 108-118, June 1970.

[4.11] H. Voorman and A. Biesheuvel, 'An Electronic Gyrator', *IEEE Journal of Solid-State Circuits*, Vol. 7, pp. 469-474, December 1972.

[4.12] S. Hara, T. Tokumitsu, T. Tanaka and M. Aikawa, 'Broad-Band Monolithic Active Inductor and Its Application to Miniaturized Wide-Band Amplifiers', *IEEE Transactions on Microwave Theory and Techniques*, Vol. 36, pp. 1920-1924, December 1988.

[4.13] S. Hara, T. Tokumitsu and M. Aikawa, 'Lossless Broad-Band Monolithic Active Inductors', *IEEE Transactions on Microwave Theory and Techniques*, Vol. 37, pp. 1979-1984, December 1989.

[4.14] R. Kaunisto, P. Alinikula and K. Stadius, 'Active Inductors for GaAs and Bipolar Techniques,' *Proceedings of Norchip Seminar*, Trondheim Norway, pp. 170-176, November 1993.

[4.15] P. Alinikula, R. Kaunisto and K. Stadius, 'Monolithic Active Resonators for Wireless Applications,' *Proceedings of IEEE Microwave Theory and Techniques Symposium*, San Diego USA, pp. 1151-1154, May 1994.

[4.16] R. Kaunisto, P. Alinikula and K. Stadius, 'Q-Enhancing Technique for High Speed Active Inductors', *Proceedings of IEEE International Symposium on Circuits and Systems*, London UK, pp. 735-738, May 1994.

[4.17] R. Kaunisto, P. Alinikula and K. Stadius, 'Active Inductors for GaAs and Bipolar Technologies', *Analog Integrated Circuits and Signal Processing*, Vol. 7, pp. 35-48, January 1995.

[4.18] Y. Wang and A. Abidi, 'CMOS Active Filter Design at Very High Frequencies', *IEEE Journal of Solid-State Circuits*, Vol. 25, pp. 1562-1573, December 1990.
[4.19] D. Blom and J. Voorman, 'Noise and Dissipation of Electronic Gyrators,' *Philips Research Report*, Vol. 26, pp. 103-113, 1971.
[4.20] J. Voorman and D. Blom, 'Noise in Gyrator-Capacitor Filters,' *Philips Research Report*, Vol. 26, pp. 114-133, 1971.
[4.21] A. Abidi, 'Noise in Active Resonators and the Available Dynamic Range,' *IEEE Transactions on Circuits and Systems – I*, Vol. 39, pp. 296-299, April 1992.
[4.22] G. Groenewold, 'The Design of High Dynamic Range Continuous-Time Integratable Bandpass Filters,' *IEEE Transactions on Circuits and Systems*, Vol. 38, pp. 838-852, August 1991.
[4.23] W. Kuhn, F. Stephenson and A. Elshabini-Riad, 'Dynamic Range of High-Q OTA-C and Enhanced-Q LC RF Bandpass Filters,' *Proceedings of IEEE Midwest Symposium on Circuits and Systems*, pp. 767-771, 1994.
[4.24] W. Kuhn, F. Stephenson and A. Elshabini-Riad, 'A 200 MHz CMOS Q-Enhanced LC Bandpass Filter,' *IEEE Journal of Solid-State Circuits*, Vol. 31, pp. 1112-1122, August 1996.
[4.25] P. Alinikula and R. Kaunisto, 'New Active Inductor Configurations for RF and Microwave Applications,' *Proceedings of European Conference on Circuit Theory and Design*, Davos Switzerland, pp. 229-234, 1993.
[4.26] G. Zhang, M. Villegas and C. Ripoll, 'Microwave Active Filter Using GaAs Monolithic Floating Active Inductor,' *Microwave and Optical Technology Letters*, Vol. 8, pp. 381-388, 1992.
[4.27] D. Haigh, 'GaAs MESFET Active Resonant Circuit for Microwave Filter Applications,' *IEEE Transactions on Microwave Theory and Techniques*, Vol. 41, pp. 1419-1422, July 1994.
[4.28] D. Haigh, D. Webster, R. Kaunisto, C. Nduijuba, A. Khanifar, M. Darvishzadeh, T. Parker, J. Scott and I. Thayne,' Developments in RF Design,' *Proceedings of IEE Colloquium on RF Design*, London UK, February.
[4.29] R. Kaunisto, P. Alinikula, K. Stadius and V. Porra, 'A Low-Power HBT MMIC Filter Based on Tunable Active Inductors,' *IEEE Microwave and Guided Wave Letters*, Vol. 7, pp. 209-211, August 1997.
[4.30] R. Kaunisto, K. Stadius and V. Porra, 'A 3-GHz Silicon-BJT Active Resonator and Filter,' *Proceedings of IEEE International Conference on Electronics, Circuits and Systems*, Lisbon Portugal, Vol. 3, pp. 197-200, September 1998.

5. ACTIVE RESONATOR FILTERS

5.1 Introduction

Second-order band-pass filters are developments of simple loaded resonators. Coupling to the surrounding circuitry is a way of turning one-port loaded resonators into two-port band-pass filters without changing their loading and quality factors. Therefore, many of the active resonator properties discussed in the previous chapters are directly applicable to the corresponding filters. This gives a convenient way of examining the properties of the equivalent stand-alone resonators: by measuring the filter performance, the corresponding one-port resonator performance can be obtained from the filter data, if necessary.

Active resonators must be tuned very accurately in order to ensure proper filter function. The band-pass loss must be minimized by nulling the resonator losses, while still maintaining the system stability. The importance of the tuning accuracy is even greater if more than one resonator is employed in the filter. Considering realizations as integrated circuits, twin-resonator fourth-order filters can be regarded as the upper limit, though, as the simultaneous absolute and relative tuning of the resonators becomes quickly overly difficult. If the coupled-resonator approach [Section 2.4] is used, the two resonators are identical making mutual matching easier and decreasing the number of separate tuning voltages or currents required. The coupling between the resonators and the termination resistances is more complex in twin-resonator filters, and the specific mathematical studies shown in this work are not valid per se. The more fundamental properties, such as the relation between noise and filter bandwidth, are applicable whatsoever.

Being the most essential phenomena in active resonator filters, noise and distortion properties are discussed in this chapter. Feasibility issues, particularly in view of relevant system applications, and automated tuning techniques required for commercial applications are studied. Realized monolithic filter test topologies by the author are shown, and measurement results presented. Finally, the concept and two realizations of a local oscillator generation circuit for direct-conversion transmitters are presented as possible applications for active resonator filters.

	Aparin [5.1]	Karacaoglu [5.2]	Pipilos [5.3]	Kaunisto [5.4]	Kaunisto [5.5]	Kuhn [5.6]
Type	negative resistor	negative resistor	negative resistor	negative resistor	active inductor	negative resistor
Tech.	GaAs	GaAs	BiCMOS	GaAs	BiCMOS	CMOS
f_0	1.5–2 GHz 2–2.6 GHz	2.3 GHz 4.7 GHz	1.6–2 GHz	3.6–4 GHz 3.2–3.6 GHz	1.91–2.88 GHz	816–875 MHz
rel. BW	4.9% 5.5%	5.2% 8.5%	2.9%	1.1% 12%	1.7%	2.1%
NF	17 dB 18 dB	– 7.5 dB	43 dB*)	19 dB 11 dB	29 dB	21 dB*)
CP	+1 dBm	– 0 dBm	-14 dBm*)	-20 dBm –6 dBm	-33 dBm	-18 dBm
BDR	78 dB 76 dB	– 80 dB	40 dB	59 dB 70 dB	30 dB	62 dB**)
nom. P_{DC}	300 mW	150 mW	26 mW	15 mW 30 mW	15 mW	210 mW

*Table 5.1 Performance comparison of some recent high-frequency active resonator filter designs; *) calculated from the given data; **) for the actual filter bandwidth*

5.2 Noise in Active Resonator Filters

The expressions of noise figures are derived for filters with both active resonator in this section. As shown in Section 2.4.4, the noise figure of a second-order resonator filter is

$$F = 1 + 2\frac{\hat{i}^2}{4kT\Delta\omega C_r'} \tag{5.1}$$

where $\hat{i}^2$ is the net noise current spectral density injected into the resonator input node, $\Delta\omega$ is the -3-dB bandwidth of the filter, and C'_r is the effective resonating capacitance. Using this equation, we can now calculate the noise figures for different noise currents.

5.2.1 Noise in Negative Resistor Resonator Filters

The noise current of a negative resistor is (r_n is the relative noise resistance for series-mode negative resistors, and g_n is the relative noise conductance for parallel-mode negative resistors) [Section 3.5]:

$$\hat{i}_n^2 = 4kTr_n, g_n|G| \tag{5.2}$$

When a lossy passive resonator is compensated with a parallel-connected negative resistor whose resistance is equal in magnitude but opposite in sign, the total noise current becomes

$$\hat{i}_n^2 = 4kT(1 + r_n, g_n)|G| \approx 4kT(1 + r_n, g_n)\frac{\omega_0}{Q_0}C_r', \quad Q_0 >> 1 \tag{5.3}$$

Hence, the noise figure of a negative resistor resonator filter is

$$F = 1 + 2\frac{Q_l}{Q_0}(1 + r_n, g_n) \tag{5.4}$$

where Q_0 accounts for all losses in the passive resonator, including the tunable capacitor losses. In terms of noise, negative resistor resonators behave just like ordinary passive resonators. With small values of r_n,g_n reasonable noise performance can be attained, provided that the passive resonator quality factor is high enough. As the combined Q of an integrated spiral inductor and a pn-varactor is maximally in the order of 10, it has a dominating effect on the minimum noise figure theoretically possible, even if r_n,g_n for the particular negative resistor were small.

5.2.2 Noise in Active Inductor Resonator Filters

According to Section 4.4, the noise current spectral density of a high-Q active inductor resonator at resonance is

$$\hat{i}_n^2 = \frac{\hat{v}_{n,1}^2}{\omega_0^2 L^2} + g_{m2}^2\hat{v}_{n,2}^2 = 4kT\gamma g_{m2}\left(1 + \frac{C_r'}{C_g}\right) \tag{5.5}$$

Applying Eq. (2.28), we get the noise figure of an active inductor band-pass filter:

$$F = 1 + 2\gamma \frac{g_{m2}}{\Delta\omega}\left(\frac{1}{C_g} + \frac{1}{C_r'}\right) = 1 + 2\gamma Q_l \sqrt{\frac{g_{m2}}{g_{m1}}}\left(\frac{C_g + C_r'}{\sqrt{C_g C_r'}}\right) \tag{5.6}$$

With an obvious choice of the parameters $g_{m1} = g_{m2}$ and $C_g = C$, this yields

$$F = 1 + 4\gamma Q_l \tag{5.7}$$

In the order of magnitude, the noise figure of a second-order active inductor band-pass filter is typically Q_0 times higher than that of a negative resistor with a passive-part quality factor of Q_0 [5.3][5.7] – [5.10]. This is a fundamental statement in favor of negative resistance filter.

5.3 Dynamic Range of Active Resonator Filters

The dynamic range of an active resonator filter is directly associated with the resonator dynamic range involved, since a second-order band-pass filter is nothing but a loaded parallel resonator with current excitation. The impedance transformation at the filter input and output is taken into account in the loaded quality factor of the resonator. It increases voltage peaking proportional to Q_l over the resonator [Section 2.4.5], but the noise voltage at the resonator output experiences the same amount of attenuation at the filter terminals. The dynamic ranges of transconductor-capacitor filters and Q-compensated LC filters have been compared by Kuhn at al. [5.9][5.10]. They have shown that the dynamic range of a Gm-C filter is Q_0^2 times lower compared to that of a Q-enhanced LC filter with a passive unloaded Q of Q_0. The same result through a more complete analysis has been attained in the previous chapters of this thesis.

$$DR_{negres} \sim \left(\frac{Q_0}{Q_l}\right)^2, \quad DR_{actind} \sim \left(\frac{1}{Q_l}\right)^2 \tag{5.8}$$

The increase in the dynamic range level can be explained by examining the signal currents that must be delivered by the active devices in the two cases. In the gyrator-capacitor circuit, the signal current is determined by the signal voltage divided by capacitive reactance. In the negative resistance filter, the signal current is determined by the signal voltage divided by *negative resistance*. Since the magnitude of the negative resistance is a factor of Q_0 larger than the capacitive reactance, a factor of Q_0 less current is required in the negative resistance filter for a specified signal voltage.

5.4 Practical Feasibility in Systems

Integrated RF filters seemingly offer several benefits for applications in the RF front ends of cellular phones. The currently used passive filters cannot be adjusted to cover multiple systems and frequency bands, and the only feasible solution is to use selectable filters for each designated frequency band. Passive filters are bulky and expensive, although much progress has been made during the last decade. On the other hand, monolithic RF filters are easily tunable, small and inexpensive in both price and manufacturing costs. The drive towards increasing miniaturization would make them unparalleled elements for future handheld systems.

This section deals with system requirements for RF filters and gives an insight into why the realizable integrated RF filters, with a few exceptions, are not feasible in most telecommunication systems after all.

5.4.1 2G GSM

The relative bandwidth of a signal channel in GSM systems is 0.2% (200 kHz/900 MHz). This makes channel selection filtering impossible. Instead, the main function of the RF filters is to relax the dynamic range requirements for the following stages, i.e. by removing the unwanted signal power from other wireless systems as well as possible. Obviously, the dynamic range of the filter itself becomes a critical parameter. In [5.11] five possible applications for active RF filters are considered: 1. Frequency-Division-Duplex (FDD) heterodyne receiver filters, 2. Time-Division-Duplex (TDD) heterodyne receiver filters, 3. Image-rejection filters, 4. TDD direct-conversion receiver filters, and 5. direct-modulation transmitter filters. The system architecture is shown in Figure 5.1. In the following text, excerpts from [5.11] are referred.

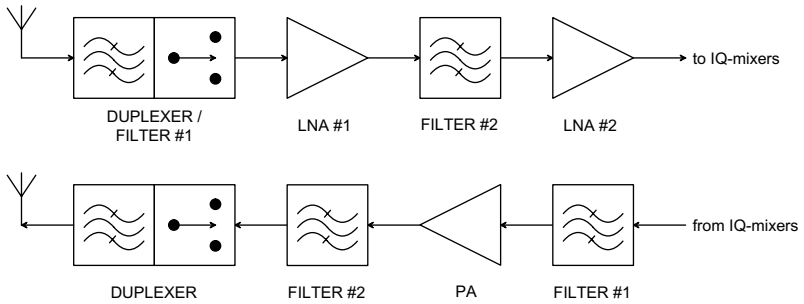

Figure 5.1 Receiver and transmitter RF-chains in a cellular phone architecture

FDD heterodyne receiver filters

In pure FDD systems, the receiver and the transmitter are both on at the same time. The first filter of the receiver chain, the duplexer, must be able to attenuate the transmitter signal whose power level is typically +30 dBm. The transmission and reception bands are close to each other (GSM 900: 890 – 915 MHz and 935 – 960 MHz), resulting in unacceptably high stop-band signal levels for any active filter.

TDD heterodyne receiver filters

In TDD systems, the transmitter is turned off during reception. Now, the maximum signal strength experienced by the first receiver filter is caused by out-of-band blocking signals that can have a maximum power level of approximately 0 dBm in digital cellular systems. The out-of-band signals need to be attenuated about 20 dB down to the level of the in-band blocking signals.

When applying active filters to TDD duplexers, the main concern is noise. The specifications are demanding: the minimum detectable signal is –102 dBm in GSM systems with a carrier-to-noise ratio requirement of about 10 dB. Hence, the maximum system noise figure for the receiver becomes:

$$F_R < -102 + 174 - 10\log(200\,\text{kHz}) - 10 = 9\,\text{dB} \tag{5.9}$$

As the duplexer is the first element in the chain, its noise figure must definitely be much smaller than F_R (Friis's formula, Eq. (2.32)). This is impossible for active filters.

Image-rejection filters

The second RF filter in the receiver chain in used mainly for image rejection. The image band rejection requirements vary between 60 – 90 dB in different systems. The filtering is distributed to the duplexer and the second filter. If the IR-mixer has an image rejection ratio of 30 – 40 dB and the duplexer provides additional 20 – 25 dB, up to 40-dB rejection is expected

from the second filter, which is manageable. The overall power range of the received signal would be too large for active RF filters without prior gain control, typically -90…-5 dBm in digital cellular phones. However, the LNA has stepped gain control in most cases for this purpose.

The system noise floor of a filter in a frequency-division receiver architecture is defined by the channel bandwidth, as shown in Eq. (5.9). Therefore, the baseband-referred system dynamic range of the filter gets significantly larger than its own RF-band dynamic range. Kuhn [5.6] suggests that as far as the system dynamic range is concerned, an active filter (with some gain as a byproduct of Q enhancement) can have comparable performance with a passive-filter – LNA combination. However, this does not alleviate the requirement for RF noise figure, which is typically 10 – 18 dB for the second filter if the LNA has a gain of 20 dB.

The other more promising alternative is to use active band-stop filters for image rejection. The filter notch is tuned to attenuate the image band, while the reception band remains unchanged. With this technique, more than 65-dB image rejection has been achieved from the second filter itself [5.12]. A series LC resonator can be used in conjunction with a series-mode negative resistor with potentially low-noise capabilities [Section 3.5.4]. The main advantage of this approach is that the reception band lies far from the resonance frequency, and thus the voltage swing over the negative resistor is low, namely

$$\left|V_{-R}\right| = \frac{1}{Q_0}\left|\frac{w}{w^2-1}V_{in}\right| \tag{5.10}$$

where $w = \omega/\omega_0$ and Q_0 is the resonator unloaded Q. For instance, in [5.12] w = 1.9GHz/2.5GHz = 0.76 and with a realistic Q_0 = 10, a 15-dB reduction in voltage swing across the negative resistor occurs, compared to the voltage swing over the series resonator, which itself is low off resonance. Therefore, the dynamic range of the filter is acceptable for a cellular receiver.

TDD direct-conversion receiver filters

In a direct-conversion transceiver, the modulation and demodulation are carried out directly at the carrier frequency. This arrangement reduces the number of required filters, as neither IF nor image-band filters are needed. The dynamic range requirements for the first filter in the receiver chain are essentially the same as for the heterodyne receiver.

Direct-modulation transmitter filters

In the transmitter chain, the last filter after the power amplifier is used for cleaning up the transmission spectrum. Naturally, it cannot be active, as the power level is very high. The filter between the IQ-modulator and the power amplifier is used for filtering the modulator output signal from the leaking spurious frequencies and for attenuating the noise floor outside the transmission band. The most important specification for the filter is its noise contribution at the stop-band. Unfortunately, the stop-band noise of an integrated RF filter easily exceeds the stop-band rejection by 10 – 20 dB.

Frequency synthesizer

The only RF block in a cellular phone, where the required dynamic range is small, is the frequency synthesizer. In generating the LO signal in a direct modulator, a problem will occur if the high-power output signal couples back to the oscillator chain. The coupling can be avoided if the LO signal is generated inside the modulator from two reference signals. Then, however, the generated LO signal must be filtered prior to the mixers. This is a potential application for monolithic RF filters, and it will be elaborated in the following sections 5.7 and 5.8.

5.4.2 3G WCDMA

The transceiver architecture for WCDMA cellular phones is similar to Figure 5.1, and basically the same considerations for active filter usage apply. The 3G system applies FDD, and thus the duplexer requirements are stringent for adequate isolation between the receiver and the transmitter chains.

According to [5.13], the receiver noise figure must not exceed 9 dB including the loss of the duplexer. As it is practically the same as in GSM systems, similar receiver chain noise requirements apply to filters. The pass-band shape and selectivity specifications are more demanding in WCDMA receivers, which makes the application of active filters even more unfeasible. The dynamic range specifications are not alleviated either. The image rejection needs to be >84 dB for the entire receiver, and the notch filter concept can be used accordingly.

5.4.3 Bluetooth

The short-range wireless protocol Bluetooth could offer some possibilities for active RF filter application. Since it has been desired that utilization of simple, small and cheap transceiver circuits would be possible, the specifications are relatively loose.

The Bluetooth system is operating at the ISM band (2400 – 2483.5 MHz) with 1-MHz channels and frequency hopping . The band is wide enough (Q_l = 30) for active resonator filters with reasonable dynamic ranges, but still too narrow for purely passive monolithic resonators.

Bluetooth is a TDD architecture, where the noise performance of the first filter is the limiting specification. Using Eq. (5.9) and referring to the Bluetooth specifications [5.14], the receiver chain noise figure can be as high as 23 dB, since the sensitivity requirement is –70 dBm. This is within the capabilities of active resonator filters, especially if combined with a low-noise amplifier. The specification for SFDR is 50 dB, which is somewhat more challenging in terms of active filter design.

5.5 Automated Tuning Techniques

For full control over an integrated active resonator, both the center frequency and the unloaded quality factor, or loss compensation, must be externally variable. The absolute process tolerances are too wide for the parameter accuracy required by filters, and the strength of active resonators lies in their adaptivity. It is acceptable to tune each resonator manually in test circuits like in this thesis. However, if the application has a real-life target, the center frequencies of individual resonators have to be tuned via a common reference, and the pass-band loss must be automatically minimized without risking stability.

When multiple resonators are included in the filter, the coupling between them becomes critical, if the desired prototype function (Butterworth, Chebyshev etc.) and the pass-band shape are to be maintained over the entire operating frequency band. The task becomes tedious if the number of resonators exceeds two or three, for it is practically impossible to develop an automatic tuning system for this purpose.

5.5.1 Master-Slave Tuning

The master-slave control scheme is an effective method of realizing resonance frequency and loss control regardless of the resonator type [5.1][5.15]. It is based on an unloaded oscillating slave resonator in a dual-loop configuration. The slave resonator is identical to that/those in the actual filter. The block level diagram of the master-slave-tuning concept is shown in Figure 5.2.

The frequency control loop is essentially a phase-locked loop where the slave resonator acts as the voltage-controlled oscillator. It locks the resonance frequency to an external sub-harmonic reference signal that is defined by the divider-by-N. It is important that the reference

input does not fall upon the filter band to prevent interference. The low frequency also enables the use of traditional digital phase detectors in the PLL. The oscillation magnitude should be as small as possible for minimizing coupling between the master oscillator and the filter.

The Q control loop automatically limits the oscillating amplitude to a certain small value via a rectifier and an integrator. Thus, the small-signal behavior is ensured in the master resonator, and the characteristics remain well matched to the slave filter resonators. The output amplitude of the master oscillator/resonator is detected in the rectifier, and the resulting DC voltage is compared with a reference voltage in the integrating operational amplifier. This voltage is chosen appropriately to maintain low oscillation amplitude.

The master and slave resonators must naturally be well matched on the die, otherwise instability or excess pass-band loss may result. The problem is more severe in very narrow-band filters, where the margin between the unloaded and loaded Q of the resonators is smaller. Another issue is the stability of the loops themselves. As the frequency and Q controls of an active resonator are never independent, adjusting one will change the other, too. To avoid any instability resulting from such interactions, the bandwidth of the Q control loop should be larger than that of the PLL [5.1].

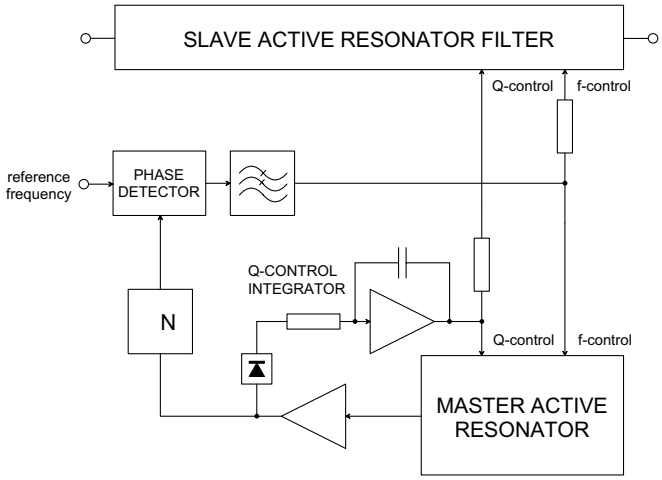

Figure 5.2 Master-slave automatic control scheme

5.5.2 Coupling Factor Tuning

In a multi-resonator filter, the coupling between the resonators must be accurate and tunable if the resonator parameters change. Aparin [5.1] has solved this problem by using matched varactor diodes as coupling capacitors between the resonator stages. Their control voltage is common with that of the resonator varactors. This approach ties the coupling to the center frequency tuning, but good pass-band shapes have still been attained with this technique.

Perhaps a more sophisticated scheme has been presented by Kuhn [5.6][5.10]. Here, the two resonators are magnetically coupled through the suitable placement of the inductors on the die, and a coupling neutralization circuit is designed for accurate control over the coupling coefficient. The neutralization circuit ensures that the phase relationship between the inductors is correct for a flat pass-band response. The control is, however, not automatic. The same principle for active inductor resonators have been used in [5.15].

5.5.3 Adaptive Transconductor Biasing

The loss control in a negative resistor resonator ensures maximum-Q characteristics. When the input signal level is raised and the negative resistor starts to compress, a constant tuning current is not able to maintain the highest available Q any more. If the transconductor bias adapts to the signal level across the resonator, this effect can be circumvented in some extent, and the upper limit of the dynamic range is enhanced. Notably, the bias current control must be accurate not to inflict instability.

5.6 Realized Active Resonator Filters

5.6.1 Active Negative Resonator Filters

Both GaAs-MESFET and Si-BJT technologies have been utilized in demonstrating the design of negative resonator filters. The MESFET realization is based on the compensated resonator from Section 3.8.2 with a slightly modified topology and component values. The varactor diode model has been enhanced in order to get a good match between simulations and measurements. I shall concentrate on only the MESFET filter here, as the BJT versions will be treated in Section 5.8.5. The filters in question have been published by the author in [5.4]. Preliminary studies on the issue can also be found in [5.16].

Active resonator

Figure 5.3 shows the schematic diagram of the employed active resonator. It consists of a passive spiral inductor, a pair of varactor-connected back-to-back MESFETs (M4, M5), and an active tunable negative resistance. The negative resistance is a single-ended version of the cross-coupled differential pair well suited for integration. The equal transconductances of the differential transistors can be varied, and thus the amount of negative resistance and loss compensation, via the current source M3.

A 10-nH spiral inductor has been added to provide gate bias for the common-drain MESFET M1. It reduces noise compared to the previous resonator, as no high-value high-noise bias resistors need to be connected to the high-impedance output node. The inductor has a small effect on the resonance frequency of the resonator, which must be taken into account.

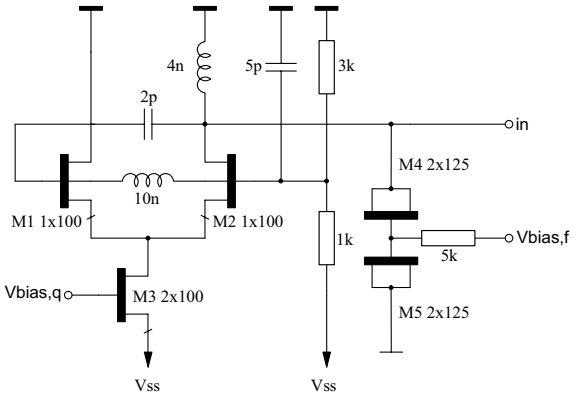

Figure 5.3 Tunable active resonator with negative resistance compensation

The varactors enable frequency tuning for the resonator. As their Q values change during tuning, the negative resistance compensation must be adjusted accordingly for zero loss at each center frequency. The back-to-back connection ensures the maximal large-signal performance of the varactors.

The negative supply voltage is beneficial in two reasons: the depletion-mode MESFETS are biased with negative gate-source voltages, and no large shunt capacitor is required for providing the RF ground for the resonating inductor.

Band-pass filters

Two coupled-resonator band-pass filters have been constructed from the resonator: a second-order single-resonator filter and a fourth-order filter with two identical resonators (Figure 5.4). The active resonators are connected to each other and to the 50-Ω terminations with small coupling capacitors. These are realized as interdigital capacitors or series-connected MIM (Metal-Insulator-Metal) capacitors. The center frequencies are 3.8 GHz for the second-order band-pass filter and 3.4 GHz for the fourth-order band-pass filter.

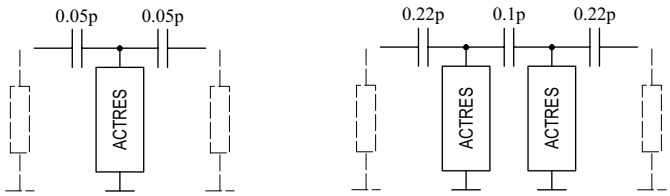

Figure 5.4 Configurations of the second-order filter and the fourth-order filter

Realized circuit and results

The filters were simulated with the advanced Parker-Skellern MESFET device models [5.17] giving excellent matches between simulations and measurements. The GEC-Marconi F20 20-GHz D-MESFET process was used for the realization. Figure 5.5a shows the measured transfer functions for the second-order filter at the nominal and the extreme center frequencies. In Figure 5.5b the measured and simulated responses of the fourth-order filter are presented. In both filters, the tuning range is roughly the same 400 MHz. The simulated and measured responses for the second-order filter also match extremely well. The simulated curves are not shown, as they coincide with the measured ones.

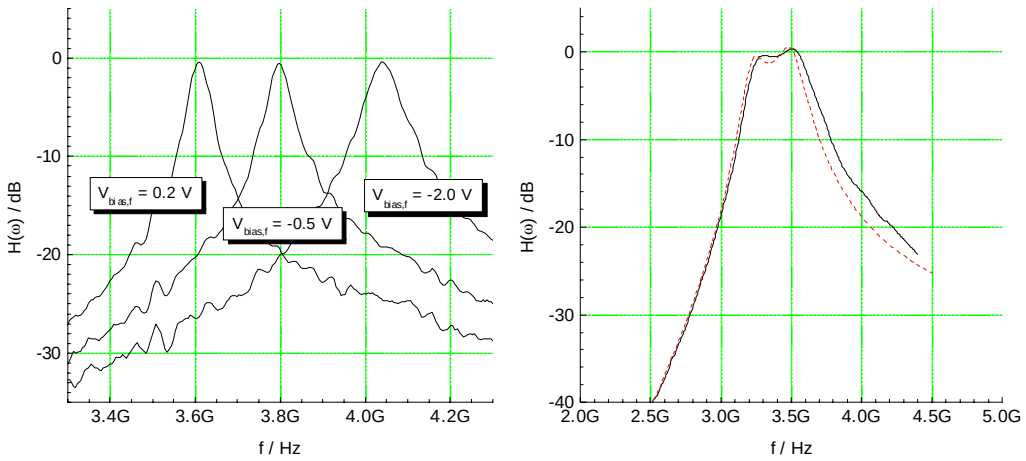

Figure 5.5 a) Measured responses of the second-order filter over the frequency tuning range; b) Measured and simulated (dashed) nominal frequency response of the fourth-order filter

The noise performance of the filters is of great interest. By using the theoretical expression for the noise figure of the negative resistor resonator filter [Section 5.2.1]

$$F = 1 + 2Q_l\left(\frac{1}{Q_{L0}} + \frac{1}{Q_{C0}}\right)(1 + g_n), \quad g_n = \gamma = 2/3 \tag{5.11}$$

with the process-defined values Q_{L0} = 15 and Q_{C0} = 12, we can calculate the theoretical noise figure for the single-resonator filter to be 16.9 dB. The dominant effect of the filter bandwidth and the resonator component Q values should be noted again; the noise contribution of the negative resistance is ideally only 2.2 dB. The measured noise figures are somewhat higher than the calculated values, mainly due to the very simplified and optimistic MESFET noise model in Eq. (5.11). The measured noise performances of both filters are plotted in Figure 5.6.

The value of negative resistance is dependent on the input power, resulting in noteworthy Q degradation at high input levels. Therefore, it is essential to retune the negative resistance circuit when the input power is raised. By this action, the dynamic range of the filter can be extended. The limit is set by stability, and the compensation cannot be increased beyond a certain point without causing oscillation. The input power level, still with a zero pass-band loss at this point, can be defined as the maximum input power for the filter. Practically, this is equivalent to the compression point as the pass-band attenuation of the filter starts to grow after this power level. The measured maximum power levels and the third-order intermodulation intercept points of the filters are illustrated in Figure 5.7. Some essential figures of merit are tabulated in Table 5.2. The spurious-free and blocking dynamic ranges (SFDR/BDR) are 20 – 30 dB higher than in active inductor filters. The wide-band fourth-order filter has clearly better power handling capabilities due to the reasons discussed in Section 5.3.

The spurious-free dynamic range SFDR is defined as the distance of the input power at which the third-order IM product rises off the noise floor, to the noise floor. More widely used is the blocking dynamic range BDR that is the distance of the input power at -1-dB compression to the noise floor. They can be calculated by using the following relations:

$$\begin{cases} \text{Noise floor} = \text{-174 dBm/Hz} + NF + 10\log BW \\ \text{SFDR} = \frac{2}{3}(IIP_3 - \text{Noise floor}) \\ \text{BDR} = ICP - \text{Noise floor} \end{cases} \tag{5.12}$$

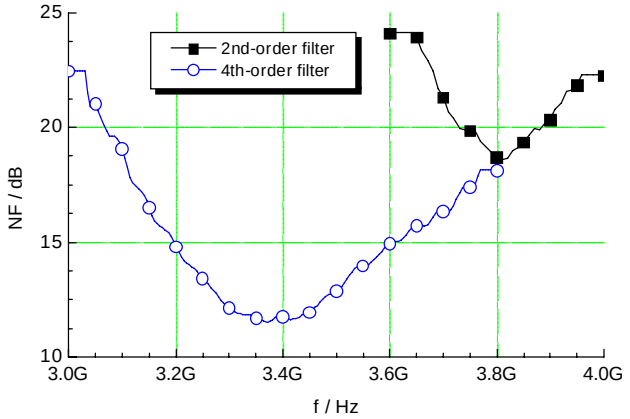

Figure 5.6 Measured noise figures of the filters

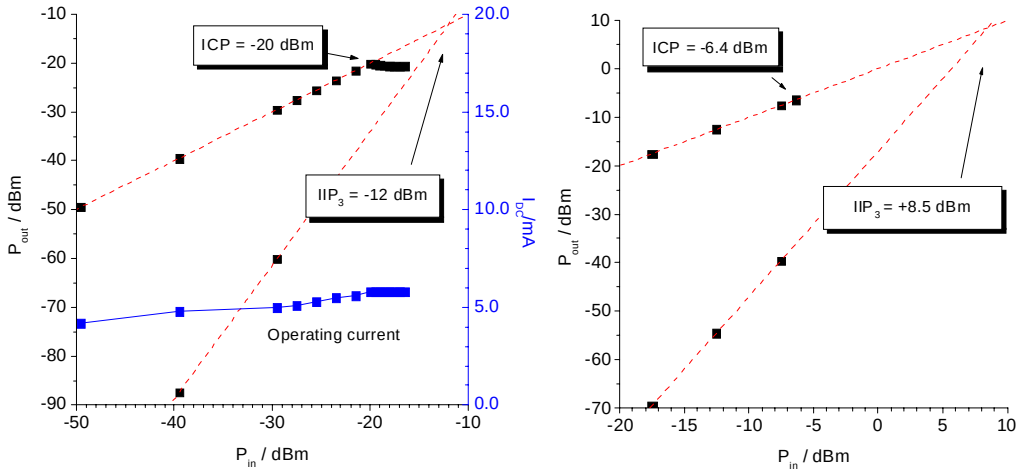

Figure 5.7 Measured power responses of a) the second-order filter and b) the fourth-order filter

	Second-order filter	***Fourth-order filter***
Center frequency	3.8 GHz	3.4 GHz
Freq. tuning range	± 200 MHz	± 200 MHz
-3 dB bandwidth nom.	40 MHz	400 MHz
NF	19 dB	11 dB
Max. input power	-20 dBm	-6.4 dBm
IIP3	-12 dBm	+8.5 dBm
SFDR / BDR	44 dB / 59 dB	57 dB / 70 dB
Operating current nom.	5.0 mA	10 mA

Table 5.2 Measured performance figures of the two filters

5.6.2 Active Inductor Filters

Active inductor resonators can be used in filters in the same manner as negative resistor resonators, and the frequency responses are fully compatible. The only difference can be observed in the tuning ranges that are larger in active inductor filters. This is due to the inductance tuning being able to vary the resonance frequency within wider limits than the capacitance tuning in varactors.

The GaAs-HBT and Si-BJT resonators, treated in Section 4.6.5, are applied to filter design by the author in [5.5] and [5.18]. More contribution to the issue can be found [5.19], [5.20].

GaAs-HBT filter

A sixth-order tri-resonator band-pass filter was designed for experimental purposes, although it was understood that the tuning of the individual resonators would be tedious. The filter is based on the sixth-order Chebyshev prototype filter, and it was constructed by chaining three active resonators with capacitive coupling (Figure 5.8). The drawback of this approach is the very small coupling capacitances required for narrow-band operation that are difficult to integrate. This problem can be alleviated if the overall impedance level is raised, but since the circuit was designed for on-chip measurements, the impedance level remained 50 Ω.

To facilitate the measurements, all the resonators have common bias voltages. This prevents precise adjustment of individual resonators and full control over the response. In a practical circuit, real-time tuning of several independent biases would be very difficult, and therefore

common biasing was explored. The chip size is 1.2 × 1.2 mm^2. The microphotograph of the chip is shown in Figure 5.9.

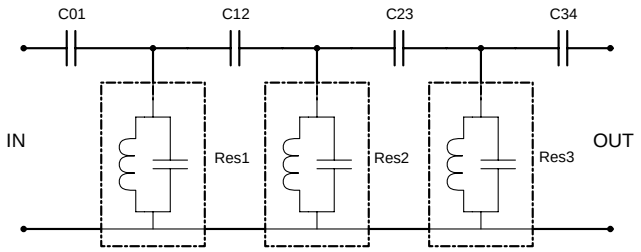

Figure 5.8 Top-level schematic of a sixth-order filter with grounded resonators

The measured response is shown in Figure 5.10. The tuning range is 2.17 GHz – 2.39 GHz but due to the common biasing, the pass-band is clearly distorted at both extremes. The frequency tuning voltage is swept from 2.2 V to 2.6 V, and the Q tuning voltage is set within 1.25 V – 1.95 V to give zero loss at the pass-band. The optimum is at 2.32 GHz with 300 MHz -3-dB bandwidth.

The operating current of the whole filter varies from 7 mA to 10 mA depending on the frequency adjustment. At the optimum, it is 8.3 mA, resulting in only 25-mW power consumption with a 3 V supply voltage. This is only a fraction of that of the GaAs-MESFET active inductor filters.

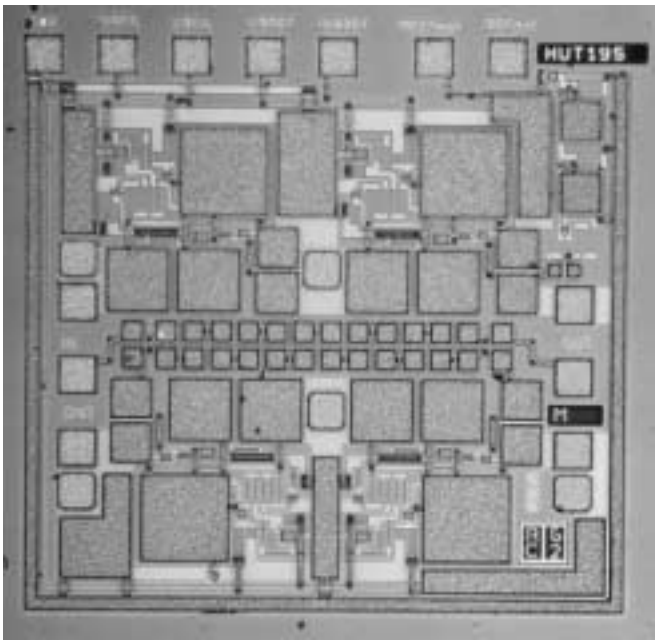

Figure 5.9 Microphotograph of the chip. The physical size is 1.2 × 1.2 mm^2. The chip contains a triple-resonator filter and a slave resonator oscillator with an output buffer amplifier

Non-linearities cause severe pass-band shape degradation at higher signal levels. The shape remained satisfactory up to -20-dBm input level that can be regarded as the upper limit of the dynamic range. The maximum power level can be increased by raising the operating current, naturally at the cost of higher power consumption. A noise figure estimate of 35 dB was obtained with the Y-factor method, resulting in a dynamic range of 34 dB.

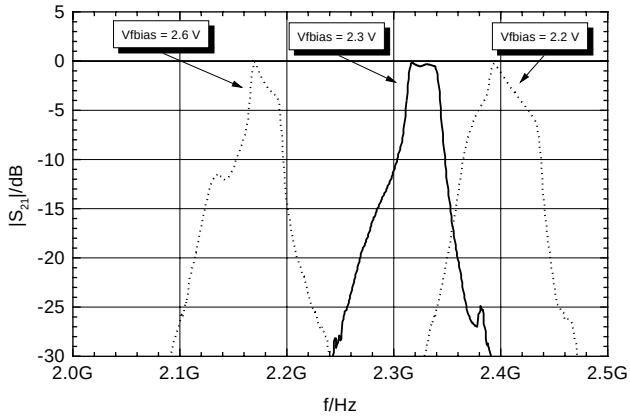

Figure 5.10 Measured S_{21} of the HBT filter. The tuning range extends from 2.17 GHz up to 2.39 GHz with V_{fbias} settings of 2.2 V - 2.6 V. The optimum is at 2.32 GHz (V_{fbias} = 2.3 V)

Si-BJT Filter

A differential second-order pass-band filter with one bipolar active resonator [Section 4.6.5] was designed for 3 GHz. The -3-dB bandwidth is 50 MHz (1.7% at 3 GHz). The topology of the filter is similar to that of Figure 5.4a with 0.25 pF coupling capacitors on both differential signal lines. The intended tuning range is 2.5 – 3 GHz within which the pass-band loss can be cancelled out with the Q tuning of the resonator. The simulated transfer function at both tuning extremes is plotted in Figure 5.11a. The noise figure for the filter was simulated to be 27 dB, which is again significantly more than the theoretical estimation. The simulated -1-dB compression point is as low as -33 dBm resulting in a blocking dynamic range of only 35 dB.

The realized filter suffered from a -30-dB transfer attenuation, what seems an apparent processing error. Therefore, the measured data is actually from the resonator-only measurements back-annotated into the simulator. As the coupling capacitors were properly modeled, the procedure gives realistic results. The transfer functions obtained in this manner are shown in Figure 5.11b. The tuning range is wider, but the maximum frequency is 120 MHz lower than predicted.

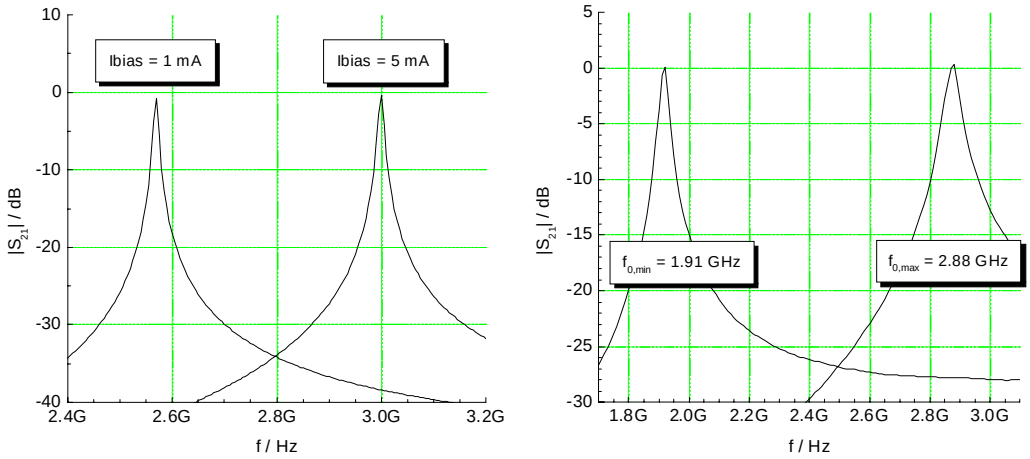

Figure 5.11 Filter transfer functions at both ends of the tuning range: a) simulated, and b) de-embedded measured

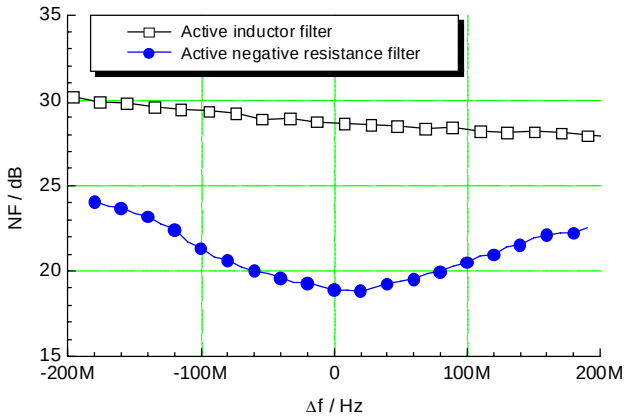

Figure 5.12 De-embedded measured noise figure of the filter with the corresponding result from Figure 5.6

The de-embedded measured noise figure of the filter is 29 dB (Figure 5.12). With the simulated -33-dBm compression point and the loaded Q of 60, this yields BDR = 36 dB. Calculated from the measured resonator-only value in Section 4.6.5, it is 34 dB, which is in good agreement with the simulations. It is noteworthy that the dynamic ranges from this differential active inductor filter are comparable in magnitude with the numbers from the single-ended HBT filter. This was expected keeping in mind the theory in Section 4.5.3. Although the circuit is differential, the transconductors themselves are single-ended, and the second-order non-linearities are not cancelled in the transconductors.

The power consumption of the filter is 6.6 – 23 mW, depending on the center frequency setting.

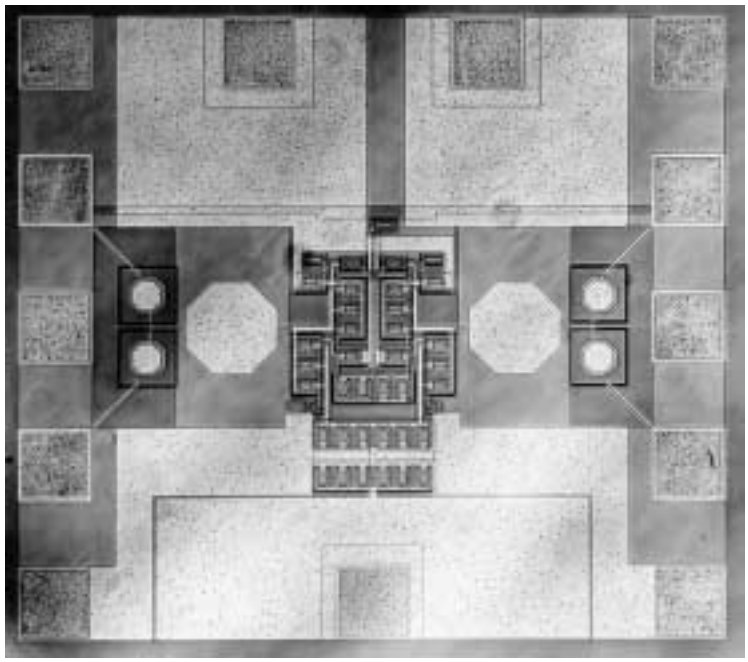

Figure 5.13 Photograph of the filter; the active die area is 300 x 600 μm^2

5.7 Application Case I: Local Oscillator Generation Circuit for Direct Conversion Transmitters in GaAs-MESFET Technology

5.7.1 Introduction

The continuous drive towards higher miniaturization and reduction of the overall cost of the handheld terminals has made the direct conversion concept attractive among different receiver-transmitter architectures. The key advantage of the direct conversion topology is the reduced need of RF circuitry, and that no expensive and bulky IF filters are needed. Consequently, the integration level is increased. The direct conversion architecture suffers from some important drawbacks that the designer has to consider when selecting the appropriate architecture: the oscillator feedthrough and oscillator backward transmission in the receiver and the disturbance of the local oscillator by the power amplifier in the transmitter.

In a direct conversion transmitter, coupling between bond wires and package pins, and therefore leakage of the power amplifier output, corrupts the in-band local oscillator signal spectrum (Figure 5.14). In the following, a circuit is demonstrated which, if integrated on the same die with the transmitter, circumvents the effect of coupling of the power amplifier output to the local oscillator signal.

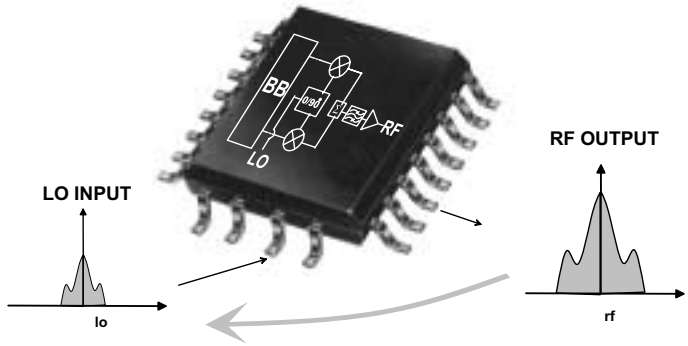

Figure 5.14 Leakage of power amplifier output to the local oscillator signal input

5.7.2 LO Signal Generation Circuit

In a direct conversion transmitter, the transmitted carrier frequency is equal to the local oscillator frequency. The direct conversion IQ modulator performs both modulation and upconversion of the baseband signal. In the modulator, the quadrature signals, I and Q, are upconverted in the quadrature mixers. The modulator is followed by a power amplifier which amplifies the transmitted signal and provides the required output power.

When generating an LO signal in a direct conversion transmitter, problems will occur if the modulated high-power output signal is coupled back to the oscillator chain. Illustrated in Figure 5.14, the power amplifier output has a modulated high-level waveform and a spectrum centered around the LO frequency. Coupling between bond-wires and package pins of the 'noisy' power amplifier output signal corrupts the local oscillator signal spectrum and modulates this signal. The impure local oscillator signal is then used for upconverting the baseband signal, resulting in a distorted RF output signal. In order to save power, the power amplifier is in many cases switched on and off periodically. The switching of the power amplifier creates sharp transitions in the signal waveform, and as a consequence, undesired harmonics and spurious frequency

components worsen the problem with the leakage of the power amplifier output to the local oscillator signal input.

Distortion of the LO signal spectrum in a direct conversion transmitter is alleviated if the coupled RF output signal does not create any in-band frequency components. This can be accomplished by generating the desired local oscillator signal to be used in the up-conversion mixer of the direct conversion transmitter from two local oscillator signals [5.11][5.21]. The local oscillator signal is generated as shown in Figure 5.15, where one of the input signals is divided by two and then mixed with the other input signal. The wanted LO signal is then given as one of the mixing products.

The frequencies of the input signals should be selected in such a way that they do not create any in-band mixing, intermodulation or harmonic signals that degrade the purity of the wanted LO signal. If the desired local oscillator signal bandwidth is $f_{LO,max}-f_{LO,min}$ the requirement for the input signal frequencies is:

$$\left|nf_{LO2} \pm mf_{LO1}\right| \notin \left[f_{LO,\min}, f_{LO,\max}\right] \quad \forall n,m \in [-5,-4,...,4,5] \tag{5.13}$$

$$f_{LO} = f_{LO2} - \frac{1}{2} f_{LO1}, \quad f_{LO} \in \left[f_{LO,\min}, f_{LO,\max}\right] \tag{5.14}$$

The power associated with higher harmonics than five of f_{LO1} and f_{LO2} is very small and can therefore be neglected. If one of the input signals is divided by two (Eq. (5.14)), the generated signal is in practice harmonically uncorrelated with the input signals. In this case, the coupled RF output signal of the direct conversion transmitter will mix with either f_{LO1}, f_{LO2} or with itself and generate therefore only out-of-band components. The up-conversion mixers of the direct conversion transmitter convert the baseband signal around every frequency component in the local oscillator signal spectrum.

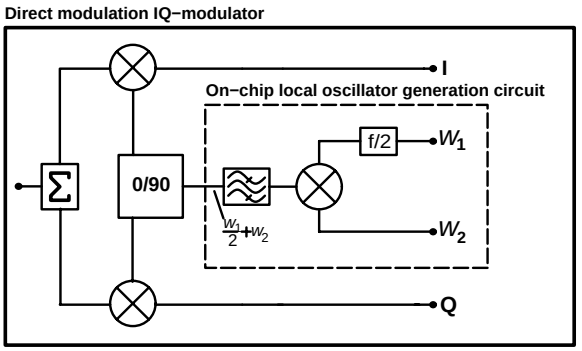

Figure 5.15 Direct modulator with on-chip LO generation

Because there is no filtering between the upconversion mixers and the power amplifier, all the unwanted frequency components will start to saturate the power amplifier at lower power levels. Therefore, all mixing products but the wanted one, i.e. higher order mixing terms at $n\omega_{LO2} \pm \frac{1}{2}m\omega_{LO1}$, n,m = 2,3,..., are filtered out with an active band-pass filter, as well as the other mixing product at the mirror frequency. However, depending on the frequency plan, the mirror frequency can be very close to the wanted signal, and the filter might not be able to filter out this component. Alternatively, a mixer topology, which removes the mirror frequency, could be used as shown in Figure 5.16. In this configuration, the mirror frequency is removed by 90° phase splitting and combining, and the band-pass filter only attenuates all the unwanted mixing products. In practice, due to parasitic components and layout considerations the mirror

frequency attenuation can be as low as 30 dBc [5.22]. The fact that the input power for the filter is constant makes this circuit topology very attractive for applying fully monolithic active resonator filters. The inherently poor noise properties of these filters do not limit their usability in the application, and their limited large-signal handling can be compensated with amplifying output buffers.

For the proposed circuit to function as explained, it is essential that the circuit is integrated on the same die with the transmitter. If the signal is taken off-chip at some point, for example to perform filtering, the RF output can couple to this pin and distort the generated local oscillator signal as explained.

5.7.3 Designed MESFET Circuit

A test circuit of the proposed on-chip local oscillator signal generation circuit was designed. The goal was to test the practical feasibility of the presented idea. The topology of the realized circuit is shown in Figure 5.15. The required building blocks were fabricated using the standard GEC-Marconi F20 D-MESFET technology. The gate widths of the active devices are 0.5 μm and the cut-off frequency f_T = 20 GHz.

The threshold voltage of the active devices is low, i.e. V_t = -1.8 V, which, together with the lack of enhancement mode devices, makes the process suitable for analog design only. Consequently, the divider, which is a digital circuit, is not very well optimized with this technology. The GaAs technology was selected because of easy access to the foundry, and because high quality and well-modeled inductors (with Q values over 10) and varactors that facilitate the implementation of the active band-pass filter. However, the circuit can be realized with any technology, providing that inductors and varactors are available.

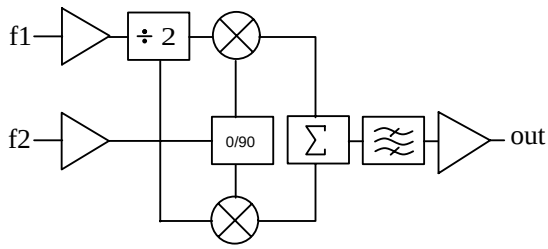

Figure 5.16 Mirror rejection topology of the local oscillator generation

The target system for the designed circuit is a DCS 1800 direct conversion transmitter. The desired output frequency of the proposed circuit is the same as the TX band of the system, i.e. 1710 – 1785 MHz. The input frequency f_{LO1} can be selected according to Figure 5.17, which is a graphical equivalent of Eq. (5.13). The wanted output frequency is then produced by selecting the other input frequency f_{LO2} appropriately. Tuning of the output signal is carried out by varying f_{LO2} accordingly. In our case, the input frequency f_{LO1} was fixed as 464 MHz in the specifications, and the frequency f_{LO2} is therefore 1942 – 2017 MHz.

The designed circuit blocks are all differential; therefore input and output buffers are needed to convert the single-ended inputs to differential and the differential output to single-ended, as well as to match the circuit to 50 Ω for facilitating measurements. A microphotopraph of the designed circuit is presented in Figure 5.18.

Frequency divider

GaAs flip-flop circuits as 6-NOR gate edge triggered flip-flops and ECL master-slave flip-flops have been adapted from silicon MOS or bipolar technologies. With a slight modification of the conventional 6-NOR gate D-flip-flop [5.23], we get a fully symmetrical D-flip-flop circuit that can be used as a frequency divider (Figure 5.19a). The maximum toggling frequency

of the flip-flop is $f = ¼t_{pd}$ (where t_{pd} is the mean propagation delay time in seconds per gate of the flip-flop) when used as a divide-by-two circuit. The advantage of the fully symmetrical topology is that a single-phase clock signal can be used as the input signal and that the output is differential.

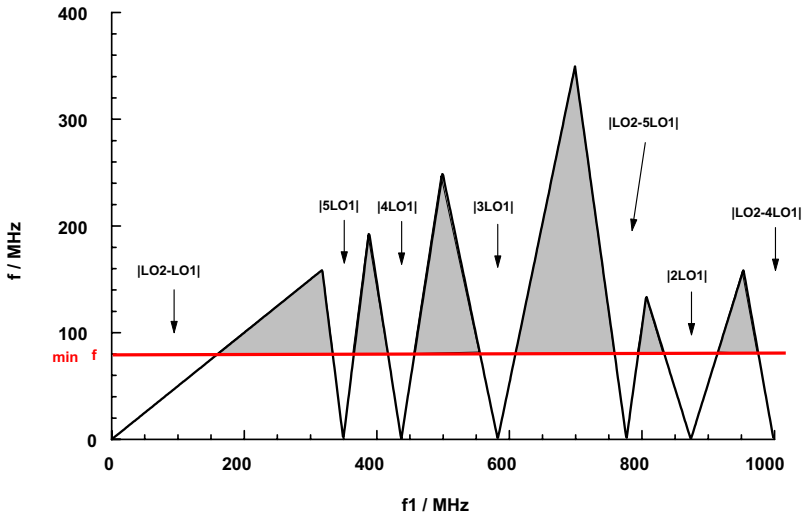

Figure 5.17 According to Eq. (5.13) possible selections of frequency f_{LO1}. Δf is the distance of the respective harmonic or mixing product to the center frequency 1747.5 MHz and min Δf marks the minimum allowed distance for out-of-band signals. If f_{LO1} is selected within the allowed shaded areas no in-band frequency components are created

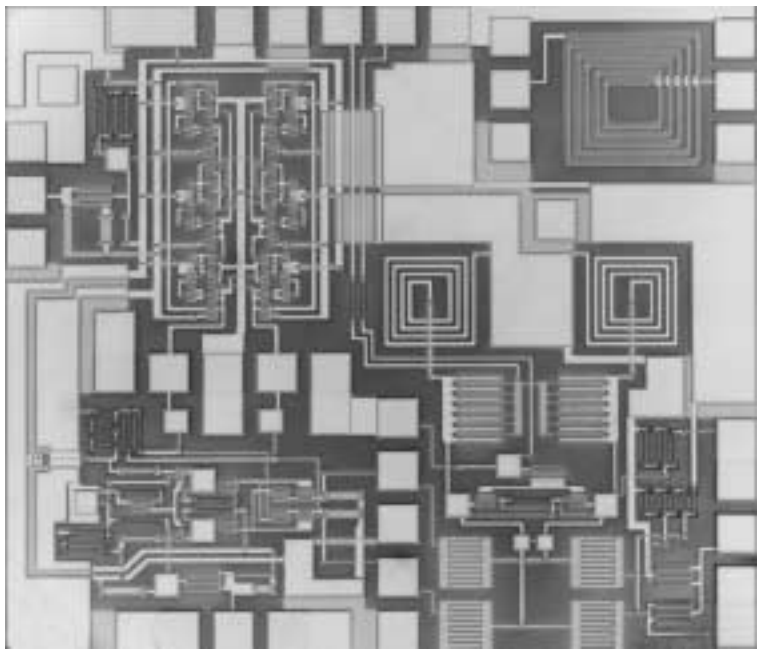

Figure 5.18 Microphotograph of designed circuit.
The inductor in the upper right corner is not a part of the circuit

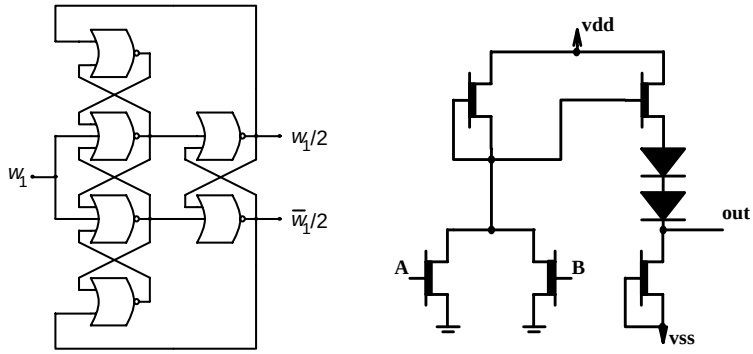

Figure 5.19 a) Implemented fully symmetrical frequency divider; b) BFL NOR-port

The most straightforward way of implementing a NOR gate is to connect transistors in parallel with an active load, i.e. a D-MESFET with gate connected to source. In this way, up to five-input NOR gates are possible. Because only D-MESFETs are provided by the foundry, a level shifter stage for V_{out}-to-V_{in} compatibility is needed. The logic block is biased with the positive supply voltage, and the level shifter stage that is implemented with two MESFETs connected as diodes in series is biased by a current source connected to the negative supply voltage. The level shifter stage is connected to the logic block output through a common source D-MESFET, and hence the level-shifter circuit acts as a buffer stage (hence the name, buffered FET logic, BFL, Figure 5.19b).

The number of diodes in the level shifter circuit is related to the low threshold voltage V_t of the active device used as the logic element. If the gate to source voltage of the common source transistor in the level shifter is approximately 0.3 V, and the voltage over a diode is 0.8 V, we get approximately (n is the number of diodes)

$$V_t = -(0.3 + 0.8n)\ \text{V} \tag{5.15}$$

From Eq. (5.15) it is easily seen that two diodes are needed in the level shifter stage. In order to minimize the capacitive load of the NOR gate and the current through the gate, the input transistors are of minimum width. The output waveform of the divider is a square wave with V_{pp} = 1.5 V.

The power consumption of the BFL gate, and therefore the divider, is directly proportional to the needed supply voltages and to the threshold voltage of the active device. The level shifter stage is biased between the negative and positive supply voltages of 3 V and -1.5 V. This, together with the low V_t, makes the power consumption of the GaAs MESFET divider high, namely 280 mW. With a more suitable choice of process or technology, it is possible to design divide-by-two circuits that have a power consumption less than 10 mW. The used technology is by no means suitable for digital IC design.

Mixer

Figure 5.20 introduces the realized mixer, a doubly-balanced Gilbert analog multiplier. The doubly-balanced connection of this mixer will cancel even-order spurious components at the IF output, which is important in monolithic mixer implementations, where spurious signals can interfere with other circuits integrated on the same IC through parasitic coupling paths.

The mixer consists of a linear voltage-to-current converter comprising common-source FETs in saturation. The output current of the RF transconductance stage is commutated by the local oscillator. The commutation process conserves the total current and therefore a fraction of the RF current is downconverted, the remaining RF current is upconverted around one or more

harmonics of the LO. The voltage conversion gain of the Gilbert cell multiplier is set by the choice of the transconductance and the load resistance.

The large voltage swing of the frequency divider output, used as the LO to the mixing core, quickly switches the FETs from their saturation region to their cutoff region, and vice versa. Thus, the switching FETs that are biased at $\frac{1}{2}I_{dss}$ operate like ideal switches. The transconductance FETs are biased in I_{dss}, and all the FETs of the mixer core are of equal size.

Due to the poor filter large signal handling capabilities, the maximum output power of the mixer is limited to -15 dBm. The conversion of the single-ended input signal to differential is performed by a matched differential pair. Input matching to 50 Ω is realized with a common-gate transistor giving an input return loss better than 20 dB.

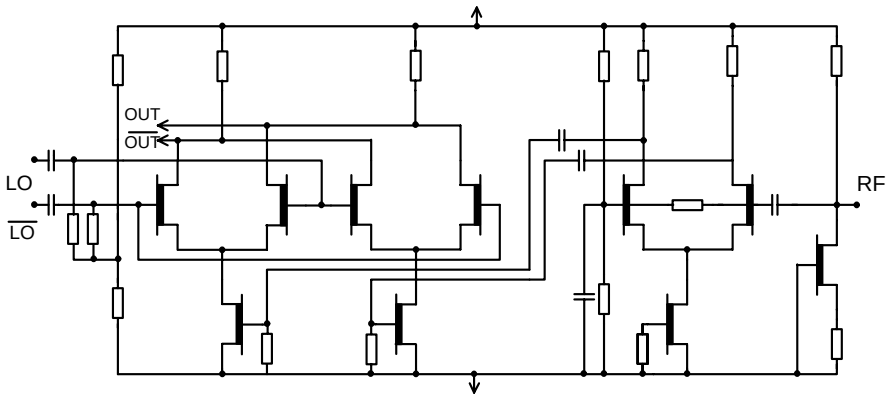

Figure 5.20 Gilbert cell mixer with input buffer

Active band-pass filter

A fully integrated band-pass filter which attenuates all unwanted mixing results and spurious frequencies was designed for the circuit. The implemented filter is a varactor-tuned parallel LC resonance circuit (Figure 5.21), where the cross-coupled differential active negative resistance circuit was used for loss compensation of the resonance tank [5.3][5.4][5.10][5.16].

As shown previously, if the transistor is modeled with the transconductance g_m, the output conductance g_{ds} and the gate-source capacitance c_{gs}, the input admittance is simply

$$Y_{in} = -\frac{g_m - g_{ds}}{2} + j\omega\frac{c_{gs}}{2} \tag{5.16}$$

This corresponds to a negative resistance in parallel with a capacitance ($g_m > g_{ds}$). The amount of negative resistance can be altered by adjusting the current and accordingly the transconductance g_m of the source coupled MESFETs, and thus the Q value of the tank is changed. If too much negative resistance is put in parallel with the resonance tank and the resulting tank resistance becomes negative, the circuit will be unstable and starts acting like an oscillator. Therefore, extra care has to be taken when adjusting the tank Q.

The nominal center frequency of the filter is 1.75 GHz. The center frequency was made tunable by varying the voltage of varactor-connected MESFETs. The sizes of the varactors are $6 \times 130\mu m$ giving a capacitance range of $0.8 - 2$ pF each. The frequency tuning range is ± 150 MHz. When adjusting the capacitance of the varactor pair the series resistance is also changed, which affects the tank Q-value. Therefore, the tank Q-value has to be tuned as the frequency is tuned. In a production circuit, however, a control circuit would have to be used for generating control bias voltages for the filter. The control circuitry could be realized with a dual-loop

master slave scheme as in [5.1][Section 5.5.1], which automatically adjust the bias voltages to maintain 0-dB pass-band insertion loss and stable center frequency in the presence of process tolerances and variations with operating conditions.

The dynamic range of the filter has less significance in this application than usually, as the input power level remains constant. Thus, excess in-band noise generated by the compensation circuit is of little interest. However, being the lowest in the whole circuit, the compression point of the filter dictates the maximum attainable output power. The compression point of a narrow-band filter is easily 20 dB lower than that of the compensation transconductor itself [Section 5.3] if the passive inductor Q is low. Thus, higher output power levels are possible only with amplification after the filter.

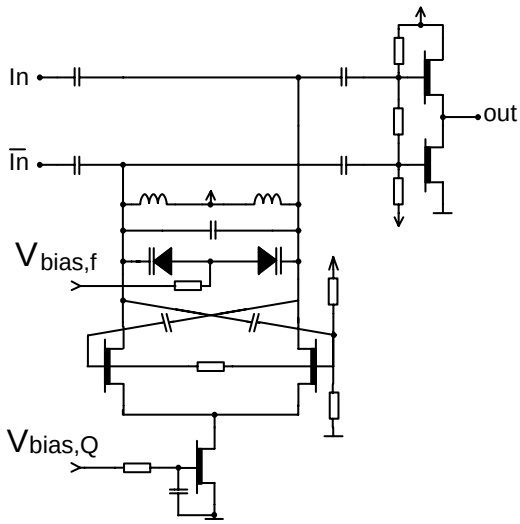

Figure 5.21 Fully monolithic band-pass filter with output buffer

5.7.4 Experimental Results

The performance of the circuit was verified with on-chip measurements. In Table 5.3, some key figures of the measured circuit are listed. Simulations were performed with Hewlett Packard Microwave Design System. Very good agreement between measured results and simulations of the CAD model was achieved.

P_1 (f_{lo1} = 464 MHz)	-10 dBm	Q-value	415
P_2 (f_{lo2} = 1942-2017 MHz)	-10 dBm	OCP	-20 dBm
P_2 (f_{lo2} = 1710-1785 MHz)	-25 dBm	Spurious frequencies	-40 dBc
filter f_{tuning}	1.56 - 1.91 GHz	Noise floor @ 20 MHz	-147 dBm/Hz

Table 5.3 Some performance results of the presented circuit

Figure 5.22a shows the measured output spectrum of the fabricated circuit. The output power of the wanted signal at 1.71 GHz is -25 dBm. The input power levels are kept at their nominal values, -10 dBm. The maximum output power is limited by the filter large-signal characteristics. The measured -1-dB output compression point is -20 dBm. If the Q value is tuned simultaneously as the input power is increased, the filter power handling capabilities are improved. This is due to the degradation of the negative resistance when the input signal level is raised.

The frequency tuning range of the filter is 1.56 – 1.91 GHz. In Figure 5.22b the frequency responses of the band-pass filter at both extremes and at the nominal frequency are shown. As

the input frequency is tuned, the spectral components move accordingly along the frequency axis. The loaded Q value was measured as the ratio of the center frequency to the two-sided -3-dB band-with and was found 415.

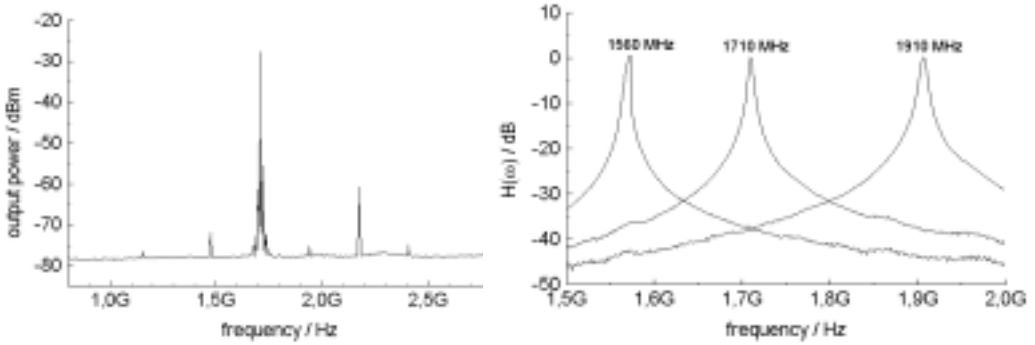

Figure 5.22 a) Power spectrum at output; b) Frequency response of band-pass filter at both extremes and at the nominal frequency

The mixer mirror frequency at 2174 MHz is attenuated 30 dBc. In principle, the mirror component attenuation can be improved with a filter of higher order. As a consequence of adding more stages to the filter, the bias arrangements become complicated and sensitiveness towards process variations rise. Alternatively, the mixer topology with rejection of the mirror frequency could be used.

The phase noise of the output signal in an issue in LO signals. The mixer and the band-pass filter do not add hardly any phase noise to the signal in theory, and the phase noise of the realized divider is very small according to a comparison made in [5.24]. Hence, the phase noise of the output signal is practically the sum of the phase noises of the two input signals.

The noise floor of -147 dBm/Hz was measured at 20 MHz offset from the filter center frequency. To get a clear picture of how the noise floor of the proposed circuit would affect the total noise of a direct conversion modulator, the local oscillator signal generation circuit should be integrated on the same chip with the modulator. In some applications the noise floor of the direct conversion modulator should be around -140 dBm/Hz. If it were assumed that the modulator mixer LO leakage were 25 dB and the mixer were passive, which also attenuates the LO-based noise floor, the noise floor at the output of the local oscillator signal generation circuit should be -165 dBm/Hz.

5.7.5 Conclusions

A local oscillator generation circuit for a direct conversion transmitter has been designed. The circuit demonstrates that a local oscillator signal can be generated from two reference signals as proposed, which strongly reduces the effect of coupling between the transmitter antenna path and the local oscillator, provided that the circuit is integrated on the same die with the modulator. Thus, on-chip LO filtering could provide improved performance, and due to loose specifications, be the first application for active microwave filters in cellular systems, even though the high noise floor caused by the active device can couple to the signal path and increase the noise of the modulator. The results obtained from this circuit give valuable information for further development of the on-chip LO generation circuit. With a more suitable process a large improvement considering especially the power dissipation can be achieved.

The studies and results presented in this section have been published in [5.25] and [5.26].

5.8 Application Case II: Local Oscillator Generation Circuit for Direct Conversion Transmitters in BiCMOS Technology

5.8.1 Introduction

Referring to the previous section, BiCMOS technologies offer several benefits for LO generation circuit design. The digital part, i.e. the divider with its auxiliary circuits, can be designed with complementary MOS transistors, which significantly reduces the overall power consumption and the die area in spite of the greater complexity. Proven CMOS topologies for the divider can be easily applied. In addition, bipolar transistors with high-frequency capabilities are available for RF sections.

The mirror-rejection topology shown in Figure 5.23 was experimented in this circuit. The test chip was fabricated with a 0.25-µm BiCMOS silicon process especially targeted for RFIC design. The process provided spiral inductors and varactors for uncomplicated implementation of the band-pass filter, and the negative resistor filter topology could be employed. The circuit was realized as differential with 100-Ω terminations so that the power specifications are comparable to the single-ended version. The LO1 low frequency input port has a very high input impedance, and therefore the input quantity cannot be power but voltage. A minimum input voltage of 50 mV (single-ended) was used as a design target.

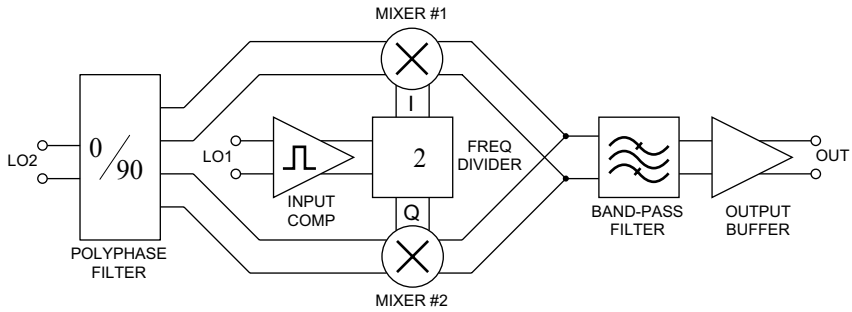

Figure 5.23 Mirror-rejection topology for LO generation circuits

5.8.2 Divider

The divide-by-two frequency divider provides the low-frequency signal to the mixers. The mirror-rejection operation requires output signals in all four quadratures, which is easily realizable with the conventional latch-based topology. The divider block consists of an input comparator, a divider core and output buffers.

The low-frequency signal LO1 is amplified and potentially clipped in the twin-stage input comparator shown in Figure 5.24a. The comparator stages are normal CMOS-inverters with common-mode feedback for DC-offset stabilization. The simulated gain at 464 MHz is 24 dB, which enables functioning even at low input amplitudes.

The conventional CMOS-latch (Figure 5.24b) is used in the divider core. The cross-coupled connection of two latches forms a 2-divider with direct I and Q outputs (Figure 5.25). The maximum division frequency is partly determined by the bias current of the latches. In this case, a 500-µA bias current ensures operation up to 2 GHz.

Output buffers were needed for preventing the mixers from loading the divider and for limiting the signal swing to its optimal value for the mixers, 150 mV.

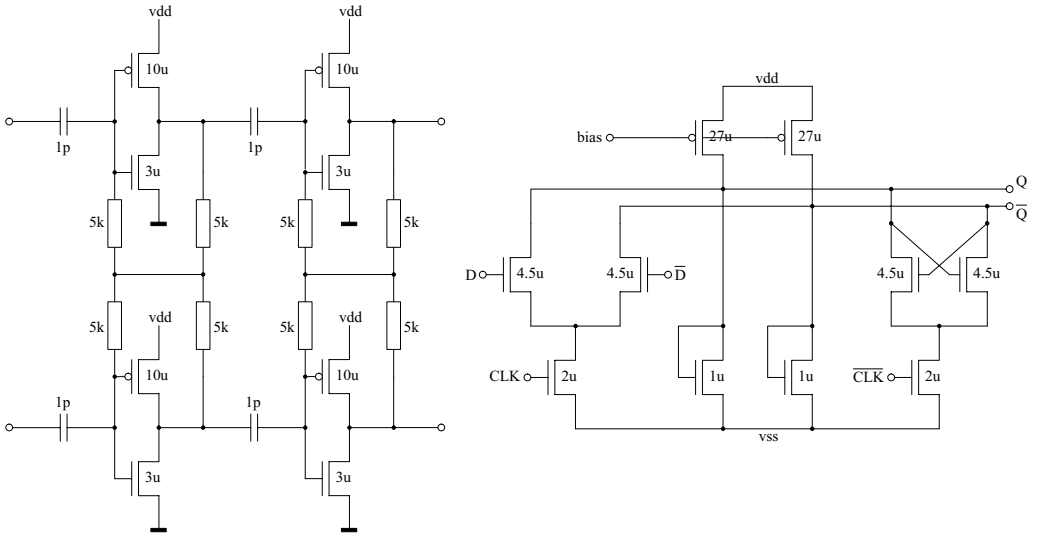

Figure 5.24 a) Input comparator; b) Latch circuit

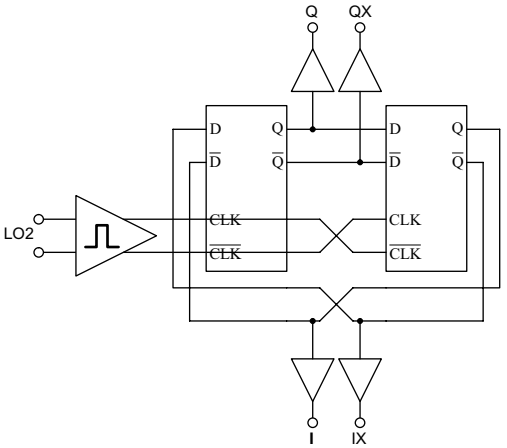

Figure 5.25 Divide-by-two frequency divider based on latch circuits

Simulated results

The simulated input and all four output waveforms of the divider core are shown in Figure 5.26. The comparator input signal amplitude is 250 mV. The simulated power consumption for the whole digital part is 14 mW.

Measured results

The digital section of the circuit (the input comparator, the divider core and the output buffers) was processed also as a stand-alone unit for testing purposes. The measured output waveforms are plotted in Figure 5.27. It must be noted that the circuit was loaded by 50 Ω during the measurements instead of the actual high input impedance of the mixer. Therefore, the measured output swing is very low.

In addition to the actual input frequency 464 MHz, a lower frequency of 100 MHz was also used. At 464 MHz the phase error due to the slightly different signal leads becomes visible, as well as the limited bandwidth of the used 500-MHz sampling oscilloscope.

The unloaded power consumption of the digital part was measured to be 11.7 mW being slightly smaller than predicted. The maximum operating frequency is 1.92 GHz with an input signal amplitude of 750 mV. At high frequencies, the input comparator gain becomes insufficient for small input signals. The minimum operational input amplitude is 35 mV at the nominal frequency of 464 MHz. The lower the frequency the more the input signal is attenuated due to the 1-pF coupling capacitors in the comparator, and the minimum functional input level is raised.

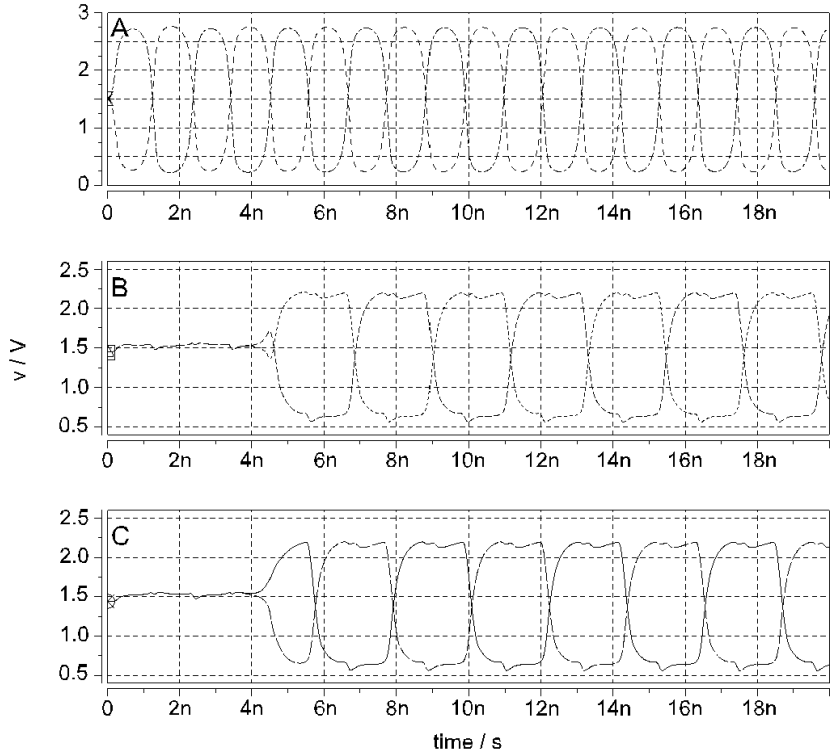

Figure 5.26 Simulated divider core waveforms: A input, B I-output I, C Q-output

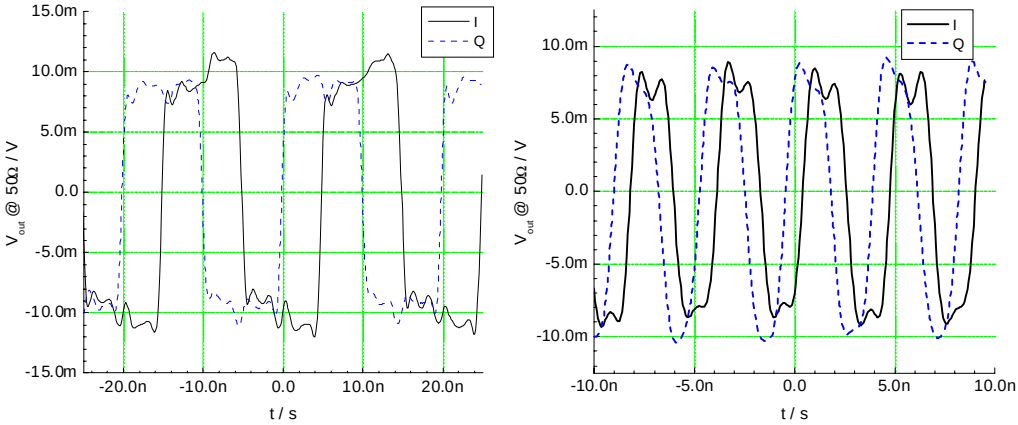

Figure 5.27 a) Measured output of the stand-alone divider at f_{in} = 100 MHz, v_{in} = 200 mV unbal, 375 mV bal; b) Measured output of the stand-alone divider at f_{in} = 464 MHz, v_{in} = 200 mV unbal, 375 mV bal

5.8.3 Polyphase Filter

The high-frequency input signal LO2 is fed to a two-stage balanced polyphase filter, shown in Figure 5.28, which creates the quadrature signals needed. The I and Q branches are then buffered and amplified with differential pairs for compensating the loss in the polyphase filter.

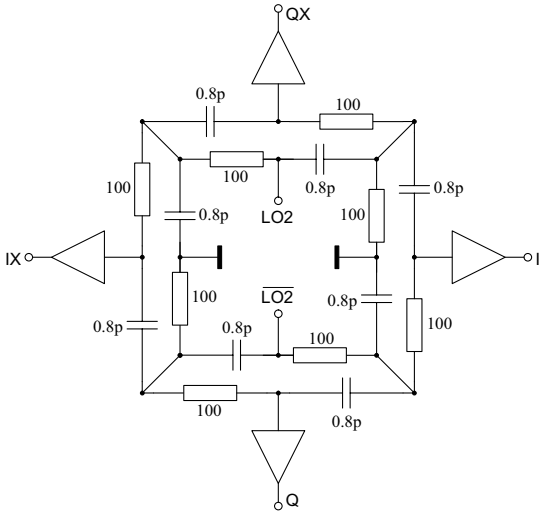

Figure 5.28 Polyphase filter

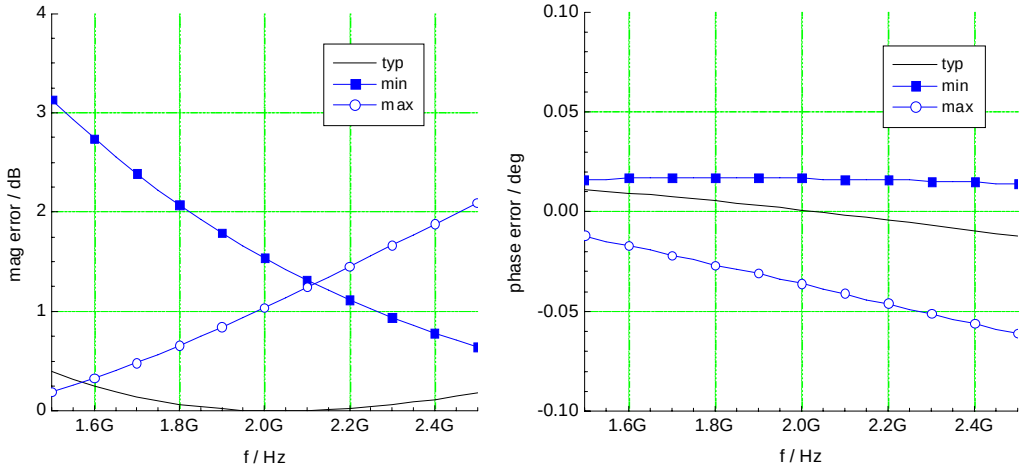

Figure 5.29 a) Magnitude error of the polyphase filter; typical and the simulation corners; b) Phase error of the polyphase filter; typical and the simulation corners

5.8.4 Mixers

According to Figure 5.23, the combined output of the mixers is

$$v_o = A\sin(\omega_1 t)\sin(\omega_2 t) + A\cos(\omega_1 t)\cos(\omega_2 t) = A\cos(\omega_2 - \omega_1)t \qquad (5.17)$$

and the mirror frequency $A\cos(\omega_1+\omega_2)t$ is suppressed, provided that the phase shift between the branches is exactly 90º. If a phase error $\Delta\varphi$ and a relative amplitude Δa error between the branches occur, as inevitably happens in practice, the mirror-rejection ratio MRR becomes

$$MRR = \frac{P_{\omega_2-\omega_1}}{P_{\omega_2+\omega_1}} = \frac{1+\Delta a^2+2\Delta a\cos(\Delta\varphi)}{1+\Delta a^2-2\Delta a\cos(\Delta\varphi)} \tag{5.18}$$

Theoretically one degree of total phase error without magnitude error corresponds to an MRR of 41 dBc, whereas a sole 1-dB amplitude error (Δa = 0.891) will lead to a high 25-dBc MRR. To avoid these degradations, one must take care of good matching and uncompromising symmetry between the I and Q branches in the layout design.

The mixer cores are conventional balanced Gilbert cells optimized for the given input signal levels. Their simulated power consumption is 11 mW each. The schematic diagram of the whole mixer without the bias arrangements can be seen in Figure 5.30.

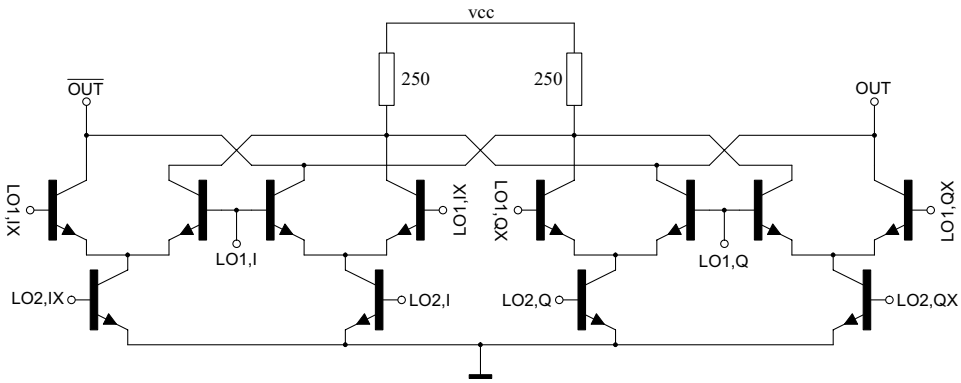

Figure 5.30 Gilbert-cell mixer

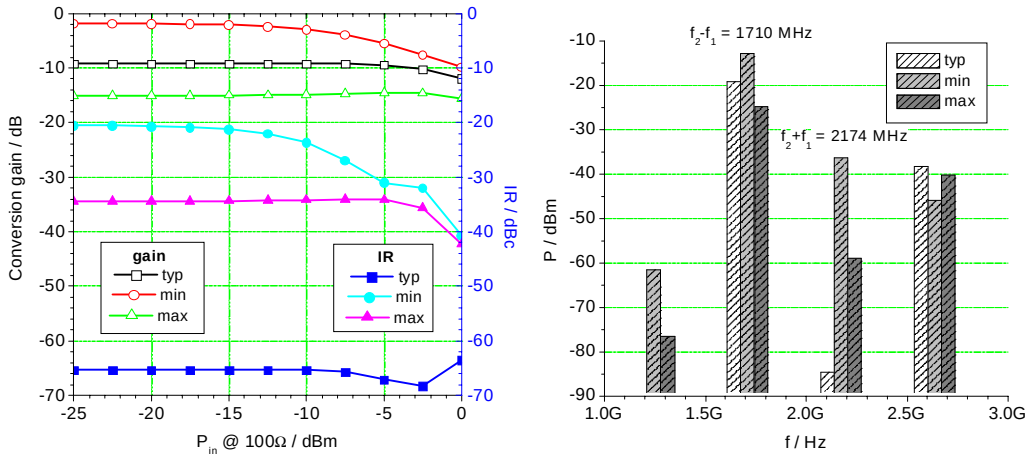

Figure 5.31 a) Simulated conversion gain and mirror rejection ratio;
b) Simulated output spectrum of the mixers

5.8.5 Band-Pass Filter

The band-pass filter shown in Figure 5.32 is a second-order capacitively coupled LC resonator with a controllable negative resistance for Q enhancing. The negative resistance circuit is a cross-coupled transistor pair that compensates the low quality factors (< 10) of the integrated spiral inductors and enables arbitrarily high unloaded Qs for the LC resonator. The amount of negative resistance is adjusted by changing the bias current. The filter center frequency is controlled by a pair of varactor diodes in the back-to-back configuration. The simulated tuning range of the filter is 1.65 – 1.95 GHz when the frequency tuning voltage is varied from 2.2V to 3.2V. The Q tuning current is simultaneously set for minimum filter insertion loss (1 mA – 4 mA), resulting in the power consumption starting from 10 mW. The maximum simulated stable loaded Q is around 200.

For testing purposes, the band-pass filter was also processed as a stand-alone circuit. The power handling requirements in the actual LO generation circuit (P_{out} = -10 dBm) required an emitter-degeneration resistor of 100 Ω in the negative resistor circuit, but this was omitted in the stand-alone filter. The tuning range is practically identical, but the Q control currents are lower than 1 mA due to the lack of the gain-decreasing emitter resistor (the power consumption is less than 5 mW).

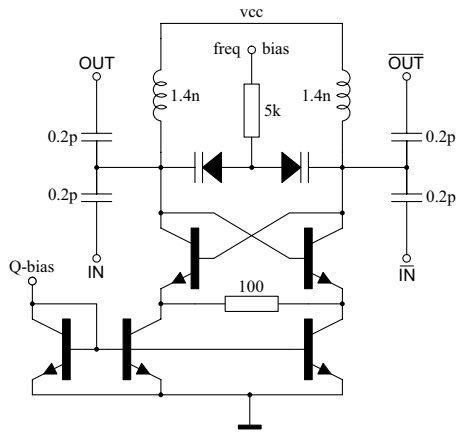

Figure 5.32 Negative resistance resonator filter

Measured results

The stand-alone filter responses (minimum, maximum and nominal) are shown in Figure 5.33a. The measured tuning range is 1.48 – 1.82 GHz (Figure 5.33b), and depending on the tuning current setting, the power consumption ranges from 3 mW to 3.5 mW. The measured loaded Q value at mid-band is 200. The measured tuning range is shifted down 150 MHz from the expected value. This is caused by the inaccurate varactor foundry model that predicted too low varactor capacitances. In addition, only one varactor size was modeled, which made the selection of nominal resonance frequencies very coarse.

The large-signal performance of the stand-alone filter is depicted in Figure 5.34. Due to the high Q_l, the compression point is very low (-67 dBm). As the measured noise figure is approximately 30 dB at the whole frequency band, the dynamic range becomes 38 dB.

5.8.6 Output Buffers

The output buffer is an ordinary emitter-coupled pair followed by an emitter follower. Its function is to prevent the termination impedances from loading the high-impedance output of the band-pass filter, amplify the signal for the maximum output power, and match the output to

50 Ω. The matching draws a large amount of DC current, and therefore the simulated power consumption of the output buffer is 65 mW representing 65% of the whole circuit value. If used as a part of a bigger system with higher interconnection impedances, the power consumption can be greatly reduced.

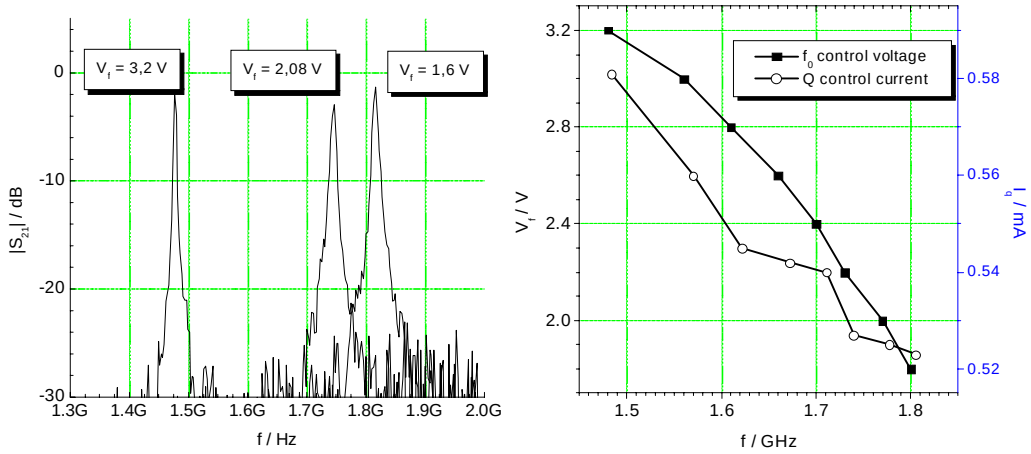

Figure 5.33 a) Frequency response of the stand-alone filter; b) Center frequency and Q control

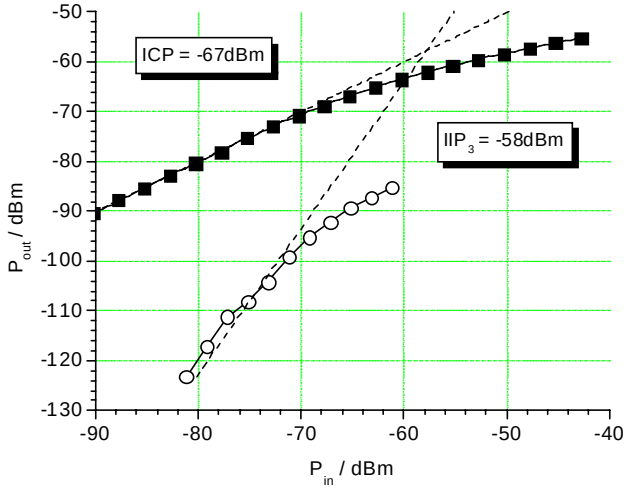

Figure 5.34 Compression and IM performance of the stand-alone filter, f = 1.65 GHz

5.8.7 Entire System

Simulated results

The simulated total gain from the f2 input to the output is 26 dB (OCP –12 dBm). The nominal power consumption of the total circuit is predicted to be 86 mW + 14 mW = 100 mW (33 mA), most of which (65 mW) is consumed in the output buffer. Due to the perfect balance in the simulator, the simulated nominal mirror-rejection values are infinitesimal.

Measured results

In Figure 5.35a, the system frequency response is plotted. Calculated from the plot, the loaded quality factor is as high as 300, complying well with the simulations. The increase of Q in the full circuit can be explained with higher source and load impedances seen by the filter in the system. The tuning range is shifted further downwards, which implies that the system filter is loaded by extra capacitance not accounted for by the simulator. By redesigning the LC network, this problem should be solved.

The power response is shown in Figure 5.35b. As seen, the specified output power of -10 dBm is reached in strong compression. The output compression point is -22 dBm, and the total gain is 23 dB. The output spectrum of the whole circuit is shown in Figure 5.36. The mirror rejection with the filter on is >70 dBc, and with the filter off 39 dBc. The LO2 frequency is attenuated 60 dBc and 33 dBc, respectively. The low filter-off rejection ratios are due to the imperfect balance of the input and output baluns in the measurements, though trimmed, and the process-inflicted mismatch errors on the chip.

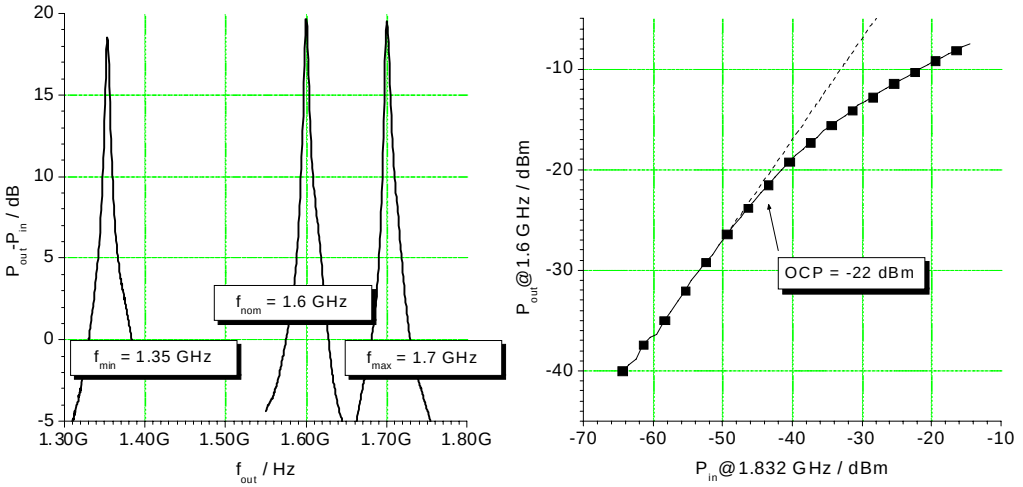

Figure 5.35 a) Output frequency response; b) Power-sweep response, P_{LO2} = -30 dBm

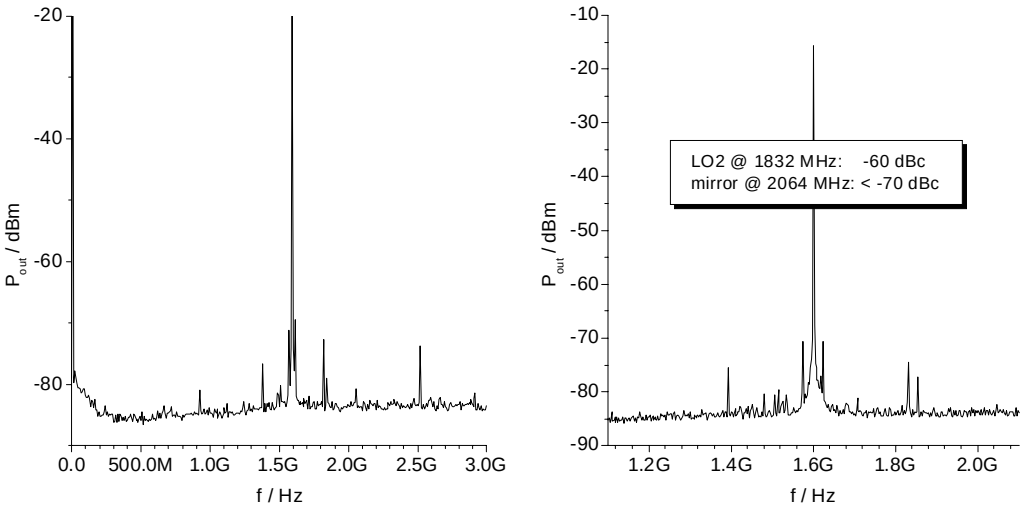

Figure 5.36 a) Output spectrum, P_{LO2} = -30 dBm; b) Spectrum close-up

The measured power consumption is 103 mW, which complies with the simulated value extremely well.

The noise floor measured at 10-MHz offset from the carrier is -139 dBm/Hz. For curiosity, the phase noise at the output was also measured. When compared to the source phase noises the additional noise generated by the circuit is small but nevertheless detectable. The most obvious change can be detected in the raised noise floor.

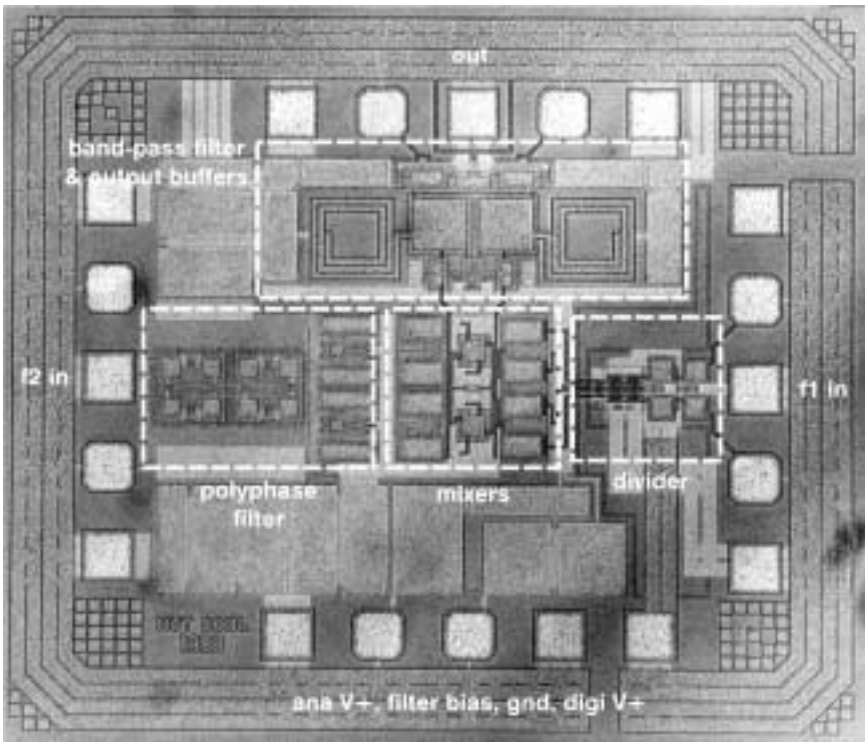

Figure 5.37 Photograph of BiCMOS LO generation circuit

The microphotograph of the processed chip is shown in Figure 5.37. As the design is obviously sensitive to imbalance, the layout was drawn as symmetrically as possible, and all the differential signal leads are exactly of the same length. All the differential blocks are exact mirror copies of each other. The active chip area is 0.93 x 0.71 mm^2 without the pads and the pad ring. As seen from the photograph, the actual functional blocks occupy roughly only a half of this area, since the layout is pad-restricted (the pads are set for five-finger GSGSG probe heads with 150-μm pitches). The rest of the area is filled with RF grounding capacitors for the DC voltage lines.

5.8.8 Comparisons and Conclusions

Finally, it is interesting to compare some key performance figures of both realized LO generation circuits. They have been gathered in Table 5.4. The results are very much comparable, since the most crucial specification, the output power compression, is approximately the same in both realizations. The differences in other properties stem from the characteristics of the GaAs-MESFET and BiCMOS technologies and the circuit topologies chosen. It is very much obvious that the MESFET technology is not suitable for the application, except for demonstration purposes.

	GaAs-MESFET	Si-BiCMOS
Active chip area	2,3 mm^2	0,66 mm^2
Operating voltage	+3 V, -1,5 V	3 V
Power consumption	387 mW, divider 280 mW	103 mW, output buffers 65 mW
Mirror rejection	31 dBc	>80 dBc
Freq. tuning range	1,58 – 1,91 GHz	1,35 – 1,7 GHz
Filter Q	414	300
Output –1 dB comp. point	-20 dBm	-22 dBm

Table 5.4 Performance comparison of the LO circuits

The motivation for designing local oscillator generation circuits for direct conversion transmitters has been in the possibility to take advantage of fully monolithic active resonator filters discussed in this thesis. In the light of the obtained results, it has been successfully demonstrated that the concept is functional and feasible. However, a proper automated tuning mechanism must be adopted for the band-pass filter in a fully applicable system. Nevertheless, the high-frequency performance of the LO generation circuit is adequately characterized even with presented test circuits.

References

[5.1] W. Aparin and P. Katzin, 'Active GaAs MMIC Band-Pass Filters with Automatic Frequency Tuning and Insertion Loss Control,' *IEEE Journal of Solid-State Circuits*, Vol. 30, pp. 1068-1073, October 1995.

[5.2] U. Karacaoglu and I. Robertson, 'MMIC Active Bandpass Filters Using Varactor-Tuned Negative Resistance Elements,' *IEEE Transactions on Microwave Theory and Techniques*, Vol. 43, pp. 2926-2932, December 1995.

[5.3] Pipilos, Y. P. Tsividis, J. Fenk and Y. Papananos, 'A Si 1.8 GHz RLC Filter with Tunable Center Frequency and Quality Factor,' *IEEE Journal Solid-State Circuits*, Vol. 31, pp. 1517-1525, October 1996.

[5.4] R. Kaunisto, K. Stadius and V. Porra, 'Active MMIC Filters with Negative Resistance Compensation,' *Electronics Letters*, Vol. 34, pp. 1236-1237, June 1998.

[5.5] R. Kaunisto, K. Stadius and V. Porra, 'A 3-GHz Silicon-BJT Active Resonator and Filter,' *Proceedings of IEEE International Conference on Electronics, Circuits and Systems*, Lisbon Portugal, Vol. 3, pp. 197-200, September 1998.

[5.6] W. Kuhn, N. Yanduru and A. Wyszynski, 'Q-Enhanced LC Bandpass Filters for Integrated Wireless Applications,' *IEEE Transactions on Microwave Theory and Techniques*, Vol. 46, pp. 2577-2585, December 1998.

[5.7] J. Voorman and D. Blom, 'Noise in Gyrator-Capacitor Filters,' *Philips Research Report*, Vol. 26, pp. 114-133, 1971.

[5.8] A. Abidi, 'Noise in Active Resonators and the Available Dynamic Range,' *IEEE Transactions on Circuits and Systems – I*, Vol. 39, pp. 296-299, April 1992.

[5.9] W. Kuhn, F. Stephenson and A. Elshabini-Riad, 'Dynamic Range of High-Q OTA-C and Enhanced-Q LC RF Bandpass Filters,' *Proceedings of IEEE Midwest Symposium on Circuits and Systems*, 1994, pp. 767-771.

[5.10] W. Kuhn, F. Stephenson and A. Elshabini-Riad, 'A 200 MHz CMOS Q-Enhanced LC Bandpass Filter,' *IEEE Journal of Solid-State Circuits*, Vol. 31, pp. 1112-1122, August 1996.

[5.11] P. Alinikula and R. Kaunisto, 'Microwave Active Filters for Wireless Applications: Systems Approach,' *European Microwave Conference Proceedings*, Jerusalem Israel, Vol. 1, pp. 409-414, 1997.

[5.12] J. Macedo and M. Copeland, 'A 1.9-GHz Silicon Receiver with Monolithic Image Filtering,' *IEEE Journal of Solid-State Circuits*, Vol. 33, pp. 378-386, March 1998.

[5.13] O. Jensen et al., 'RF Receiver Requirements for 3G W-CDMA Mobile Equipment,' *Microwave Journal*, Vol. 43, pp. 22-46, February 2000.

[5.14] Bluetooth Specification Version 1.0 B, *http://www.bluetooth.com/developer/specification*, pp. 17-32, November 1999.

[5.15] Y. Wang and A. Abidi, 'CMOS Active Filter Design at Very High Frequencies', *IEEE Journal of Solid-State Circuits*, Vol. 25, pp. 1562-1573, December 1990.

[5.16] R. Kaunisto, D. Webster and D. Haigh, 'Improved MMIC Filters Based on Passive LC Resonators with Active Negative Resistance Circuits,' *IEE Colloquium on Advanced Signal Processing for Microwave Applications*, Stevenage UK, pp. 3/1-3/6, November 1996.

[5.17] A. Parker, 'Implementing SPICE Models with High-Order Continuity and Rate Dependence,' *IEE Proceedings of Circuits, Devices and Systems*, Vol. 141, pp. 251-257, April 1994.

[5.18] R. Kaunisto, P. Alinikula, K. Stadius and V. Porra, 'A Low-Power HBT MMIC Filter Based on Tunable Active Inductors,' *IEEE Microwave and Guided Wave Letters*, Vol. 7, pp. 209-211, August 1997.

[5.19] R. Kaunisto, P. Alinikula and K. Stadius, 'Active Inductors for GaAs and Bipolar Technologies', *Analog Integrated Circuits and Signal Processing*, Vol. 7, pp. 35-48, January 1995.

[5.20] D. Haigh, D. Webster, R. Kaunisto, C. Nduijuba, A. Khanifar, M. Darvishzadeh, T. Parker, J. Scott and I. Thayne,' Developments in RF Design,' *Proceedings of IEE Colloquium on RF Design*, London UK, 10 p., February 1996.

[5.21] B. Razavi, 'RF Microelectronics,' Prentice Hall PTR, USA, 352 p., 1998.

[5.22] J. Kiraly, S. Kalajo and V. Porra, 'A Low Voltage GaAs Direct I/Q-Modulator and Power Amplifier for 2 GHz Transmitter,' *Proceedings of Norchip Conference*, Helsinki Finland, pp. 52-57, November 1996.

[5.23] H. Hausila, R. Sadler, W. Tanis and A. Schenberg, 'GaAs Prescalers and Counters for Fast-Settling Frequency Synthesizers,' *IEEE Journal of Solid-State Circuits*, Vol. 25, pp. 239-245, February 1990.

[5.24] B. De Muer and M. Steyaert, 'A Single-Sided 1.5 GHz 8/9 Dual-Modulus Prescaler in 0.7um CMOS with Low Phase Noise and High Input Sensitivity,' *Proceedings of European Solid-State Conference*, The Hague The Netherlands, pp. 256-259, September 1998.

[5.25] J. Riska, R. Kaunisto, P. Alinikula and K. Halonen, 'Fully Monolithic On-Chip Local Oscillator Generation Circuit for Direct Conversion IQ-Modulators,' *Proceedings of Asia-Pacific Microwave Conference*, Yokohama Japan, pp. 155-158, December 1998.

[5.26] J. Riska, R. Kaunisto, P. Alinikula and K. Halonen, 'Local Oscillator Generation Circuit for Direct Conversion Transmitter,' *Analog Integrated Circuits and Signal Processing*, Vol. 22, pp. 7-15, January 2000.

6. CONCLUSIONS

In this doctoral thesis, the specific design issues of monolithic microwave-frequency active resonator filters have been tackled. The high-Q active resonators employed in the filters are divided into two groups: passive LC resonators with active negative resistance compensation, and active inductor resonators.

Different microwave negative resistor topologies have been shown to derive from a single three-port. Thus, they can be categorized, and their fundamental differences recognized. This has also enabled comparisons in terms of performance and feasibility. Particularly noise and distortion properties have been elaborated, as they are the main concerns in practical applications. It is shown by measurements that the derived theoretic results can be used as guidelines for practical designing. The gyrator-based active inductors have also been analyzed carefully. A method for eventual cancellation of the losses generated by loop phase errors in gyrators has been presented. The phenomena in practical circuits follow this theory very well.

Simple models for transistor noise and non-linearities have been used throughout the calculations. Although the absolute theoretical results give an optimistic view, their relative accuracy is good and useful for practical dimensioning. The Volterra-series approach for calculating distortion responses has been applied to the resonator topologies. It clarifies the effect of each non-linearity term on the distortion responses. Although the analyses had to be much simplified for illustrative results, the noise and distortion studies have revealed the key factors affecting the performance, and guidelines for optimal dimensioning has been given. It has been made clear that the noise and distortion properties of active resonators are usually insufficient for traditional purposes, which is often ignored in published papers. Nevertheless, by keeping the limitations in mind one can find new feasible applications for the circuits described.

Several active resonators and filters have been designed. Different process technologies have been experimented, and their suitability for active resonator design has been evaluated. Understanding the theoretical limitations, the performance figures have been on a par with other published works, but generally, somewhat lower noise figures and power consumptions have been acquired. Cellular telephones are commonly regarded as potential applications for monolithic active filters. It has been shown, however, that the noise and dynamic range performance of active resonator filters is insufficient for direct replacement of passive filters in current wireless architectures. Instead, a new application, where active resonator filters could be beneficially used, is presented: an LO signal generation circuit with applications in frequency synthesizers of direct-conversion transmitters. Two such circuits, realized with different technologies, have been presented in the thesis. The results show that the filter performance does not hinder the system from functioning as desired.

The future of monolithic filter design will be much brighter if the development of high-Q passive spiral inductors, or even better, hyper-Q micromechanical resonators, provides new possibilities for low-noise realizations. At some point, however, it will be questionable to use active components at all, and the topologies will revert to passive resonators. Research on these subjects will be of great interest, given the motivation of this work.